FILTER DESIGN OF HIGH POWER DENSITY CONVERTER WITH WEIGHT, SIZE AND THERMAL CONSIDERATIONS

LIU YONG

School of Electrical and Electronic Engineering

A thesis submitted to the Nanyang Technological University

in partial fulfillment of the requirement for the degree of

Doctor of Philosophy

2018

Acknowledgements

I would like to express my sincere gratitude to my supervisor, Associate Professor See Kye Yak, for his patience, support, and encouragement during my study as a PhD student. He not only taught me the subject matter related to my research but also the opportunities and challenges for my future research direction and career.

The research is conducted within the Rolls-Royce @ NTU Corp Lab with financial support from the National Research Foundation (NRF), Singapore, under the Corporate Laboratory @ University Scheme. Hence, I would like to thank Rolls-Royce, NRF and NTU for the opportunity in working in the Corporate Laboratory. I am also thankful to the research group members, especially to Associate Professor Josep Pou, Assistant Professor Tang Yi, Dr. Rejeki Simanjorang, Dr. Gajanayake Chandana, Dr. Gupta Amit, Dr Liu Yitao, Dr Tong Chin Foong, Dr Arie Nawawi, Dr Yin Shan, Dr Assel Sakanova, Dr Lim Ziyou and Mr Men Kai, for their technical inputs and suggestions. Also, my appreciation goes to Professor Tseng King Jet and Visiting Professor Jason Lai Jih-Sheng, for their guidance and valuable advice in the field of power electronics.

I would like to thank my colleagues and friends in the Electrical Power System Integration Lab@NTU (EPSIL@N) for their help and friendship. They are Mr Zhang Yicheng, Mr Yu Yang, Mr Zhai Jianyang, Mr Tu Pengfei, Mr Fan Fei, Mr Shi Donghan, Mr Wang Shuai, Mr Ji Dongxu, Ms Xu Qianwen, Dr Mao Xiaohe, Dr Liu Xiong, Dr Liu Sijun, and Dr Guo Fanghong.

The technical and measurement support from Mr Wee Seng Khoon, Mr Lim Kim Peow and Dr Chen Jian are gratefully acknowledged.

Last but not least, I would like to give my deepest gratitude and love to my family for their support, encouragement, and contribution without expecting anything in return during my academic pursuit. Their support, understanding and love throughout my life are beyond words.

Abstract

Adopting more efficient electric technologies in the aircraft industry has been gaining attention with the objectives to decrease fuel consumption and reduce environmental impact. The backbones of more electric technologies are power converters to interface between loads and power grids. For aerospace applications, these power converters must be both compact and light, and hence, realization of high power density converter (HPDC) is necessary. Pulse width modulation (PWM) technique with high switching frequency is commonly employed in HPDC design but it results in large harmonic contents. To achieve high power density, increasing the switching frequency of the power converter has also become a necessity. Hence, practically all HPDCs require passive filters to meet the stringent power quality requirements. For all the filter configurations, LCL filter is the most popular choice in grid-connected power converter systems for its excellent performance. However, it is also a major contributor of the overall weight of an HPDC, especially the inverter-side inductor, which requires to suppress higher frequency harmonic contents at the inverter side. The main focuses of this thesis are to explore various design techniques in size and weight reduction of passive filters.

Then, the benefits of interleaving three phase voltage source converters (VSCs) are presented to improve the power density. To further improve power density of HPDC, different levels with power converter includes two-level, three-level, and five-level configurations will be investigated, with two types of three-

phase power grids, the three-phase three-wire and three-phase four-wire power grids.

Lastly, the common mode inductor, includes the extraction of common mode (CM) and differential mode (DM) inductances are analysed by using 3D finite element method (FEM). The effects of CM and DM currents on the magnetic core saturation, the parasitic capacitance of a CMC, and different core structures on the performance are evaluated. In addition, the high density and liquid-cooled CMC are also analyzed with computational fluid dynamics (CFD) and ANSYS Fluent.

Table of Contents

List of Figures

List of Tables

List of Abbreviations

APF: Active Power Filter
CFD: Computational Fluid Dynamics
CM: Common Mode
CMC: Common Mode Choke
CI: Coupled Inductor
DM: Differential-mode
DSP: Digital Signal Processor
EMC: Electromagnetic Compatibility
EMI: Electromagnetic Interference
EPC: Equivalent Parallel Capacitance
ESL: Equivalent Series Inductance
EV: Electric Vehicle
FEA: Finite Element Analysis
FEM: Finite Element Method
FFT: Fast Fourier Transform
GaN: Gallium Nitride
HAPF: Hybrid Active Power Filter
HEV: Hybrid Electric Vehicle
HPDC: High Power Density Converter
IGBT: Insulated-Gate Bipolar Transistor
MEA: More Electric Aircraft
MEE: More Electric Engine
MOSFET: Metal-Oxide-Semiconductor Field-Effect Transistor
NPC: Neutral Point Clamping
NSC: Network Side Converter
PCB: Printed Circuit Board
PPF: Passive Power Filter
PWM: Pulse Width Modulation
rms: Root Mean Square
SiC: Silicon Carbide

SMPS: Switching-Mode Power Supply

THD: Total Harmonic Distortion

VSC: Voltage Source Converter

VSI: Voltage Source Inverter

WBG: Wide Band Gap

Chapter 1 Introduction

1.1 Background

The aerospace industry has experienced rapid growth over the past decades and the fuel costs account for a significant portion of the total operating costs [1]. To improve the efficiency of an aircraft system, there is a trend to replace the traditional non-electrical systems, such as hydraulic, pneumatic, and mechanical systems with electrical systems. The more electric aircraft (MEA) concept has shown promising results in the reduction of fuel consumption, which is evident in both the Airbus A380 and the Boeing 787, where significantly more electrical systems are deployed as compared with the previous generations aircrafts [2, 3]. MEA will become a norm in future[4-6], as depicted in the technological roadmap shown in Figure 1.1.

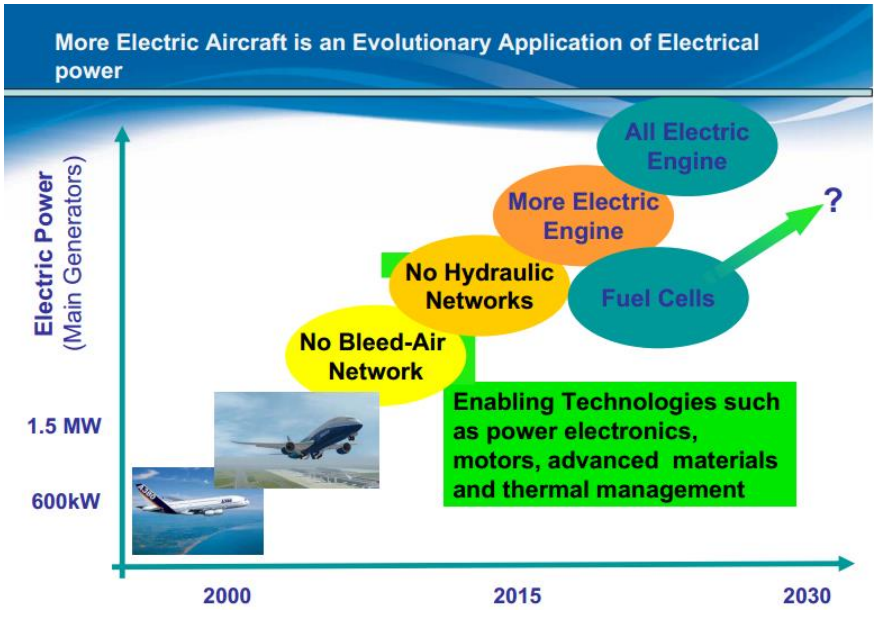

Figure 1. 1 Roadmap for future civil aircraft development [7]

With more and more electrical systems being deployed, power converters

that link power sources and electrical loads, will become unavoidable and development of HPDC is an important technology that is critical to the success of MEA [8]. Pulse width modulation (PWM) technique with high switching frequency is commonly employed in HPDC design but it results in large harmonic contents [9]. To comply with the relevant power quality standards, such as RTCA DO-160, ISO 1540-2006, Boeing D6-44588 and Airbus ABD-0100, the total harmonic distortion (THD) must be kept within 3%. Therefore, an output filter is needed [10] so that the THD and the first 40^{th} current harmonics can be controlled within the limit [11].

Also, due to the space constraint, carrier capability, and harsh environment in aircraft, the primary design goals of HPDC system are size and weight reduction, as well as thermal management. It is well known that the weight of the passive components account for 30% - 50% of total weight of HPDC system [12], especially harmonic and electromagnetic interference (EMI) filter inductors. Therefore, design optimization of these inductors has become important because of the limited space and carrier capability requirement.

Recently, the wide bandgap (WBG) semiconductor devices such as silicon carbide (SiC) and Gallium Nitride (GaN), have attracted increasing attention and become a promising candidate for aerospace power converter. With the ever increasing switching frequencies in HPDC systems, silicon carbide (SiC) is regarded as the next-generation material for the WBG power devices intended for high power density and high temperature applications, such as EV and MEA [13]. The ability of SiC devices to switch at high speed paves the way for SiC

power converters with higher operating frequency, and thereby reducing the size of passive components to improve the power density significantly [14]. The design challenges exist because of much different operating conditions than Si devices, and much research work on LCL filters has been reported, such as LCL filter designs for lower power (≤10 kW) lower switching frequency (≤ 10 kHz) [15, 16] or high power (≥50 kW) low switching frequency (≤ 20 kHz) [17] converters. Therefore, the conventional passive filter design should be revisited because of high switching frequency, high power, and high operating temperature (70 ^{o}C) [18] requirements for MEA.

1.2 Research motivation and objective

Given the space and weight constraints in an aircraft, compact and efficient power converter design is important [19]. The design of HPDC has numerous challenges, such as high-power semiconductor devices, control topology, heatsink and magnetic components, just to name a few. Firstly, the fast switching power semiconductor devices, such as MOSFET with silicon carbide (SiC) and gallium nitride (GaN) device, can reduce the size and weight of power converters, especially for magnetic components [20]. Secondly, as the modulation scheme generates harmonic currents and high-frequency switching of devices also bring the EMI problems into the system [21], both the harmonic and EMI filters are needed to meet the power quality and electromagnetic compatibility (EMC) requirements. Design and optimization of harmonic and EMI filters can be rather challenging, as the filters must attenuate the harmonics at low frequencies as well

as the EMI at high frequencies. Also, to improve the power density, interleaved converter topologies with phase-shifting of the carrier waveform of individual converters are used to reduce the harmonics [22], which leads to the need of coupled inductors to suppress the circulating current between two individual converters.

Therefore, the magnetic components including inductors of harmonic filter, CMCs of EMI filter, coupled inductors between two interleaved three-phase inverters require careful design consideration. As the magnetic components account for nearly half of the total weight of a power converter, the weight reduction of these magnetic component become a critical design parameter to realize HPDC. Hence, the SiC power converter operating at high switching frequency leads to new challenges for magnetic components design, for examples:

- Multi-field design approach, such as electric-magnetic-thermal-fluid.
- Novel methods to reduce the weight and size of the filter, such as magnetic integration, filter and converter topology.
- High frequency characteristics of CMC and CI.

1.3 Major contributions

The major contributions of the research work presented in the thesis are summarized as follows:

- Firstly, a LCL filter design methodology that targets for high power density converter with high switching frequency is proposed, as

opposed to conventional LCL filter design intended for converter operates at low switching frequency:

- Secondary, a novel magnetic integration of the LCL filter with delta-yoke core is proposed, designed and tested; which has demonstrated a 10% reduction in core size as compared to conventional rectangular yoke core;
- Thirdly, comprehensive circuit-level and finite element method (FEM) simulations are carried out to optimize the overall weight reduction of harmonic filters and coupled inductors for multiple parallel converters;
- Finally, multi-physics optimization is applied to take into consideration of weight reduction and thermal management a common mode choke (CMC) in coupled inductor and EMI filter designs, which is intended for high temperature environment.

1.4 Thesis organization

This Thesis is organized into the following 7 chapters.

Chapter 1 presents the background, motivation, and objective.

Chapter 2 reviews power density of HPDC, THD reduction methods, material of magnetic component, output harmonic filter, and thermal management of magnetic components.

Chapter 3 optimizes the LCL filter design using a multi-field approach with electrical circuit analysis of HPDC, magnetic circuit analysis of inductor with

finite element method (FEM), and thermal analysis of inductor with computational fluid dynamics (CFD) and JENOPTIK thermography camera.

Chapter 4 explores magnetic integration of LCL filter to reduce the filter weight. The delta-yoke core is proposed to replace the conventional rectangular yoke core.

Chapter 5 looks into parallel interleaved two three-phase voltage source converters to reduce the filter weight and size. Comprehensive harmonic analysis and THD are compared for two-level, three-level, and five-level converters.

Chapter 6 evaluates the characteristics of the common-mode choke (CMC), such as common-mode (CM) and differential-mode (DM) inductances, magnetic core saturation with CM and DM currents, the parasitic capacitances of the turn-to turn and the turn-to-core, and different core structures. In addition, the thermal management of CMC is also investigated under different conditions.

Chapter 7 concludes the thesis, and recommends potential works that are worth exploring.

Chapter 2 High Power Density Converters and Passive Filters

In this chapter, the up-to-date and key issues in HPDCs and passive filters: power density barrier, harmonic and common-mode voltage reduction method, material selection, optimization of output harmonic filter, and thermal management in MEA are reviewed.

2.1 High power density converter for more electrical aircraft application

2.1.1 Overview

The back to back HPDC for aerospace application consists of AC to DC rectifier and DC to AC inverter. This thesis focuses mainly on DC to AC inverter as indicated in Figure 2.1, with emphasis in advanced harmonics filter and CMC of EMI filters designs.

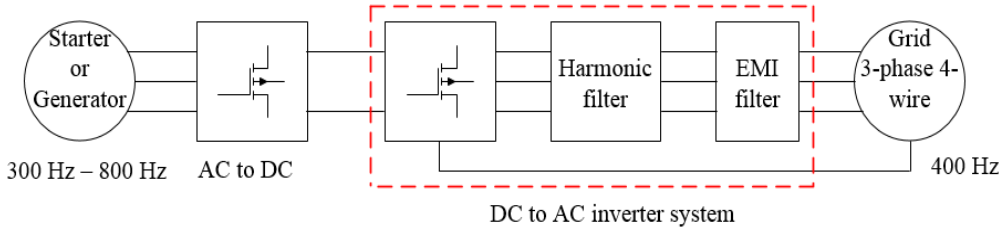

Figure 2. 1 Back to back high power density converter for aerospace application

2.1.2 Power density barrier

Requirement for future power electronics converter includes lower weight, volume, higher efficiency, reliability with lower cost, and mean time between failures (MTBF) as shown in Figure 2.2 [23]. In More Electric Engine (MEE), compactness is paramount for fuel and space saving, especially in aircraft applications. While there is no clear overview on the attainable converter's power

density at this moment, there are several key areas that enable the increase in power density: power devices and topology, thermal management, and passive technology.

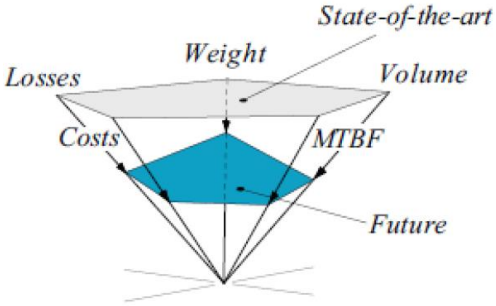

Figure 2. 2 Key performance parameters in the development of power converter [23]

Power devices and topology determine the loss profile of a converter, and thus the amount of heat to be dissipated by the cooling system. Recent advances in wide band gap power devices technology such as SiC and GaN power devices enable lower losses and higher operating junction temperature. These result in smaller and lighter cooling systems for thermal management [23]. In general, the components that contribute significantly to converter's volume and weight are the cooling system and passive components. Trade-off between them can be clearly seen as a function of switching frequency, device losses, and filter losses. Higher switching frequency results in added requirement of cooling system, but smaller passive components. Therefore, finding optimal switching frequency for highest possible power density is important to maximize the performance of any power converter.

2.1.3 Methods with the improvements of power density

There are several methods to improve power electronic converter density. From the system level perspective, optimization of HPDC system with different converter topologies [24, 25]. For the subsystem's perspective, a comprehensive design of passive filter, or heatsink can also be optimized to reduce the weight and size under certain operating conditions [26]. From the components perspective, on one hand, multi-domain design can be optimized to improve power density, such as electric-magnetic-thermal for magnetic component design [27, 28]. On the other hand, magnetic integration is also one of an effective method to reduce the core weight [29-33]. Besides, advanced modulations are used to reduce the harmonics, then the losses decrease, and the lighter heatsink or smaller passive filter will be required as well [34, 35].

2.1.4 THD and standards

Table 2. 1 RTCA DO-160 harmonic limits [11]

Harmonic order	**Limits**
3, 5, 7	$I_3 = I_5 = I_7 = 0.02I_1$
Odd triplen-9,15,21,27,33,39	$I_h = 0.1\, I_1/h$
11	$I_{11} = 0.1I_1$
13	$I_{13} = 0.08I_1$
Odd non triplen-17 and 19	$I_{17} = I_{19} = 0.04I_1$
Odd non triplen-23 and 25	$I_{23} = I_{25} = 0.03I_1$
Odd non triplen-29,31,35,37	$I_h = 0.3\, I_1/h$
Even-2 and 4	$I_h = 0.01\, I_1/h$
Even > 4 (6,8,10,12,…,40)	$I_h = 0.0025I_1$

With the use of PWM modulation on a three-phase inverter in Figure 2.3, the harmonic filter is necessary for the grid interface converter. This filter is essential to suppress the current harmonics as shown in Figure 2.4, and to comply

with the relevant power quality standards, such as RTCA DO-160, ISO 1540-2006, Boeing D6-44588 and Airbus ABD-0100, the total harmonic distortion (THD) must be kept within 3%. In addition, the first 40th harmonics are required to satisfy the individual current harmonic limits, as tabulated in Table 2.1.

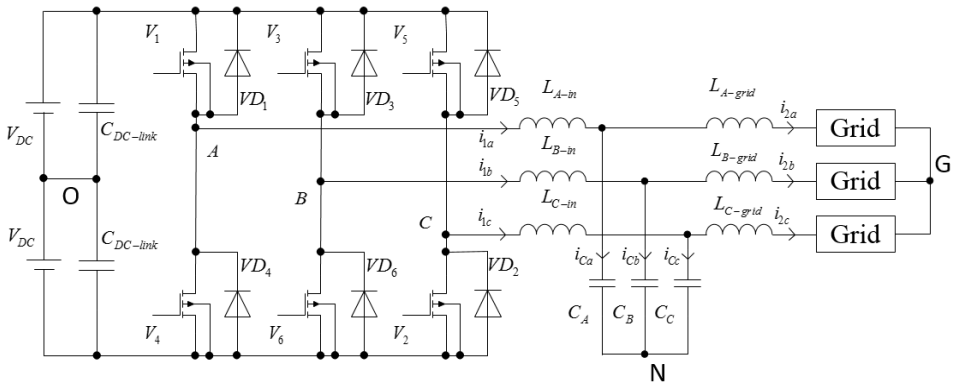

Figure 2. 3 LCL filter with three-phase inverter for grid-connected applications

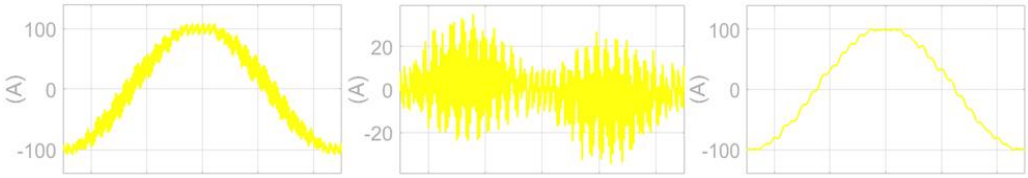

(a) (b) (c)

Figure 2. 4 Current waveform of LCL filter, (a): inverter-side current; (b): capacitor current; (c) grid-side current.

2.1.5 Filters for hamronic and CM voltage reduction

There are two main types of filters to reduce the harmonics. One is to use a passive power filter (PPF), and the other is to use an active treatment. Passive filter plays an important role in harmonic reduction of aircraft power grid [30]. For aerospace applications, passive filter design includes electric-magnetic-thermal-fluid analysis, which is necessary for the development of HPDC [36]. Active treatment uses additional device by modulating and controlling the circuit to decrease or cancel the harmonic content, such as active power filter (APF)

technology [37]. Besides, the combination of active and passive components composes hybrid APF (HAPF), and different topologies have been proposed, such as series APF and shunt PPF, shunt APF and shunt PPF, and APF in series with shunt PPF [38].

The passive EMI filter is to utilize inductors and capacitors to suppress the high frequency common mode (CM) voltage and current. To improve the power density of inverter system, compact EMI filter with size and weight considerations has become an important research topic [39].

Active filters use controllable devices to produce the voltage to cancel CM voltage, includes different modulation schemes, filter topologies, and inverter configurations [40-42]. One of the popular methods is the adoption of multilevel converter to reduce CM voltage.

2.2 Material of inductor core and copper wire

2.2.1 Magnetic material properties comparison

The general magnetic materials of interest are shown in Table 2.2, and there are mainly six kinds of materials, including amorphous, silicon steel, nano-crystalline, ferrite, powder iron, and powder core. The electromagnetic characteristics of magnetic materials such as saturation flux density, relative permeability, and core loss are given. Besides, the thermal conductivity, specific heat capacity, density, and continuous operating temperature are beneficial of magnetic component's cooling system design. The anisotropic thermal conductivities of amorphous metal, silicon steel, and nano-crystalline are

significantly higher along the laminations than across the laminations, and the cooling path can be optimized with thermal path anisotropy. Ferrite and powdered iron have relatively lower thermal conductivities. Magnetostriction is also a determining factor of inductor design if the frequency of interest is in the audible range of 20 Hz-20 kHz.

Table 2. 2 Magnetic material properties [43]

Magnetic Material Type	Manufacturer	Material	Composition	Bsat [T] @25 °C	Rel. Permeability (100C @20kHz)	Curie temp. [ºC]	Continuous operating temperature [ºC]	Thermal conductivity [W/(m K)]	Specific Heat Capacity [J/(K kg)]	Density [g/cm3]	Electrical Resistivity [μΩ m]	Lamination Thickness [mm]	Core Fill Factor	Magnetostriction [ppm]	Core Loss @0.1T, 20kHz [kW/m^3] 60μ for powder cores
Amorphous	Metglas	2605SA1	Fe-B-Si	1.56	600	395	150*	10***	540	7.18	1.37	0.03	0.83	27	70
Amorphous	Metglas	2605S3A	Fe-B-Cr-Si	1.41	35000	358	150*	10***	TBD	7.29	1.38	0.03	0.75	20	17
Silicon Steel	JFE	10NHF600	Fe-Si	1.88	600	700	150*	18.6***	536	7.53	0.82	0.1	0.9	0.1	150
Nanocrystalline	Vacuumschmelze	Vitroperm500F	Fe-based	1.2	13200	600	120*	10***	~500	7.3	1.15	0.02	0.7	0.5	5
Ferrite	Ferroxcube	3C93	MnZn	0.52	1800	240	140	3.5-5	~750	4.8	5x10^6	bulk	1	0.6	5
Powder Iron	Micrometals	Mix -26	Fe	1.38	72	-	<75**	4.2	TBD	7	TBD	bulk	1	TBD	630
Powder Core	Magnetics	MPP	Fe-Ni-Mo	0.75	14-550	460	200	TBD	TBD	8.2	TBD	bulk	1	TBD	45
Powder Core	Magnetics	High Flux	Fe-Ni	1.5	14-160	500	200	TBD	TBD	7.7	TBD	bulk	1	TBD	116
Powder Core	Magnetics	KoolMu	Fe-Al-Si	1.05	26-125	500	200	TBD	TBD	6.8	TBD	bulk	1	TBD	83
Powder Core	Magnetics	Xflux	Fe-Si	1.6	26-60	700	200	TBD	TBD	7.5	TBD	bulk	1	TBD	200
Powder Core	Chang Sung Corp.	MPP	Fe-Ni-Mo	0.7	26-200	450	200	TBD	TBD	TBD	TBD	bulk	1	TBD	65
Powder Core	Chang Sung Corp.	High Flux	Fe-Ni	1.5	26-160	500	200	TBD	TBD	TBD	TBD	bulk	1	TBD	100
Powder Core	Chang Sung Corp.	Sendust	Fe-Al-Si	1	26-125	500	200	TBD	TBD	TBD	TBD	bulk	1	TBD	76
Powder Core	Chang Sung Corp.	Mega Flux	Fe-Si	1.6	26-90	725	200	TBD	TBD	6.8	TBD	bulk	1	TBD	186
Powder Core	Arnold Magnetics	MPP	Fe-Ni-Mo	0.75	14-350	TBD	TBD	TBD	TBD	TBD	TBD	bulk	1	TBD	70
Powder Core	Arnold Magnetics	High-Flux	Fe-Ni	1.5	14-160	TBD	TBD	TBD	TBD	TBD	TBD	bulk	1	TBD	130
Powder Core	Arnold Magnetics	MSS	Fe-Al-Si	1	14-147	TBD	TBD	TBD	TBD	TBD	TBD	bulk	1	TBD	90
Powder Core	Arnold Magnetics	Fe-Si 6%	Fe-Si	1.5	14-147	500	200	TBD	TBD	TBD	TBD	bulk	1	TBD	240
Powder Core	Arnold Magnetics	Crystal-X	TBD	1.5	14-60	TBD	TBD	TBD	TBD	TBD	TBD	bulk	1	TBD	100
Powder Core	Ferroxcube	MPP	Fe-Ni-Mo	0.75	14-300	460	200	TBD	TBD	8.7	TBD	bulk	1	TBD	TBD
Powder Core	Ferroxcube	High-Flux	Fe-Ni	1.5	14-160	500	200	TBD	TBD	8.2	TBD	bulk	1	TBD	TBD
Powder Core	Ferroxcube	Sendust	Fe-Al-Si	1.05	26-125	500	200	TBD	TBD	7	TBD	bulk	1	TBD	83

*limited by the lamination epoxy, ** limited by thermal aging, *** along laminations, TBD – to be determined.

In summary, the selection of magnetic material is dependent on its properties and the intended operating conditions.

2.2.2 Magnetic core loss

The increase in magnetic core temperature with core loss is usually the key limitation for high frequency applications. The physics of magnetic core losses is rather complicated. In general, magnetic core losses mainly consist of a hysteresis loss, an air-gap loss, an eddy-current loss, and excess loss.

To align and rotate magnetic moments is required to consume the energy, which results in hysteresis loss.

At low frequency such as 50 Hz or 400 Hz, the loss associated with the air gap of a three-phase coupled E-core inductor can be predicted as follows [44]:

$$W_g = 3GDFB_m^2 l_g, \ watts \tag{2.1}$$

where, $G = 0.155 \times 10^{-8}$ is a numerical constant; D is the core strip width (cm); F is the line frequency (Hz); B_m is the maximum core induction (Gauss); and l_g is the length of the air gap (cm).

Due to the resistivity of the core material, and a time-varying magnetic field, a voltage is generated and then it causes an eddy current flowing in a conductive core, which contributes to the eddy-current power loss (Ohmic loss or resistive loss).

The excess loss comes from the dynamic loss of the dynamic domains, since the magnetic domains are divided from each other by domain walls, and a

changing external magnetic field is required to move the domain walls, which leads to the dynamic loss [45].

2.2.3 Litz wire

For higher switching frequency, wide band gap devices are used, which brings high frequency harmonics and the skin effect can be significant. As an example, the skin depth at 60 kHz is

$$\delta = \sqrt{\frac{\rho_{Cu}}{\pi f \mu_0}} = \sqrt{\frac{1.724\times10^{-8}}{\pi\times60000\times4\pi\times10^{-7}}} = 0.2698\ mm \tag{2.2}$$

Hence, the Litz wire is a better choice for high frequency magnetic component design.

The DC Litz-wire resistance per meter is:

$$R_{\omega DC(\text{litz})} = \frac{\rho_{Cu}}{k\pi\left(d_l/2\right)^2} \tag{2.3}$$

An approximate expression of Dowell's equation F_R using Litz-wire for winding [45] is:

$$F_R \approx 1+\frac{5N_l^2k-1}{45}\eta^2\left(\frac{\pi}{4}\right)^3\left(\frac{d_l}{\delta_\omega}\right)^4,\ for\ \ \frac{d_l}{\delta_\omega}\le 2. \tag{2.4}$$

The porosity factor is given by outer diameter d_0 and inner diameter d_l as follows:

$$\eta = \left(\frac{d_l}{d_0}\right)^2 \tag{2.5}$$

Thus, the Litz-wire winding AC resistance is:

$$R_{\omega(litz)} = F_{\omega(litz)}R_{\omega DC} \tag{2.6}$$

The inductor's winding loss due to the fundamental current and all

harmonics current can be calculated with (2.7) and (2.8).

$$P_{\omega DC} = R_{\omega DC} I_L^2 \tag{2.7}$$

The harmonic winding loss factor is defined as the ratio of the total winding DC and AC power losses to the winding DC power loss:

$$F_{Rh} = \frac{P_\omega}{P_{\omega DC}} = 1 + \sum_{n=1}^{\infty} F_{Rn} \left(\frac{I_n}{I_L} \right)^2 = 1 + \sum_{n=1}^{\infty} \gamma_n^2 F_{Rn} \tag{2.8}$$

2.3 Review of output harmonic filter

2.3.1 Topologies of output harmonic filter

The passive filter has different topologies, such as L filter, LC filter, LCL filter, LLCL filter, LCL-LC filter, LTCL filter, and so on [17, 46-51]. Figure 2.5 shows the four main filter topologies.

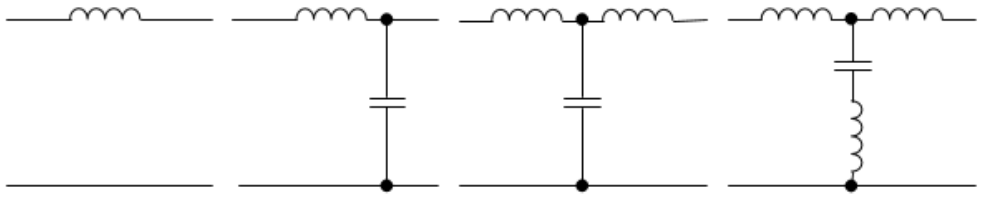

Figure 2. 5 Typical harmonic filters. (a) L filter. (b) LC filter. (c) LCL filter. (d) LLCL filter

The simplest structure uses an inductor connected between voltage source converter and grid to smooth the current. Although it has the least number of components, the heaviest weight and limited 20 dB/dec attenuation make L filter not attractive. LC filter with 40 dB/dec attenuation and lower weight are better option compared to L filter, but the L and C have a resonance, which degrades the performance of LC filter and it also needs to be damped by another damping circuit or virtual impedance damping [52]. To further reduce the total weight of

passive filter, the LCL is adopted, which have 60 dB/dec attenuation at high frequency and lowest weight compared to L and LC filter, and the resonance issue is dealt with virtual impedance damping [52] and no extra passive components are required. Therefore, even though an LCL filter requires a more complex control system to manage the LC resonance, it is much smaller in size compared to a simple L filter and LC filter [53], and the LCL filter is the most widely utilized and many other filter topologies are usually based on LCL filter.

2.3.2 LCL filter design guidance

There are some constraints for LCL filter between the VSC and grid-connected side to guide the design procedure, such as current tipple, switching frequency, filter size and thermal issue, reactive power requirement, resonance problem, and THD standard.

For the inverter side inductor L_{in} in Figure 2.3, the current ripple and the switching frequency are the dominant factors. On one hand, the current ripple requires bigger inductance and larger inductor size, on the other hand, these current ripples also lead to the higher loss and the larger inductance induces the voltage drop. The higher switching frequency results in smaller filter size, but it is more complex to choose the core material. Therefore, the inverter-side inductor is a trade-off between size and thermal to improve power density.

The presence of a capacitor reduces the total weight and size of LCL filter, but it creates a resonant problem that is to be dealt with, either actively by an extra capacitor current feedback loop, namely, a virtual resistance is inserted in series with the capacitor [54, 55], or passively by using a resistor to dampen filter

resonance [55, 56]. In addition, the filter capacitor absorbs ripple current, which consumes the reactive power that is normally limited to less than 5 % of system rated power [17].

The grid-side inductor attenuates the harmonics to meet the THD standard. There are two criteria for selection of filter capacitor and filter grid-side inductor. Firstly, the impedance of the grid-side inductor has several times larger than the filter capacitor impedance at the switching frequency. Secondly, the natural damped frequency of LCL filter should be within the digital controller range.

2.3.3 Magnetic integration

Magnetic integration is another effective way to reduce the filter weight and size. Magnetic integration technology can be categorized into decoupled integration and coupled integration, according to the coupling effect between each magnetic cores The flux linked by each magnetics windings of the decoupled magnetics integration is independent, and the same characteristic with previous discrete magnetics is kept; and there is coupling effect among the flux linked by each magnetics winding when using coupled magnetics integration, so the characteristics of the previous magnetics will change [29].

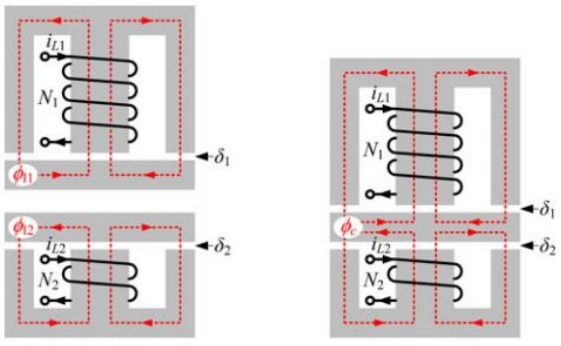

(a) (b)

Figure 2. 6 Core structures of the two inductors for a single-phase LCL filter. (a) Discrete inductors. (b) Integrated inductors. [31]

Figure 2.6 presents the decoupled integration of two inductors of LCL filter, and the selection of the common core between two inductors needs to decrease the coupling side effect.

Figure 2.7 shows the coupled integration of LCL filter, and the coupling effect in the central leg is effectively used and equivalent to inserting the third inductor of LLCL filter into the filter capacitor branch loop.

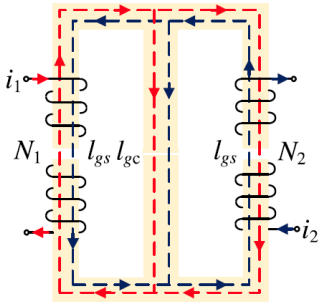

Figure 2. 7 Structure of magnetic integrated LLCL filter [33]

2.4 Thermal management

Due to smaller cooling surface area and larger power loss per unit volume of high density magnetic component, thermal management becomes one of the key design issues. High density magnetic components are widely used in many applications, such as aerospace and automotive power conversion systems [27, 28], where size and weight of magnetic components are major design considerations.

In general, there are three methods for thermal analysis of magnetic components, namely thermal FEM analysis, numerical computational fluid dynamics (CFD), and analytical equivalent thermal circuits [57-61]. Both of thermal FEM and numerical CFD are time consuming. The analytical approach

is computational efficient but it requires initial information. Usually, a hybrid approach with a combination of these methods can be used to model and predict the temperature rise of magnetic component.

There are several methods to cool the magnetic component, such as natural air cooling, forced air cooling, and liquid cooling. The surface power loss density ψ and the thermal resistance R_{Th} of an inductor are given by:

$$\psi = \frac{p_{cc}}{A_{sur}} \tag{2.9}$$

$$R_{Th} = k\frac{l}{A_{sur}} \tag{2.10}$$

where P_{cc} is the sum of core loss and copper loss, A_{sur} is the outer surface area of an inductor, k is the thermal conductivity, and l is length of the core. P_{cc} can be determined by:

$$p_{cc} = p_{out} = hA_{sur}\Delta T = \frac{\Delta T}{R_{Th}} = \frac{k}{l}A_{sur}\Delta T \tag{2.11}$$

Under the standard operating conditions specified in [45], the temperature rise of the inductor is related to the loss and the outer surface area by

$$\Delta T = 450\psi^{0.826} = 450\left(\frac{p_{cc}}{A_{sur}}\right)^{0.826} = 450\left(\frac{p_{core} + p_{copper}}{A_{sur}}\right)^{0.826} (^{\circ}C) \tag{2.12}$$

From (2.12), the following are contributing factors of the temperature rise:

(1) Total inductor loss (core loss and copper loss)

It can be reduced by:

- Reducing the operating flux density of core material;

- Adding multiple air gaps in the lamination to reduce air gap and proximity losses;
- Foil cutting for low resistance; and
- Shielding the air gap to reduce the copper loss (e.g. aluminum foil between coil and core).

(2) Total surface of inductor

It can be increased by:

- Use a bigger core;
- Increasing the space between stack cores;
- Increasing the space between coils; and
- Adding air duct between the coil and core, or between coil materials to increase cooling surface area.

(3) The heat transfer rate

It can be increased by:

- Forced air cooling such as adding a fan; and
- Liquid cooling such as using heatsink.

Chapter 3 LCL Filter Design with Size and Thermal Considerations

In this chapter, a comprehensive design approach of LCL filter with size and thermal considerations is described, which involves electrical-magnetic-thermal-fluid design optimization.

3.1 Introduction

Adopting more efficient electric technologies in the aircraft industry has been gaining attention with the objectives to decrease fuel consumption and reduce environmental impact. The backbones of more electric technologies are power converters to interface between loads and power grids. For aerospace applications, these power converters must be both compact and light, and hence, realization of HPDC is necessary [8, 19].

PWM technique with high switching frequency is commonly employed in HPDC design but it results in large harmonic contents [9]. To comply with the relevant power quality standards, such as RTCA DO-160, ISO 1540-2006, Boeing D6-44588 and Airbus ABD-0100, THD must be kept within 3%. Therefore, an output filter is needed [10] so that the THD and the first 40th current harmonics can be controlled within the limit [11].

With the ever-increasing switching frequencies in HPDC systems, silicon carbide (SiC) is regarded as the next-generation WBG power devices intended for high power density and high temperature applications, such as EV and MEA [13]. The ability of SiC devices to switch at high speed paves the way for SiC

power converters with higher operating frequency, and thereby reducing the size of passive components to improve the power density significantly [14].

For all the filter configurations, LCL filter is the most popular choice in grid-connected power converter systems for its excellent performance. Much research work on LCL filters have been reported, such as LCL filter designs for lower power (≤10 kW) lower switching frequency (≤ 10 kHz) [15, 16] or high power (≥50 kW) low switching frequency (≤ 20 kHz) [17] converters. Also, issues related to resonant problems [62-64], control [65-69] and magnetic integration [30, 31] of filters have also been well reported in the literatures. However, compact LCL filter design targeted for HPDC with both size and thermal considerations has not been well studied, especially for high power (≥50 kW) and high switching frequency (≥ 60 kHz) converters. Since high fundamental current and most of the harmonics are generated at the inverter-side of the converter [70, 71], a balance between thermal handling and size of the inverter-side inductor will be the key factor to contribute towards the compactness of the HPDC. It is well-known that the inverter-side inductor is the main heat source of the filter, mainly contributed by the air-gap and core losses. Also, the size of inverter-side inductor of the LCL filter has a direct impact on the power density of HPDC. Although single phase UI ferrite cored inductors can achieve high inductance with high operating temperature [15], but ferrite is prone to core saturation and hence, operates at relatively lower magnetic flux density, which needs large core size and prevent it being used for HPDC applications. Also, ferrite is structurally brittle, that making it a poor candidate for inductor that needs to handle very high

power [72]. The no air-gap amorphous core has been adopted for 20 kHz switching frequency with IGBT switches [17], whereas the focus is mainly on high system efficiency without air-gap loss or thermal issue, but it requires a larger margin for inductor design. When power density, system efficiency and thermal are all to be considered, design optimization of inductor becomes crucial and special design attentions are needed to achieve both compactness and thermal requirements. Hence, a comprehensive study of the relationships of inductor weight, core width and total surface area with respect to air-gap length become important for an optimal design of inductor to meet the size and thermal requirements, which will be the focus of this chapter.

A two-level, three-phase and three-wire inverter, as shown in Figure 2.3, uses sinusoidal pulse width modulation (SPWM) method, is adopted as a design case study. The chapter will be organized as follows: firstly, the trade-off between inverter loss and switching frequency with heatsink limitation will be presented. The design procedure of LCL filter will also be briefly described. Then, the optimization with the customized Amorphous E-cored inductors based on FEM simulation is presented in detail. Thermal consideration of the inverter-side inductor design will be elaborated and analyzed. Finally, the designed LCL filter is experimentally validated with conclusions.

3.2 50 kW HPDC Prototype

Figure 3.1 shows the prototype of the 50 kW HPDC with a weight of 1.9 kg. Heatsink design of an inverter is one of the key considerations for a high power

and high efficiency converter [73]. Considering the high ambient temperature environment in aircraft and losses of SiC devices for high power applications, liquid cooling is an attractive option for thermal management of power electronic components [18] as well as high power density requirement [39]. For most applications, the cooling system operates at 5 - 40 ^{o}C and ANSYS Fluent is chosen as the simulation tool for the heat sink design. For aerospace applications with high ambient temperature environment, ANSYS Fluent analysis with computational fluid dynamics (CFD) will be co-simulated for heat sink design with different choices of coolants [18, 74].

To start with the LCL filter design, the loss of SiC module CAS120M12BM2 versus output power under varying switching frequency is measured with a WT3000 precision power analyzer (0.02% accuracy) and plotted in Figure 3.2 with room temperature. As expected, the SiC loss increases with higher switching frequency. Considering the limit and the margin of the heatsink in Fig. 3.1 and the 150 ^{o}C junction temperature limit of the SiC module CAS120M12BM2 [18], the switching frequency of 60 kHz is found to be a suitable frequency for the HPDC system design. Hence, the selected switching frequency will be used for the LCL filter design.

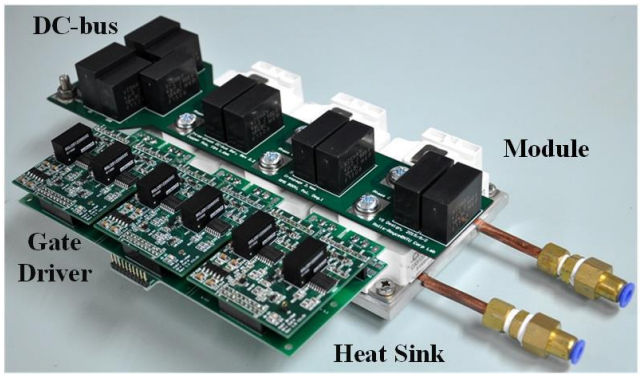

Figure 3. 1 Prototype of the in-house designed 50-kW HPDC.

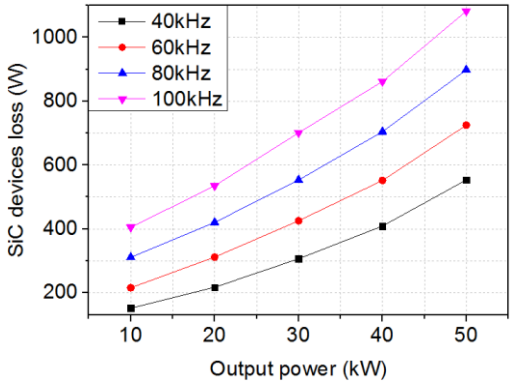

Figure 3. 2 SiC device loss versus output power under different switching frequencies.

3.3 LCL filter design and harmonic analysis

3.3.1. Inverter-side inductor

Since the inverter system shown in Figure 2.3 uses the sine-triangular modulation, the amplitude of the inverter phase voltage V_{AG} based on the Bessel functions is given [75], and the phase voltage is composed of a dc offset, fundamental and baseband harmonics, carrier harmonics and sideband harmonics. It can be shown that the most significant harmonic is around switching frequency and multiples of switching frequency. In a 3 phase 3 wire system, the maximum peak to peak current ripple at the inverter output is [76]:

$$\Delta I_{L\max} = \frac{2 \cdot 2V_{DC}}{3L_{in} f_{sw}}(1-M)M \tag{3.1}$$

where M is the SPWM modulation index.

The technical specifications of high power density inverter are presented in Table 3.1. For a typical maximum allowable current peak to peak ripple of 20 % on the inverter-side [77], the inverter-side inductance is determined by:

$$L_{in} = \frac{4V_{DC}}{3\Delta I_{L\max} f_{sw}}(1-M)M = 46.9\,uH \tag{3.2}$$

The inverter-side inductor is mainly for smoothing the switching frequency current ripple. To increase the power density, the silicon-carbide (SiC) CAS120M12BM2 MOSFET is selected so that switching frequency can be pushed to 60 kHz or higher. According to (3.1), given the same maximum current ripple, the inverter-side inductance can be reduced with a higher switching frequency and results in smaller core size. On the other hand, higher current (72.5 A RMS) and higher switching frequency current ripple cause more losses and their impacts on the temperature rise of inverter-side inductor L_{in} have to be carefully considered.

Table 3. 1 Technical Specifications of the Inverter

Parameter	Variable	Value
DC input voltage	$V_{DC\text{-}input}$	± 375V
AC output voltage	$V_{AC\text{-}output}$	230V (phase to neutral)
Output voltage frequency	f_0	400 Hz
Switching frequency	f_{SW}	60 kHz
Output power	P	50 kW
Inverter side inductor	L_{IN}	55 μH
Capacitor	C	5 μF
Grid side inductor	L_{GRID}	33 μH

3.3.2. Capacitor

Large capacitance provides good filtering of high frequency ripple but causes higher reactive power and shifts the power factor. Normally this reactive power is kept within 5 % of total system power rating [78]. Since the base impedance Z_{base} can be determined with line-to-line RMS voltage $V_{ll,rms}$ as follows:

$$Z_{base} = \frac{V_{ll,rms}^2}{P_{rating}} \tag{3.3}$$

Then the base capacitance C_{base} can be calculated by:

$$C_{base} = \frac{1}{\omega Z_{base}} = \frac{1}{2\pi f_0 Z_{base}} \tag{3.4}$$

Therefore, the maximum capacitance can be derived from as follows:

$$C \le 0.05 \cdot C_{base} = \frac{0.05 \times 50000}{2\pi 400 \times (230\sqrt{3})^2} = 6.3\,\text{uF} \tag{3.5}$$

A standard off-the-shelf 5 μF capacitor is chosen to fulfill (3.5). Usually the size and weight of the capacitors are less than 10% and 5% of the total size and weight of the LCL filter, respectively. Hence, the focus in this paper will be on design of the inductors to achieve overall size and weight reduction of the LCL filter.

3.3.3 Grid-side inductor

The grid-side inductor L_{grid} also suppresses the current harmonics. The sum of inductance of inverter-side and grid- side inductors depends on the voltage drop on the inductors, and normally it is controlled within 10 % of the base inductance L_{base} [65]:

$$L_{base} = \frac{Z_{base}}{\omega} = \frac{Z_{base}}{2\pi f_0} \tag{3.6}$$

The maximum total inductance is given by:

$$L_{in} + L_{grid} \le 0.1 \cdot L_{base} = \frac{0.1 \times (230\sqrt{3})^2}{2\pi 400 \times 50000} = 126.3\,uH \tag{3.7}$$

Based on the limit given in (3.7), through circuit simulation for THD requirement, 3D finite-element simulation, and resonant frequency requirement for the control part [53], the inverter-side and grid-side inductances are found to be 55 μH and 33 μH, respectively.

3.3.4 Simulated and measured output harmonics

With the component values of the LCL filter finalized, through circuit analysis, the simulated harmonic current components are presented in Figure 3.3 (a), which is in close agreement with the measured results, as shown in Figure 3.3 (b). With the DC input voltage and PWM modulation index unchanged, the output harmonics of the inverter are nearly invariant under different output power levels except the fundamental component.

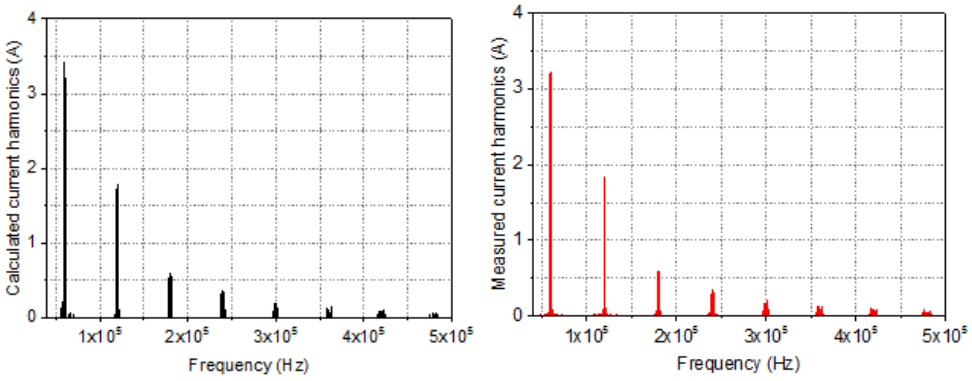

(a) (b)

Figure 3. 3 Current harmonics: (a) simulated (b) measured.

3.4 Core material and wire selection

3.4.1 Core material selection and structure design

Table 3. 2 Comparison of different magnetic materials

Physical property	Ferrite (Mn-Zn)	Nano-crystalline	Amorphous	Fine-met
Saturation flux density (T)	0.4	1.2	1.56	1.23
Initial relative permeability	1000-4000	15000-150000	3000-6000	>70000
Mass density (g/cm3)	5	7.2	7.18	7.2
Core loss without air gap (W/kg)	+	++	++++	+++
Continuous operation temperature (℃)	120	120	150	150

Symbols: Very high (++++); High (+++); Average (++); Low (+).

The inverter-side inductor of the LCL filter has to handle high switching frequency current ripple. To minimize the core size and losses, the comparison of magnetic properties of typical core materials is listed in Table 3.2.

From the power density perspective, it mainly depends on the ratio of saturation flux density to mass density. Hence, the amorphous core is the lightest and offers the best power density among the four magnetic materials. Based on FEM simulation, the ferrite (Mn-Zn) is found to be about 3 times heavier than amorphous cored inductor to achieve the required inductance of 55 μH. And the core losses are typically increasing for temperatures higher than 100 ℃. In addition, it is brittle and structurally not strong enough to support an inductor with high power rating [72]. Although Nano-crystalline and Finemet have lower core loss without air gap, comparing with amorphous, there is a need for larger air gap for high current application and results in fringing flux, which bring the air gap losses several times higher than the core loss [44, 79, 80], producing hot spot near the air gap. Nano-crystalline and Finemet cores are usually chosen for EMI filter design with lower current ratings from several mA to several hundreds

mA [81, 82]. Powdered magnetic materials [43] can be another option, as the magnetic flux density and mass density of some powdered cores are comparable to amorphous material. However, the core losses of these powdered cores are relatively higher than those of amorphous cores and their relatively lower permeability also requires more number of winding to achieve the same inductance, which increases the inductor size and introduces higher parasitic capacitance. In addition, not only weight, but also thermal limitations need to be considered for such a high frequency and high power density inductor design. The amorphous core has low core loss, higher saturation flux density (1.56 T) [17, 79, 83], wider operating frequency and relatively high operating temperature (up to 150 ℃). These desirable properties make amorphous core the most suitable choice for inductor design with weight and thermal constraints. The lamination factor of the core is about 0.9 and its physical dimensions are shown in Figure 3.4.

Three-phase inductor on an integrated core has an advantage in size reduction comparing with three separate single-phase inductors [84]. To avoid core saturation, a small air gap will be added between the two E-cores. EE core with central air gap has lower losses than EI core with side air gap, so three phase inductors on EE core will be adopted for the design. The three-phase core area product is given by:

$$A_p = 3\left(\frac{W_a}{2}\right)A_c \tag{3.8}$$

where W_a and A_c are the window area and the cross-section area of the core.

The maximum energy stored in the magnetic field (in the air gap) of the inductor W_m is:

$$W_m = 3\left(\frac{1}{2} L I_{L\max}^2\right) \tag{3.9}$$

The three-phase area product is given by:

$$\frac{3W_a A_c}{2} = \frac{3LI_{L\max}^2}{K_u B_{pk} J_m} = \frac{2W_m}{K_u B_{pk} J_m} \tag{3.10}$$

The core loss can be estimated by Fourier expansion of the magnetic flux density waveform [45]:

$$P_v = k_1 f_1^{a_1} B_{m_1}^{b_1} + k_2 f_2^{a_2} B_{m_2}^{b_2} + k_3 f_3^{a_3} B_{m_3}^{b_3} + \ldots = \sum_{n=1}^{\infty} k_n f_n^{a_n} B_{m_n}^{b_n} \tag{3.11}$$

where k_n, a_n, and b_n are the coefficients at the corresponding frequencies f_n (kHz), B_{mn} in tesla. The main core loss with smaller air gap comes from switching frequency current harmonics and times of switching frequency current harmonics. Besides, the relationship between core loss and flux density of amorphous core at 25 ℃ is given by the datasheet:

$$P_{core}(\mathrm{W/kg}) = 6.5 f(kHz)^{1.51} B(T)^{1.74} \tag{3.12}$$

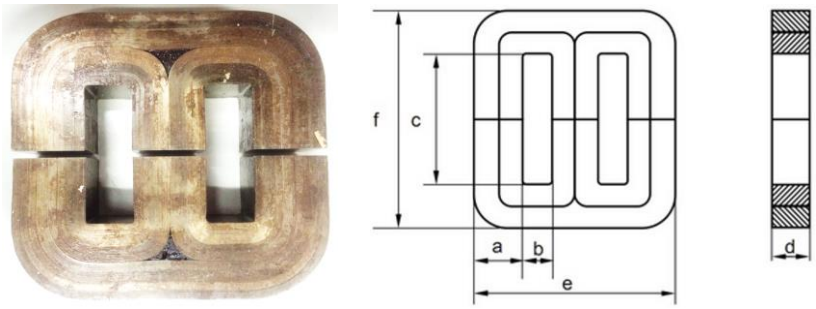

(a) (b)

Figure 3. 4 Physical layout (a) and dimensions (b) of three phase amorphous EE core.

3.4.2 Bobbin design

3D printing technology is adopted for the bobbin fabrication to tailor to our design for compactness. The fabricated bobbin has a thickness of 2 mm. The acrylonitrile butadiene styrene (ABS) material is chosen for the bobbin, as it can withstand very high temperature (210 - 215 ^{o}C) and a relatively low density. To reduce the fringing flux of the air gap, the bulges in the middle of bobbin are designed to separate the windings.

3.4.3 Winding design

Since the switching frequency is 60 kHz, the skin depth is

$$\delta = \sqrt{\frac{\rho_{Cu}}{\pi f \mu_0}} = \sqrt{\frac{1.724\times10^{-8}}{\pi\times60000\times4\pi\times10^{-7}}} = 0.2698\ mm \tag{3.13}$$

The wire current density is normally 4~5 A/mm^2, and the minimum wire radius (cross sectional area: πr^2) to handle 80 A current is 2.26 mm. The normal wire is expected to have high losses due to skin effect, therefore the high frequency (20 kHz – 100 kHz) AWG 36 Litz wire is chosen.

The approximate expressions of Dowell's equation for calculating the losses of Litz-wire [45], are shown from (2.3) to (2.8) in Chapter 2.

3.5 Inductor design

3.5.1 Magnetic core design

For magnetic core design, the typical window filling factor K_u is about 0.12 and peak flux density B_{pk} is about 90% of the saturation flux of the core material [45, 85, 114]. With the current density J_m of 4.5 A/mm^2 and known porosity

factor of the Litz wire, the product of window area and the core's cross-sectional area is given by:

$$W_a A_c = \frac{2LI_{L\max}^2}{K_u B_{pk} J_m} = \frac{2 \times 50 \times 10^{-6} \times (102.5 \times 1.1)^2}{0.12 \times 1.4 \times 4.5 \times 10^6} = 168.2 \ \ cm^4 \qquad (3.14)$$

Hence, a core with area product ($\geq$ 200 cm^4) is needed. However, the conventional inductor design based on area product and geometry coefficient only give a rough initial estimate of the core size. It is commonly used for the design of commercially available ferrite-cored inductor where lower core loss is the major concern and not the core size. For inductor intended for high power density applications, where high frequency harmonics core loss and high fundamental current air-gap loss can be significant, a comprehensive study of various design parameters, such as its weight, core width and total surface area with respect to air-gap length is necessary.

Given a specific cross-sectional area of E core and based on Biot-Savart Law, circular cross section gives the best uniformity of flux distribution, followed by square cross section and then rectangular cross section, as illustrated in Figure 3.5, and the magnetic flux density increases from the blue area to the red area. As a compromise for practical considerations of fabrication and weight, the square cross section core is chosen.

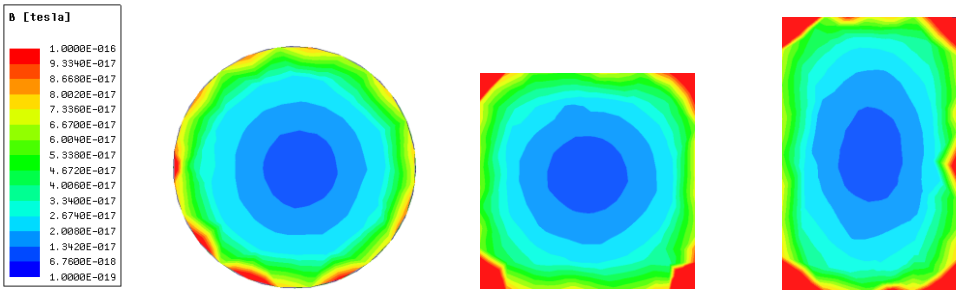

(a) (b) (c)

Figure 3. 5 Magnetic flux distribution comparison of different cross sections. (a) Circular. (b) Square. (c) Rectangular.

3.5.2 Trades-off between air gap and inductor weight

An air gap between two E cores is usually needed to avoid core saturation but at the expense of higher fringing flux that leads to increase in leakage inductance, which results in higher magnetic flux density in the core near the air gap. To determine an optimal air gap length, the core design with air gap length varying from 1 mm to 10 mm is evaluated.

Firstly, by keeping the inductance and maximum magnetic flux density to around 55 μH and 1.4 T, respectively; the relationship between the inductor weight and air gap length is shown in Figure 3.6 (a). It can be seen that the minimum weight achievable is about 3.75 kg, when the air gap length is about 5 mm. Figure 3.6 (b) shows the relationship between the core's width and the air gap length. It reveals that core's width cannot be reduced further if the air gap length is 5 mm or longer. At 400 Hz, the loss associated with the air gap of a three-phase coupled E core inductor can be predicted with (2.1) [44]:

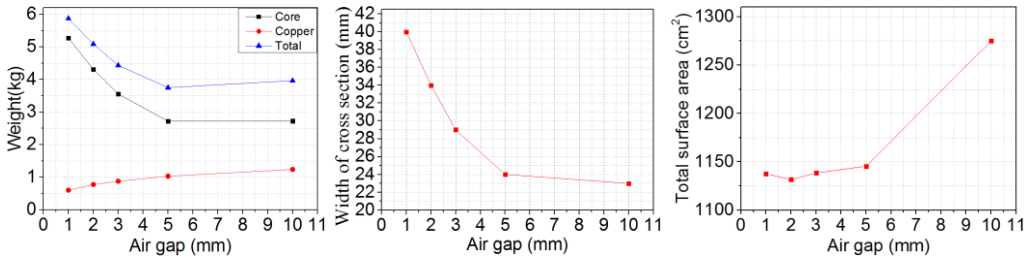

(a) (b) (c)

Figure 3. 6 (a) Inductor weight (b) width of core cross section and (c) total surface area, versus air gap length.

To reduce the fringing flux in an air gap, using many short air gaps instead of a long single air gap would help but there are other shortcomings. On one hand, the fringing effect increases the inductance, which can be calculated as follows [85]:

$$L = \frac{N^2}{R} = \frac{N^2}{R_c + R_g // R_f} = \frac{N^2}{R_c + R_g / F_f} > \frac{N^2}{R_c + R_g} \tag{3.15}$$

where N is the number of turns, R_c, R_g , and R_f are the reluctance for the core, air gap, and fringing flux, respectively.

Since the fringing factor F_f is defined by:

$$F_f = \frac{R_g}{R_g // R_f} = 1 + \frac{R_g}{R_f} = 1 + \frac{A_f / l_f}{A_c / l_g} > 1 \tag{3.16}$$

where A_f and A_c are the cross-section area of fringing flux and core. l_g and l_f are the length of air gap and fringing flux.

Therefore, the inductance of the three-phase inductor with many short air gaps will reduce the inductance. Also, many short air gaps increase the leakage flux, which further reduce the mutual-inductance and increase the maximum flux density. The flux distribution paths of a lumped air-gaps inductor can be grouped into three parts. The first is the main fluxes which go through the core and lead

to hysteresis loss, and then the by-pass fluxes that go across the winding window between two core legs and result in eddy currents and losses in winding conductors. The last is the fringe fluxes that go into the winding window area and come back into the core, which generates the air gap losses.

The expression of the three-phase inductance matrix is given by:

$$\begin{pmatrix} v_{L\_A} \\ v_{L\_B} \\ v_{L\_C} \end{pmatrix} = \begin{pmatrix} L_A & M_{AB} & M_{AC} \\ M_{AB} & L_B & M_{BC} \\ M_{AC} & M_{BC} & L_C \end{pmatrix} \cdot \frac{d}{dt} \begin{pmatrix} i_{L\_A} \\ i_{L\_B} \\ i_{L\_C} \end{pmatrix} \tag{3.17}$$

If the three inductances are symmetrical with no air gap, the self-inductance $L_A = L_B = L_C = L$, and the mutual-inductance $M_{AB} = M_{BC} = M_{AC} = M = -0.5L$. The inductance and maximum magnetic flux density derived from FEM simulation with one air gap and many short air gaps, respectively, are tabulated in Table 3.3. The inductance of the three-phase inductor with many short air gaps is reduced by 34.6%, comparing to one single air gap, and the core is also saturated easily due to the increase of in leakage flux.

Table 3. 3 Inductance and flux density comparison with two air gap designs

Air gap design	Inductance (μH)	Maximum flux density (T)
1 × 5 mm	53.4	1.344
5 × 1 mm	34.9	> 1.56

Therefore, many short air gaps are bad for magnetic design, while one larger air gap will suffer thermal problem. Although the larger surface area will increase the heat dissipation, the surface area remains rather constant for air gap between 1 mm and 5 mm shown in Figure 3.6 (c). The inductor with the air gap of 1 mm has the lowest loss due to minimum fringing flux.

With all the evaluations done earlier, the inductor with 1 mm air gap is finally chosen. The relationship between inductance and cross section width/number of turns is shown in Figure 3.7 (a). The relationship between flux density and air gap/number of turns is give in Figure 3.7 (b). The number of turns are estimated from the 1 mm air gap design and the width of cross section also can be calculated from the area product and Figure 3.7 (a).

Table 3. 4 Dimensions of the amorphous core

Parameters	a	b	c	d	e	f
Values (mm)	40	25	60	40	170	140

Table 3. 5 FEM simulated inverter-side inductor with amorphous core

Types	Phase A	Phase B	Phase C
Turns/phase	6		
Air gap (mm)/phase	1		
Inductance (uH)	54.9	55.7	54.9
BMAX (T)	1.44 (Excitation by 102.5*(1+(ripple) A)		

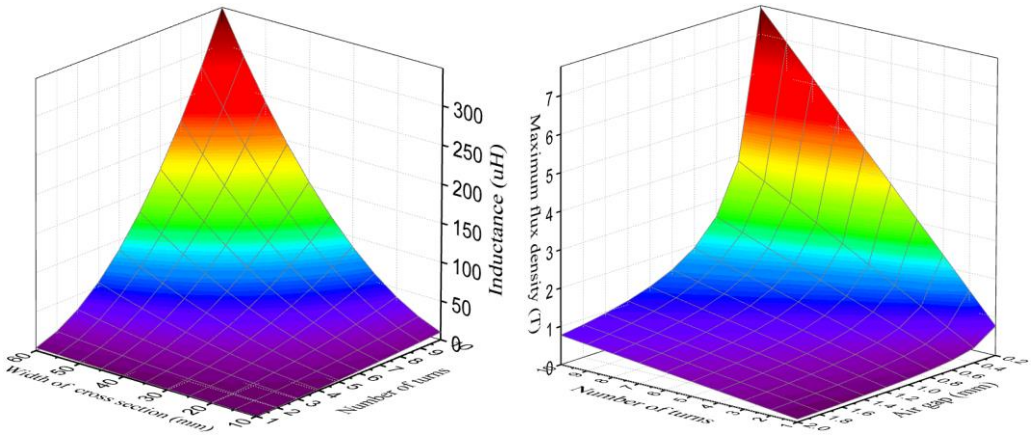

(a) (b)

Figure 3. 7 (a) Inductance versus width of cross section and number of turns and (b) flux density versus air gap and number of turns.

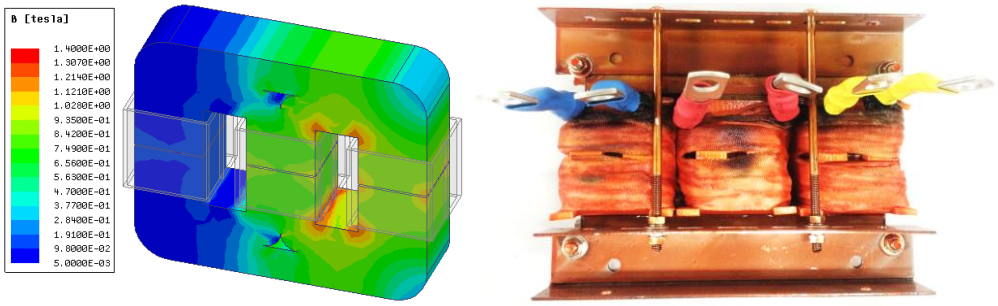

(a) (b)

Figure 3. 8 three-phase amorphous inductor (a) FEM simulation of the flux distribution and (b) fabricated prototype.

The dimensions of the final designed amorphous core with the parameters shown in Figure 3.4 (b) are given in Table 3.4. The inductance and flux density are simulated with ANSYS Maxwell and the results are shown in Table 3.5. The simulation uses the copper foil as it is impractical to draw 3D model of Litz wire. Figure 3.8 (a) presents the flux distribution of the three-phase amorphous inductor and Figure 3.8 (b) presents the three-phase inductor fabricated prototype.

3.5.3 Inductor losses analysis

The inverter-side inductor core loss is calculated based on the formula (3.12) with FEM. The copper loss is from Section 2.2.3. These losses are tabulated in Table 3.6.

Table 3. 6 Calculated power loss of inverter-side inductor

Power level (kW)	Current components (A)	Max. flux density (T)	Core loss (W)	Copper loss (W)	Total loss (W)
0	Only harmonics	0.446	319.9	0.25	320.15
10	All	0.738	324.7	0.60	325.30
20	All	0.940	340.6	2.41	343.01
30	All	1.144	347.1	5.41	352.52
40	All	1.313	349.3	9.62	358.92
50	All	1.442	350.5	15.03	365.53

Table 3.6 has two assumptions. Firstly, the actual core losses are influenced by the effects of leakage and fringing fluxes, non-sinusoidal current waveforms with many harmonics content, stacking factor of thin metallic ribbon, and thermal stress. The second is that the actual Litz wire is not ideal [86] because of the impacts of solder joints at both ends, unequal eddy current and proximity effects of each bundle, and the fringing flux of the air gap. Although the calculated losses may not be highly accurate, it does give us a good indication that core loss is much larger than the copper loss. The core loss mainly depends on high frequency harmonics and the copper loss is mainly determined by the amplitude of the fundamental current.

The air gap loss is also significant, which is generated by the fringing flux of air gap, that is perpendicular to the ribbon planes diverged from the main flux. Once the current is known, the maximum flux density can be analyzed. Finally, the 400 Hz air gap losses of inverter-side and grid-side inductor are obtained from the formula (2.1) and tabulated in Tables 3.7 and 3.8, respectively.

Table 3. 7 Air gap (1 mm) loss of inverter-side inductor at 400 Hz

Power (kW)	Current (A)	Max. flux density (T)	Air gap loss (W) (G= 0.155e-08)
10	14.49	0.561	23.42
20	28.99	0.719	38.46
30	43.48	0.937	65.32
40	57.97	1.142	97.03
50	72.46	1.314	128.46

Table 3. 8 Air gap (1 mm) loss of grid-side inductor at 400 Hz

Power (kW)	Current (A)	Max. flux density (T)	Air gap loss (W) (G=0.155e-08)
10	14.49	0.474	12.54
20	28.99	0.757	31.98
30	43.48	0.989	54.58
40	57.97	1.198	80.08
50	72.46	1.382	106.57

3.5.4 Thermal analysis

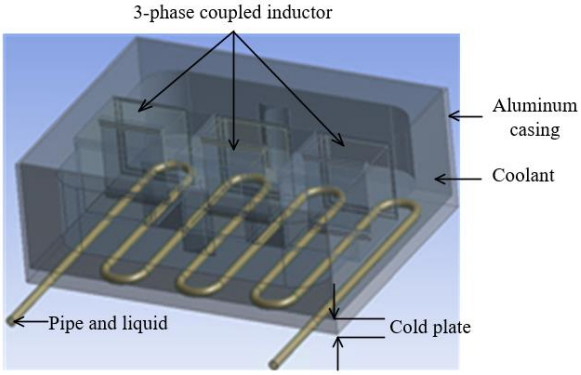

Figure 3. 9 Inductor with liquid cooling system.

The temperature rise associated with the losses of the inductor is the key limitation of inductor design targeted for high power density applications. As the core loss dominates the total inductor loss, temperature rise of the core is of major thermal consideration. The best approach is to design an inductor with the smallest possible core leading to acceptable losses and temperature conditions with possible cooling system, such as the liquid cooling system [39], as illustrated in Figure 3.9. The inductor's thermal circuit model is shown in Figure 3.10.

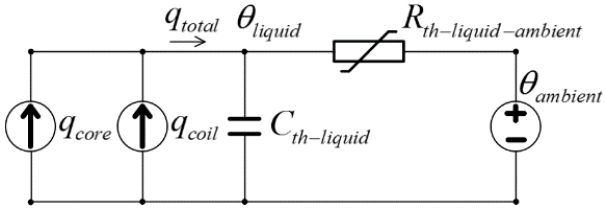

Figure 3. 10 Inductor thermal circuit model.

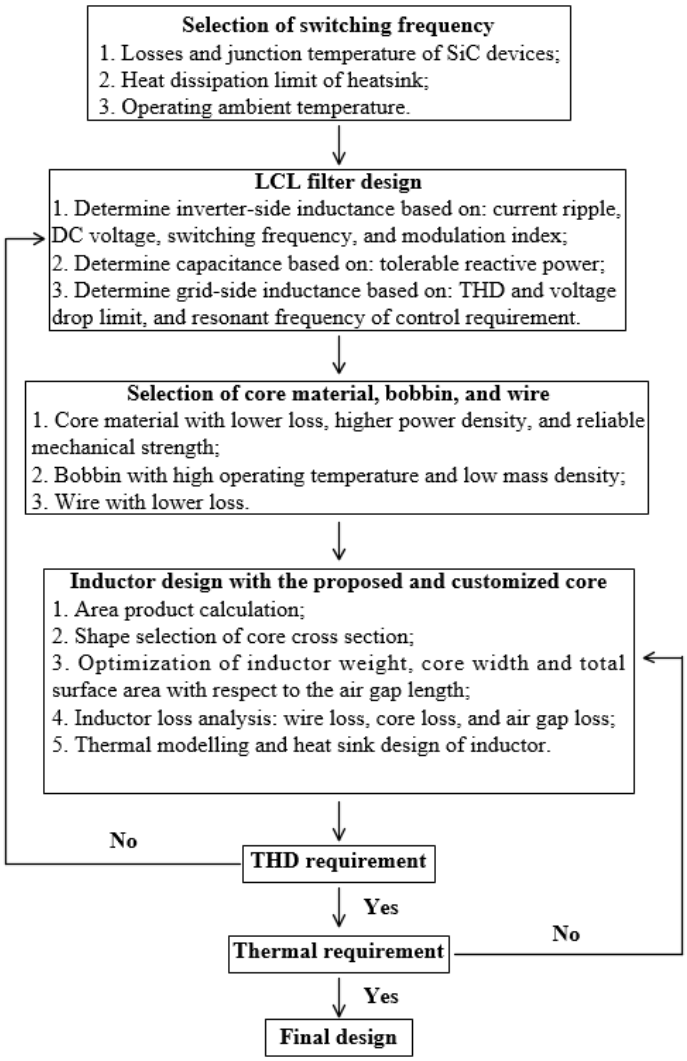

Figure 3. 11 Design flowchart for LCL filter in HPDC system.

q_{core} and q_{coil} are generated by core loss and winding loss respectively, q_{total} is the total loss. $C_{th\text{-}liquid}$ is the equivalent thermal capacitance of the liquid coolant, θ_{liquid} is the liquid coolant temperature, $R_{th\text{-}liquid\text{-}ambient}$ is the nonlinear liquid coolant to ambient thermal resistance and $\theta_{ambient}$ is the liquid ambient temperature.

3.5.5 Design methodology

To summarize the design process, a design flowchart as shown in Figure 3.11 gives a comprehensive design guide of the LCL filter in HPDC system with

both power density and thermal considerations.

3.6 Experimental verification

The three-phase two-level inverter system with the technical specifications given in Table 3.1 will be used for the verification of the LCL filter performance. The final designed LCL filter together with the inverter is shown in Figure 3.12. The inverter designed with three silicon carbide CAS120M12BM2 MOSFETs and the SPWM is driven by the TMS320F28335 microcontroller.

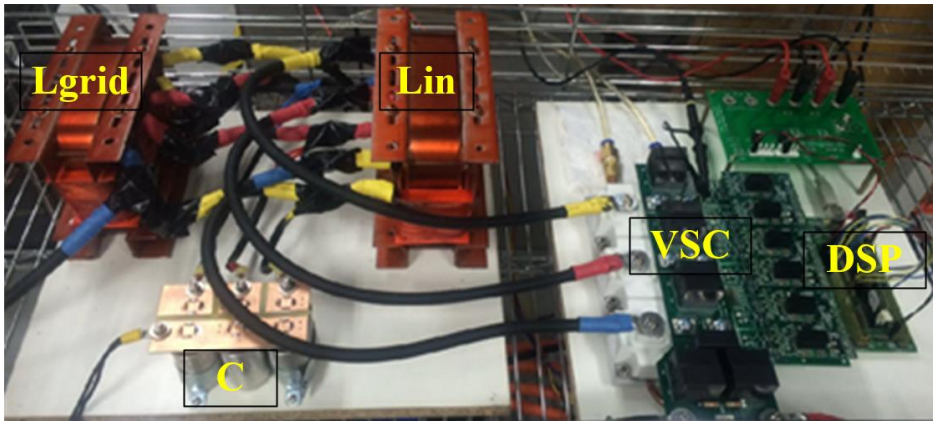

Figure 3. 12 Hardware of LCL filter with three-phase two-level inverter.

The WT3000 4-channel precision power analyzer will be used for the power measurement. Each channel has a voltage probe and a current probe. First channel measures the voltage and current at the DC input, which provides the input power. The other three channels measure the voltages and currents at each of the three phases of the AC output, which gives the output power. Knowing the input and output powers, the efficiency can be computed. Similarly, by measuring the powers before and after the LCL filter allows us to determine the loss in the LCL filter.

Figure 3.13 shows the measurement results obtained from WT3000 precision power analyzer. The measured output power and the efficiency of the inverter are 49.3 kW and 97.567 %, respectively.

Figures 3.14 (a) and 3.14 (b) show the measured inverter-side and grid-side current waveforms, respectively. The smoother grid-side current waveform indicates clearly that the LCL filter functions well. Also, both the inverter-side and the grid-side currents are analyzed in frequency-domain and their spectrum are plotted in Figure 3.15, which also clearly indicates that the switching frequency harmonics and the multiples of switching frequency harmonics are suppressed by LCL filter. The THD is reduced from 7.70 % to 1.54 %, which is less than 3 % and meets the standard requirement. The first 40th harmonic current also satisfy the individual current harmonic limits, as presented in Figure 3.16. Hence, the designed LCL filter has demonstrated its effectiveness to meet the power quality requirements.

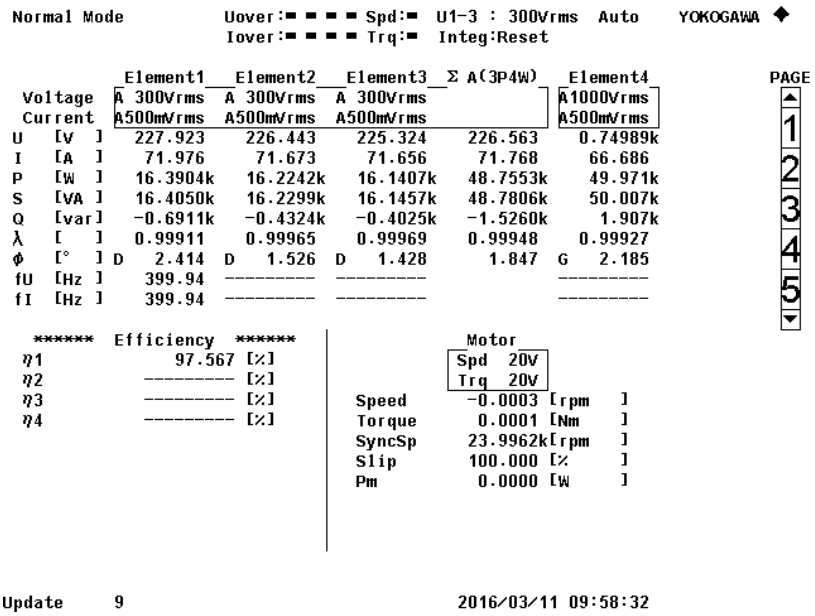

Figure 3. 13 Power analyzer data for 50 kW output power.

3.6.1 THD and lower order harmonics (≤ 40th order)

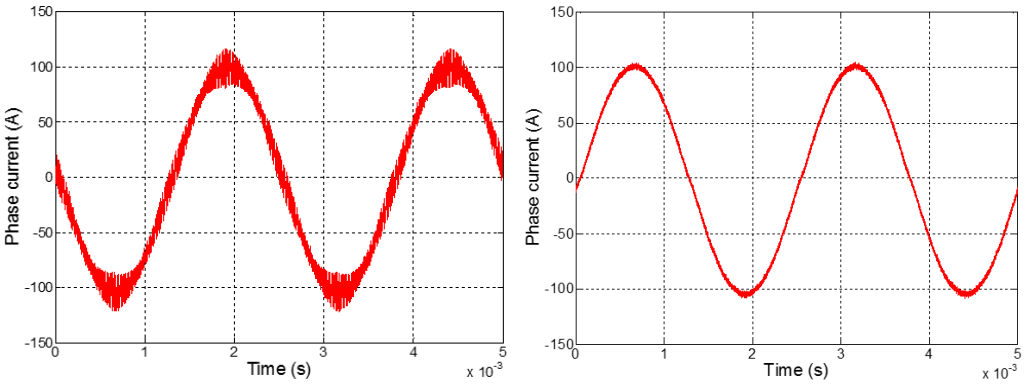

(a) (b)

Figure 3. 14 Experimental current waveforms of the inverter at 50 kW (a) inverter-side (b) grid-side.

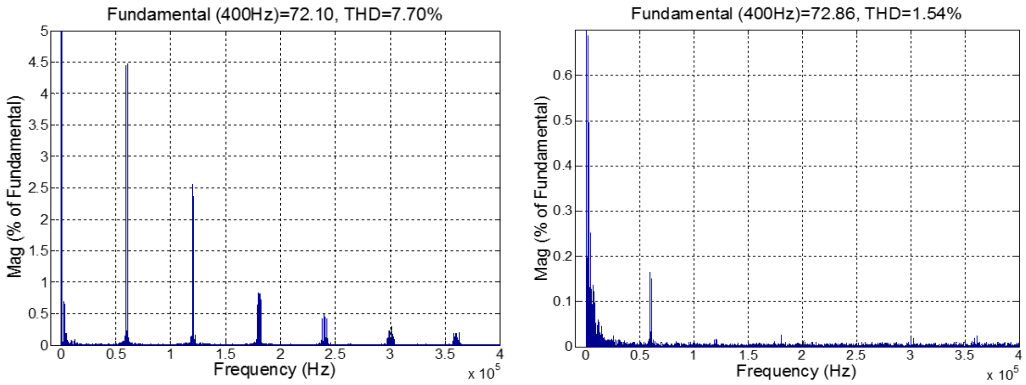

(a) (b)

Figure 3. 15 Current spectrum at 50 kW (a) Inverter-side and (b) Grid-side.

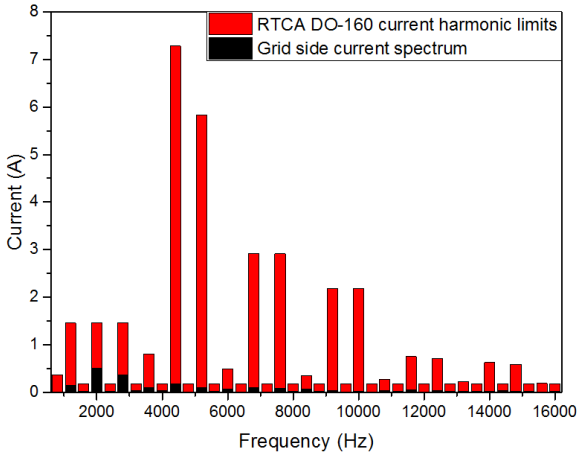

Figure 3. 16 Current harmonic limits for the first 40th harmonics at 50 kW.

3.6.2 Temperature measurement with natural air cooling

The thermal image of the LCL filter with the inverter operating of 20 kW is captured using the JENOPTIK thermography camera and presented in Figure 3.17 (a) with natural air convection. The hot spot temperature has stabilized after 100 mins of continuous operation and the temperature is less than the maximum allowable temperature of 150 °C. The hot spot occurs at the joint of the center leg for inverter-side inductor, as this joint has higher magnetic flux density, comparing to other parts of the core. The inverter-side has higher harmonics as compared to those at the grid-side. The measured temperatures of the inverter-side inductor versus time at 20 kW and 30 kW output powers are plotted in Figure 3.17 (b). The maximum temperature of inverter-side inductor with 30 kW power is slightly higher than 150 °C.

Under the full-load operation of 50 kW, liquid cooling system has been found to be a potential method to improve power density in aerospace application [18, 39]. Hence, for high power density requirements in aerospace application, air cooling alone is insufficient [18].

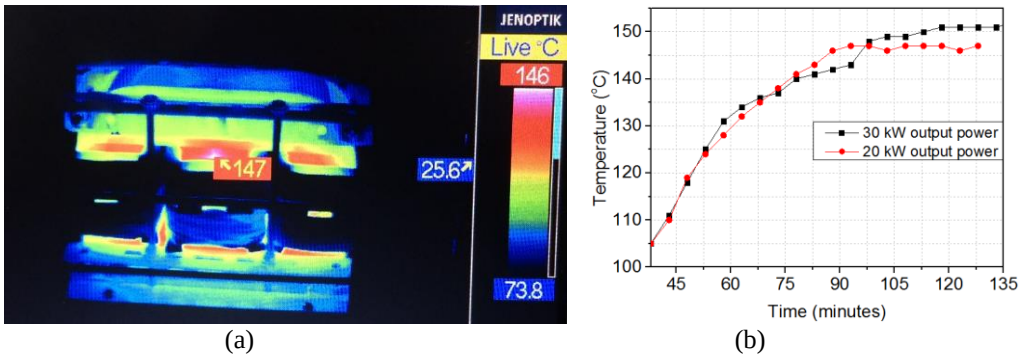

(a) (b)

Figure 3. 17 (a) Thermal images and (b) temperature versus time of the inverter-side inductor.

3.6.3 Inductor loss measurement

From the measurement results presented in Figure 3.17 (b), the designed inductor with air cooling unable to meet the thermal requirement at 50 kW full-load condition. The measured losses of inverter-side inductor, grid-side inductor and LCL filter with increasing output power are tabulated in Table 3.9, and also plotted in Figure 3.18 (b). As the loss of inverter-side inductor is a major contributor of the total filter loss, it will be good to know how the varying switching frequency affects its loss, which is shown in Figure 3.18 (a). It indicates that the loss is rather stable for switching frequency above 60 kHz. Based on the specified power analyzer's measurement accuracy of 0.02%, the expected worst cases errors of the measurement results are between 4 W and 20 W for 10 kW and 50 kW output power, respectively; which is acceptable for inductor loss between 200 W and 360 W. Figure 3.3 has demonstrated that the harmonics almost are the same for different output power. Moreover, the inverter-side inductor core loss is mainly produced from the switching frequency harmonics, multiples of switching frequency harmonics, and air gap loss. The larger fundamental current has little impact on the core loss from the formula (3.12). The loss of inverter-side inductor increases as a function of output power from 10 kW to 50 kW is quite close to the air gap loss shown in Table 3.7. The grid-side inductor core loss is mainly contributed by air gap loss, which is very close to the calculated loss in Table 3.8, since there are almost no high frequency harmonics presented in Figure 3.15 (b).

Table 3. 9 Measured inductor losses of LCL filter

Output power (kW)	Inverter-side inductor loss (W)	Grid-side inductor loss (W)	Total losses of LCL filter (W)
10	224.02	7.24	231.26
20	226.22	32.91	259.13
30	276.91	41.55	318.46
40	318.13	66.22	384.35
50	366.67	109.25	475.92

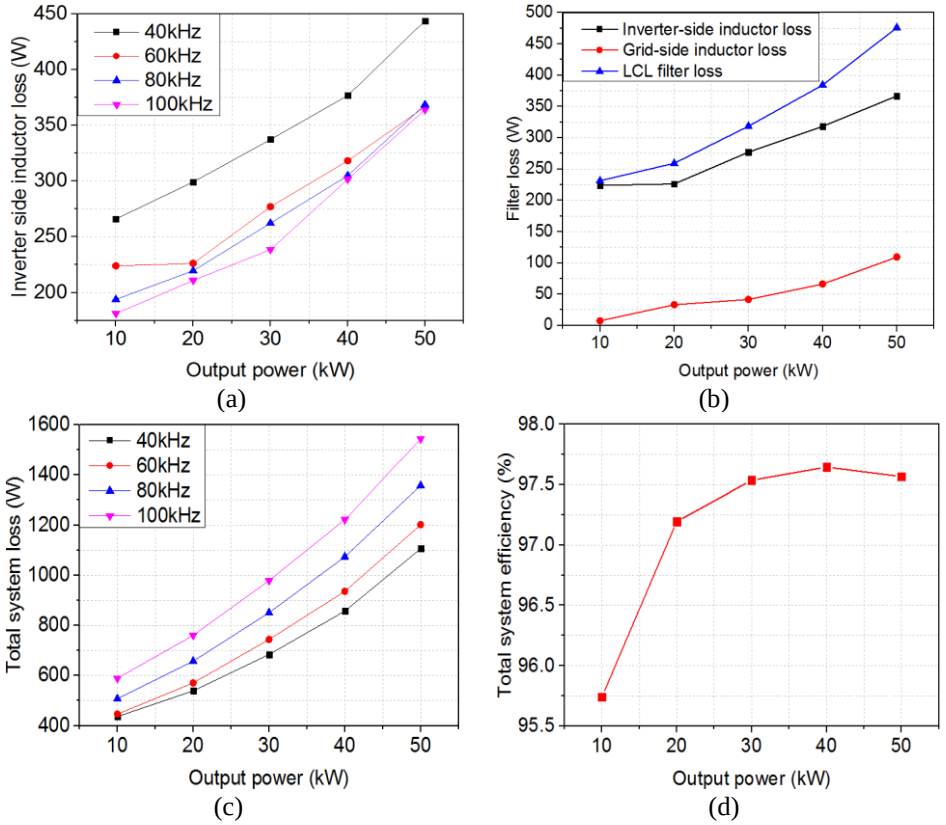

Figure 3. 18 (a) Inverter-side inductor loss versus output power for varying switching frequencies, (b) Contribution of inverter-side and grid-size inductors' losses versus output power at 60 kHz switching frequency, (c) Total system loss, and (d) Total system efficiency at 60 kHz.

For a 50 kW converter operating at full-load condition, the space and weight constrains for the cooling system on an aircraft leads to the necessity of a careful design study of the liquid coolant system. The heat sink with liquid cooling system has been verified in [18]. According to the measurement of power analyzer as shown in Figure 3.13, the calculated total loss of the inverter system

presented in Figure 3.18 (c) is about 1200 W, with the loss in LCL filter loss to be 475.92 W, the SiC power module loss will be 724.08 W, which is cooled by the cold plate presented in Figure 3.12 [18]. The inverter-side inductor also requires to be cooled to meet the thermal requirement.

Table 3. 10 Thermal properties for inductor liquid cooling system

Types	Amorphous	Coolant: Duralco 128	ABS
Density (kg/m3)	7180	980.6	1040
Specific heat (J/kg-K)	540	1000	1260
Thermal conductivity (w/m-K)	10	4.324	0.17

Table 3. 11 Thermal properties of liquid coolants

Types	Water	Fuel	Oil
Density (kg/m^3)	977.63	770	860
Specific heat (J/kg-K)	4190	2450	2080
Thermal conductivity (w/m-K)	0.67	0.105	0.139
Viscosity (kg/m-s)	4.04e-04	3.08e-04	0.053

3.6.4 Inductor cooling system design and water cooling verification at 25 ^oC

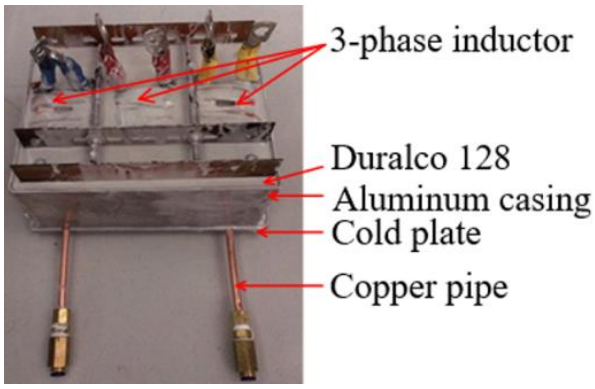

Figure 3. 19 Liquid cooled inverter-side inductor.

The liquid cooled inverter-side inductor is designed and fabricated, as shown in Figure 3.19. The inductor is encapsulated in an aluminum casing, which is filled with high thermal conductivity coolant Duralco 128 [26]. The heat sink is attached underneath the casing. The thermal image of the inverter-side inductor

operating at 50 kW output power with a flow rate of 2 liters per minute (LPM) and an operating temperature of 25^{o}C is presented in Figure 3.20. Figure 3.21 compares the simulated and measured maximum hot spot temperatures of the liquid cooled inductor operating at 50 kW output power with varying flow rate. The discrepancy is around 10 % and there are three possible reasons that may lead to this discrepancy. The first one is that in the simulation, the thermal interface is perfectly flat and smooth, but in the experiment, thermal greases are applied to fill possible air gaps between the casing bottom surface and the cold plate. The second one is that the thermal path across the duralco 128 between inductor core surface and the aluminum casing is not exactly the same, as it is impossible for actual inductor core to be perfectly identical to the simulated core because of fabrication tolerance. Lastly, the thermal conductivity of amorphous core along horizontal and vertical laminations is different; but a solid core is a solid piece in the simulation. Given the above mentioned reasons, the simulation model in Figure 3.9 gives reasonable results for preliminary design purposes. The inductor cooling system can be further improved by integrating cold plate and aluminum casing together, reducing the thermal path of the coolant between inductor core and the aluminum casing. Also, for the thermal image measurement, the aluminum cover is not present on the top side of aluminum casing. In reality, the cover will be present and it is expected to improve the efficiency of the heat dissipation.

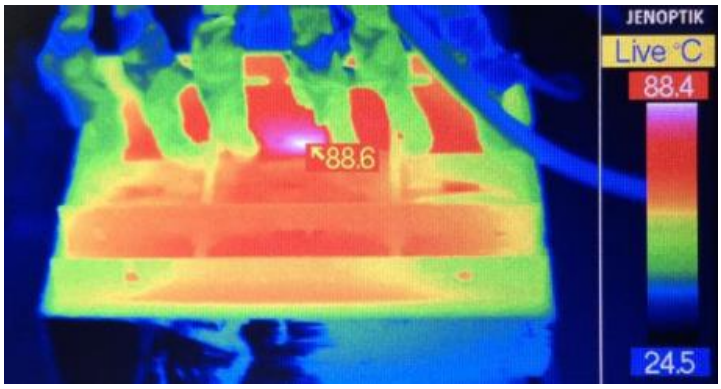

Figure 3. 20 The measured inverter-side inductor thermal image operating at 50 kW output power with a flow rate of 2 LPM and an operating temperature of 25 °C.

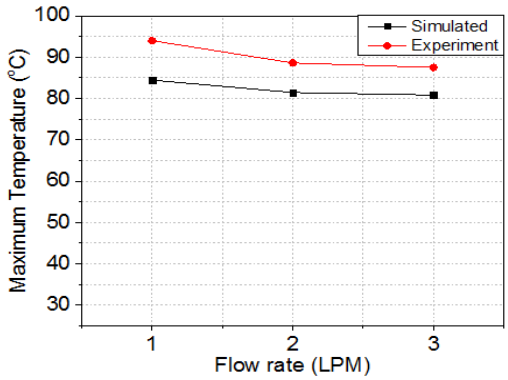

Figure 3. 21 Comparison between simulated and measured maximum temperature with varying flow rate and at 50 kW output power and 25 °C operating temperature.

3.6.5 Inductor cooling system study for aerospace applications

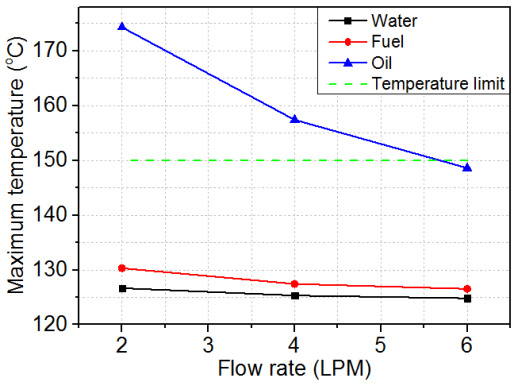

Figure 3. 22 Liquid flow rate against maximum temperature of inverter-side inductor with the three liquid coolants for 50 kW output power.

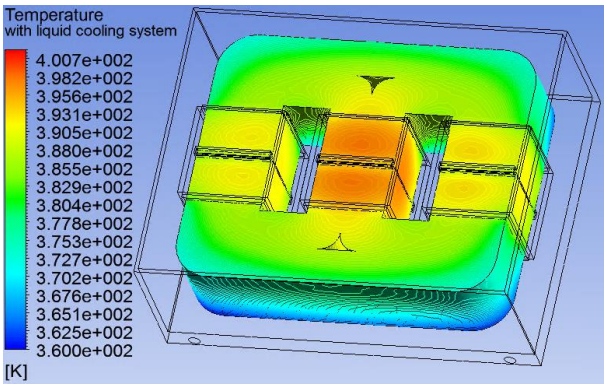

Figure 3. 23 Inductor temperature distribution of CFD simulation with the fuel liquid cooling system and 50 kW output power.

Liquid coolants such as fuel and oil are readily available in aircraft at 70 ^{o}C [25]. The inverter-side inductor cooling is further investigated by computational fluid dynamics (CFD). Table 3.10 gives the thermal properties of liquid cooling system and Table 3.11 presents the thermo-physical properties of water, fuel, and oil. Figure 3.22 presents the inverter-side inductor maximum temperature with CFD simulation for three liquid coolants with varying liquid flow rate. Water is not a feasible option of liquid coolant, as it requires an additional heat exchanger in the aircraft. The fuel requires lower pump power due to low viscosity, compared to oil. Figure 3.23 shows the inductor temperature distribution with fuel as the liquid coolant and a flow rate of 6 LPM, which has met the thermal requirement and with about 20 ^{o}C margin.

3.7 Summary

The detailed design flow of an LCL filter for a HPDC intended for aerospace applications has been presented. The design of the inductors, including core material selection, core structure, bobbin and wire is carefully studied and

analyzed. The customized amorphous core is proposed and the trade-off among air gap, inductor weight and thermal issue is evaluated systematically. Finally, the THD performance of LCL filter and the simulation model of liquid cooled version inductor is demonstrated on a 50-kW 60-kHz inverter system platform with experimental verification. Based on the CFD simulation of the inductor, meeting the thermal requirement at 50 kW full-load power is feasible for aerospace applications if a liquid cooling system is in place. The design methodology of the output filter with detailed electrical-magnetic-thermal-fluid analysis serves as a useful design reference for future HPDC systems.

Chapter 4 Magnetic Integration of Three-Phase LCL Filter with Delta-Yoke Composite Core

In this chapter, to reduce the weight and size of the LCL filter, the magnetic integration of the filter with delta-yoke composite core is explored and discussed.

4.1 Introduction

The use of PWM techniques in power conversion is a common technique to achieve good conversion efficiency but it results in significant level of harmonics [15, 75]. Therefore, a passive filter is needed at the grid side of the HPDC to ensure good power quality [15, 17, 87, 88] and LCL filters are commonly adopted for this purpose [46, 49, 89]. In an LCL filter, inductors usually account for nearly half the total weight of the entire HPDC and hence, their designs are crucial if weight is a major design consideration [12]. Conventionally, three-phase inductors are wound on rectangular composite core [90]. This chapter explores the use of alternative core structure to achieve weight reduction without compromising the symmetry of the three-phase magnetic circuits [32, 91-93].

Combining both magnetic and dielectric integrations to realize an integrated filter seems promising for excellent power density [92, 94] but poor heat dissipation limits this kind of integrated filter to lower power ($\leq$ 1 kW) converters [95]. For higher power (>1 kW) converters, magnetic integration of an integrated filter still remains a more feasible solution. By using a rectangular common yoke for two separate inductors, it is possible to reduce the weight of the magnetic core [31]. Also, using a bridging yoke to integrate the functionality of three coupled

inductors and a three-phase line inductor has also been found to be effective in total core volume reduction, as compared with separate inductors [96]. To summarize, Table 4.1 gives an overview of the pros and cons of comparing LC integration method and the magnetic integration method.

Table 4. 1 Comparison of LC integration method and the magnetic integration method [95]

Types	Advantages	Disadvantages	Power Rating
LC integration method with flexible multilayer foil [92]	Low cost and ease of fabrication	Poor stability and heat dissipation	$\leq$ 1kW
LC integration method with planar printed circuit [92, 94]	High degree of integration and stable structure	Poor heat dissipation	$\leq$ 1kW
Magnetic integration method for LCL filter [31]	Reduction of core volume, stable structure and good heat dissipation	Need to take into consideration of mutual coupling between inductors	> 1kW

Using the rectangular yoke magnetic core as a benchmark, the delta-yoke core is explored for the magnetic integration of inverter-side and grid-side inductors of an LCL filter with the objective of core volume reduction without affecting the filter's performance. Adopting a triangular-shaped core structure, the magnetic integration of inductors of an LCL filter for a three-phase grid-connected inverter [97] will be described with its performance evaluated. This chapter is organized as follows. Firstly, it presents briefly the design procedure of LCL filter and the magnetic circuit of a conventional three-phase inductors. Then the alternative core structure is proposed for the magnetic integration of the three-phase inductors. The three-phase inductors on the proposed core is simulated with finite element (FE) method to demonstrate its ability for weight reduction [98]. The mutual coupling between inductors is simulated and a

temperature measurement is conducted on the filter to demonstrate the new core structure does not affect the mutual coupling and thermal issue adversely. Finally, THD is measured to validate the proposed LCL filter's performance experimentally.

4.2 LCL filter design and three-phase inductor magnetic circuits

4.2.1 LCL filter design procedure

Figure 2.3 shows a three-phase LCL filter of a grid-connected inverter, where *A, B* and *C* denote the three phases, respectively. L_{in} and L_{grid} are inverter-side and grid-side inductors, respectively; and *C* is the capacitor. The LCL filter is designed to meet the relevant power quality requirements.

The purpose of the inverter-side inductor L_{in} is to suppress the switching frequency current ripple. For a three-phase three wire system, the inverter side inductance, depending on the maximum current ripple at the inverter output, is given by (3.2) [76].

From (3.2), the worst case maximum current ripple occurs at m = 0.5 and the inverter-side inductor is determined by:

$$L_{in} = \frac{2V_{DC}}{6\Delta I_{L\max} f_{sw}} \tag{4.1}$$

For the selection of capacitor value, larger capacitance provides good attenuation to high frequency ripple but also causes higher reactive power, which can affect the power factor of the inverter. As a rule of thumb, the reactive power

should be limited to about 5 % of total system power rating P_{rating}. With known line-to-line RMS voltage $V_{ll,rms}$, the base impedance Z_{base} is determined by (3.3).

Once the base impedance is known, the base capacitance C_{base} and the base inductance L_{base} can be determined from (3.4) and (3.6), respectively.

Given the 5% reactive power constraint, the value of the capacitor can be obtained by:

$$C \approx 0.05 \times C_{base} \tag{4.2}$$

For the grid-side inductor, its main objective is to ensure the current harmonics complied with the relevant standard. The maximum value of the total inductance should be around 10 % of base inductance to limit the ac voltage drop and the grid-side inductance is determined by[17, 88]:

$$L_{grid} \approx 0.1 \times L_{base} - L_{in} \tag{4.3}$$

4.2.2 Magnetic circuit analysis of E-shaped core

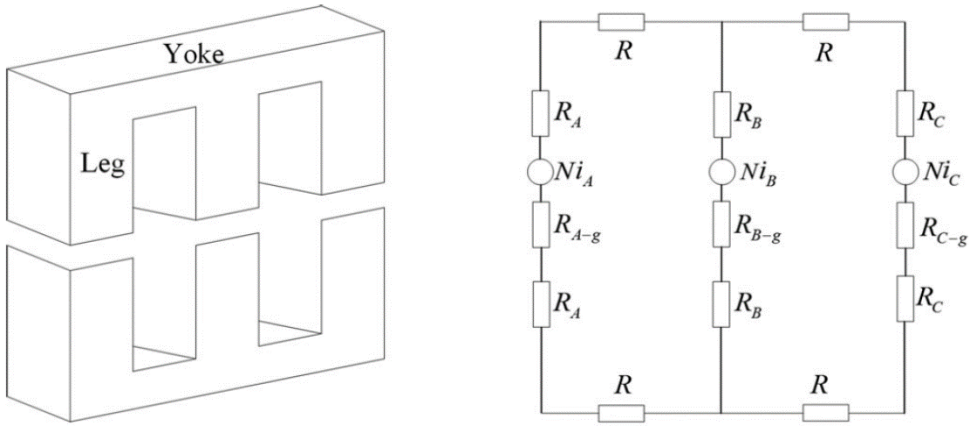

(a) (b)

Figure 4. 1 Three-phase inductor: (a) E-shaped cores (b) Magnetic circuits.

Conventionally, composite E-shaped cores are adopted to provide the magnetic path of each inductor in the LCL filter, as illustrated in Figure 4.1 (a).

The three legs have the same cross-sectional area with each leg wound with N turns of conductor. To prevent saturation in the magnetic core, a small air gap between two E-shaped cores is maintained. The fringing flux is usually negligible due to very small air gap. Therefore, the magnetic flux ϕ in each leg is given by:

$$\phi = B_c A_c = B_g A_g \tag{4.4}$$

where the subscripts c and g denote core and air gap, respectively.

Since the cross-sectional area of the core and the air gap are the same ($A_c = A_g$), $B_c = B_g$. Then the magneto-motive force (MMF) F can be determined as [45]:

$$F = Ni = H_c l_c + H_g l_g = \frac{B_c l_c}{\mu_0 \mu_r}\left(1 + \frac{\mu_r}{l_c / l_g}\right) \tag{4.5}$$

where i is the current in the winding, H is magnetic field intensity, l is the length of the magnetic flux path, μ_0 and μ_r are permeability of vacuum and relative permeability of the core material, respectively.

The magnetic circuit of the E-shaped core structure of Figure 4.1 (a) is shown in Figure 4.2 (b).

The inductance of each leg can be obtained by:

$$L = \frac{\lambda}{i} = \frac{N\phi}{i} = \frac{NBA_c}{i} = N^2 A_c \frac{\mu_0 \mu_r}{l_c} \frac{1}{\left(1 + u_r / \left(l_c / l_g\right)\right)} \tag{4.6}$$

The length of magnetic path of the center leg is slightly shorter than those of the two side legs. Hence, the inductance of phase B is expected to be slightly larger than those of the other two phases. According to (4.6), inductances of phases A and C are identical.

If $\mu_r >> l_c/l_g$, the inductance depends mainly on the air gap and (4.6) can be further simplified to:

$$L = N^2 A_c \frac{\mu_0}{l_g} \tag{4.7}$$

4.2.3 Magnetic circuit analysis of triangular shaped core

To reduce the weight of inductor, the triangular shaped core as shown in Fig. 3 is explored. Comparing to E-shaped core, the proposed core has the same dimensions of legs and space between legs. The only difference is the shape of the yoke. The reluctance can be expressed as:

$$R = \frac{l}{\mu_0 \mu_r A} \tag{4.8}$$

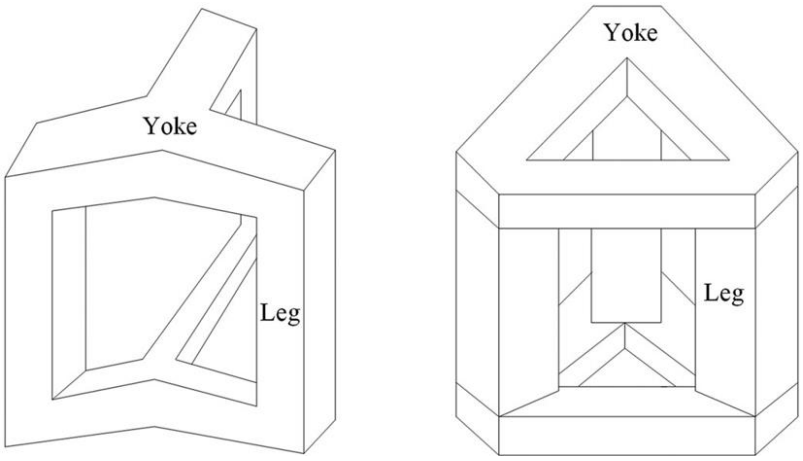

(a) (b)

Figure 4. 2 Triangular shaped core: (a) Y-yoke (b) Δ-yoke.

Using the Y-Δ transformation, the reluctance of Δ-yoke will be larger than that of Y-yoke. Therefore, with the same l and according to (4.4), cross sectional area A of Δ-yoke will be smaller, i.e., the Δ-yoke core requires less material as compared to Y-yoke.

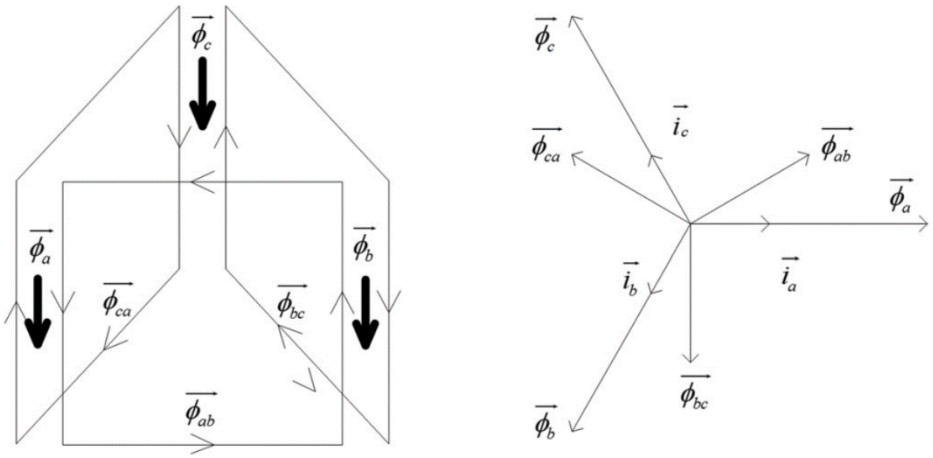

(a) (b)

Figure 4. 3 Magnetic fluxes in Δ-yoke composite core: (a) Magnetic flux distribution (b) Vector diagram of flux.

Figure 4.3 shows the magnetic flux distribution and the vector diagram of the magnetic flux of the Δ-yoke core, where ϕ_{ab}, ϕ_{bc}, and ϕ_{ca} can be regarded as three independent magnetic flux loops with a 60° phase difference between any two of them. Figure 4.4 shows the magnetic circuit of the proposed Δ-yoke core of a three-phase inductor. Each phase of the magnetic circuit consists of two independent magnetic fluxes governed by the following relationships:

$$\vec{\phi}_a = \vec{\phi}_{ab} - \vec{\phi}_{ca}$$

$$\vec{\phi}_b = \vec{\phi}_{bc} - \vec{\phi}_{ab}$$

$$\vec{\phi}_c = \vec{\phi}_{ca} - \vec{\phi}_{bc} \tag{4.9}$$

According to the vector diagram, the mathematical relationship is given by:

$$\phi_a^2 = \phi_{ab}^2 + \phi_{ca}^2 - 2 \times \phi_{ab} \times \phi_{ca} \cos(2\pi/3) \tag{4.10}$$

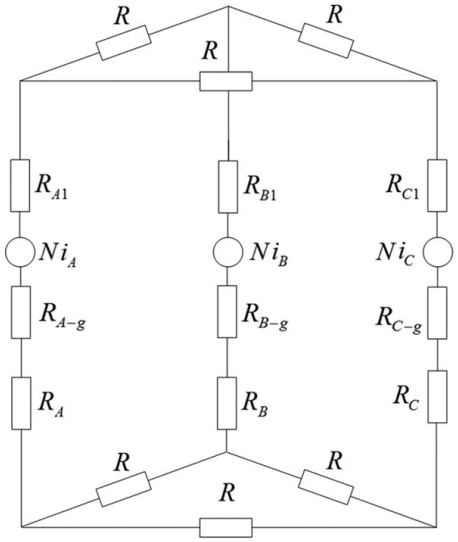

Figure 4. 4 Magnetic circiut of a three-phase inductor on the proposed core.

The relationship between magnetic fluxes in the leg and the yoke is:

$$\phi_a = \phi_b = \phi_c = \sqrt{3}\phi_{ab} = \sqrt{3}\phi_{ca} = \sqrt{3}\phi_{bc} \tag{4.11}$$

Combining (4.4) and (4.11), and by keeping the same magnetic flux density, it leads to:

$$A_{leg} = \sqrt{3}A_{yoke} \tag{4.12}$$

From (4.12), it indicates that for the same inductance, Δ-yoke core requires less material than that of the E-shaped core, and hence, less weight.

4.2.4 Magnetic integration of LCL filter

The Δ-yoke core will be used for magnetic integration of an LCL filter with L_{in} and L_{grid} wound on the two legs and shared the common yoke, as illustrated in Figure 4.5. The magnetic flux in the common core ϕ_{co-ab}, ϕ_{co-bc}, and ϕ_{co-ca}, and, can be derived from:

$$\overrightarrow{\phi_{co-ab}} = \overrightarrow{\phi_{1ab}} - \overrightarrow{\phi_{2ab}}$$

$$\overrightarrow{\phi_{co-bc}} = \overrightarrow{\phi_{1cb}} - \overrightarrow{\phi_{2bc}}$$

$$\overrightarrow{\phi_{co-ca}} = \overrightarrow{\phi_{1ca}} - \overrightarrow{\phi_{2ca}} \quad (4.13)$$

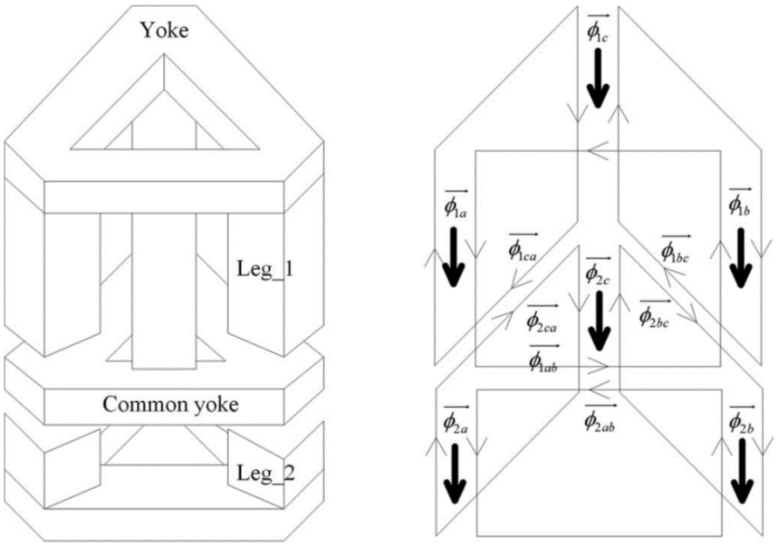

(a) (b)

Figure 4. 5 Proposed Δ-yoke core structure of two integrated three-phase inductors. (a) Core structure (b) Magnetic flux.

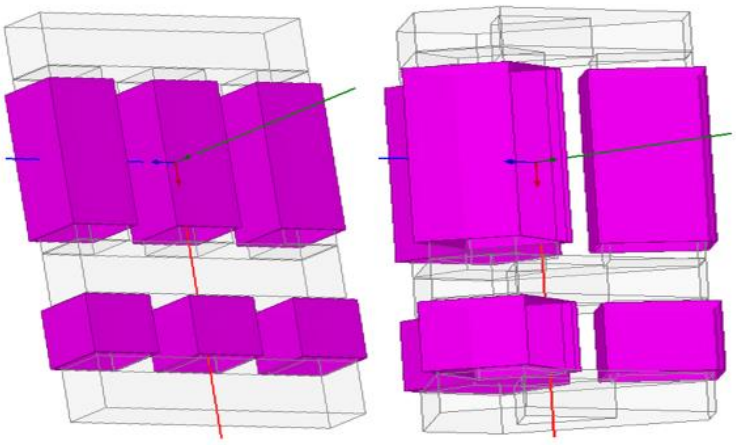

(a) (b)

Figure 4. 6 3D model of the magnetic integration of two three-phase inductors: (a) E-shaped composite core (b) Δ-yoke composite core.

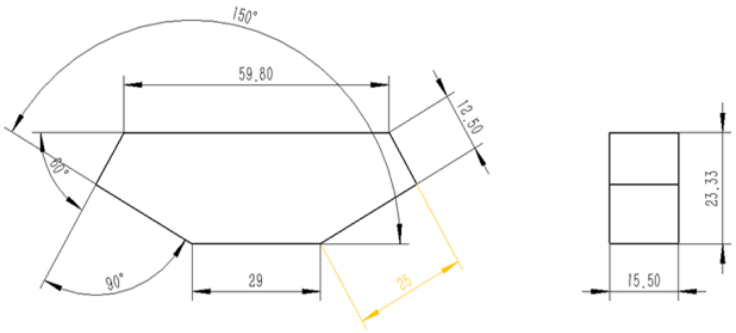

Figure 4. 7 Δ-yoke dimensions.

As the coupling between inverter-side and grid-side inductors on the same magnetic core affects the performance of LCL filter [31], some design attention is necessary to reduce the coupling. According to (4.6), (4.11), and (4.13), the flux in the common core of the two three-phase integrated inductors is:

$$\phi_{co-ab} = \phi_{1ab} - \phi_{2ab} = \frac{1}{\sqrt{3}}\left(\frac{L_{A-in}\, i_{1a}}{N_{A-in}} - \frac{L_{A-grid}\, i_{2a}}{N_{A-grid}}\right) \tag{4.14}$$

From (4.14), the coupling can be reduced by adjusting the ratios of $L_{A\text{-}in}/N_{A\text{-}in}$ and $L_{A\text{-}grid}/N_{A\text{-}grid}$, or increasing the thickness of common yoke.

4.3 Simulations results

4.3.1 Finite - element simulation

From Ampere's law, it is known that magnetic field intensity $\vec{H}$ can be solved from current density $\vec{J}$ through a curl operation:

$$\vec{\nabla} \times \vec{H} = \vec{J} \tag{4.15}$$

The relationship between magnetic field intensity $\vec{H}$ and current density $\vec{J}$ are governed by (4.16) and (4.17). The vector $\vec{A}$ can be derived from current

density $\vec{J}$ in (4.15). Then magnetic flux density $\vec{B}$ and magnetic field intensity $\vec{H}$ can be obtained from (4.17) and (4.18). Equations (4.15) - (4.18) are to be solved by ANSYS Maxwell, an FE based solver.

$$\vec{A} = \frac{u_0}{4\Pi}\int \frac{\vec{J}}{r} dV \tag{4.16}$$

$$\vec{B} = \vec{\nabla} \times \vec{A} \tag{4.17}$$

$$\vec{H} = \frac{1}{u}\vec{B} \tag{4.18}$$

4.3.2 Inductance calculation

From the FE simulation, the N-turn foil windings can be represented by one-turn coil windings that carried the current. Figure 4.6 shows the 3D model of the two integrated inductors on the composite core. To simplify the FE model, the current flowing through the copper foil is assumed uniformly distributed. With the core material operating in the linear region, the flux linkage can be obtained and the inductance can be calculated as:

$$L = \frac{\phi}{I} \tag{4.19}$$

4.3.3 Three-phase inductor design

The B23R085 silicon steel is chosen as the composite core for the simulation study and its dimensions are given in Table 4.2. For comparison purpose, two different designs are modelled and simulated.

i. One three-phase inductor on E-shaped composite core. It is named as Core #1, which is constructed with three leg #1 and two rectangular yokes, as shown in Figure 4.8 (a); and

ii. One three-phase inductor on Δ-yoke composite core. It is named as Core #2, which is constructed with three leg #1 and two Δ-yokes, as shown in Figure 4.8 (b).

The dimensions of the core components (leg and yoke) for cores #1 and #2 are given in Table 4.2. The simulation conditions for cores #1 and #2 are given in Table 4.3. The inductances computed from the simulation with 10 A RMS current are tabulated in Table 4.4.

In Table 4.4, it shows that the inductances between cores #1 and #2 are rather close. However, comparing to core #2, the inductances of the three phases of core #1 have larger variation because of asymmetrical magnetic circuit. The simulated magnetic flux distributions for cores #1 and #2 are also displayed in in Figure 4.8 (a) and (b), respectively. The maximum flux densities for core #1 and core #2 are 1.31 and 1.16 T, respectively; an indication that core #2 is less prone to core saturation, and therefore, smaller core loss. In summary, the simulation results show that three-phase inductor implemented with Δ-yoke composite core has more merits.

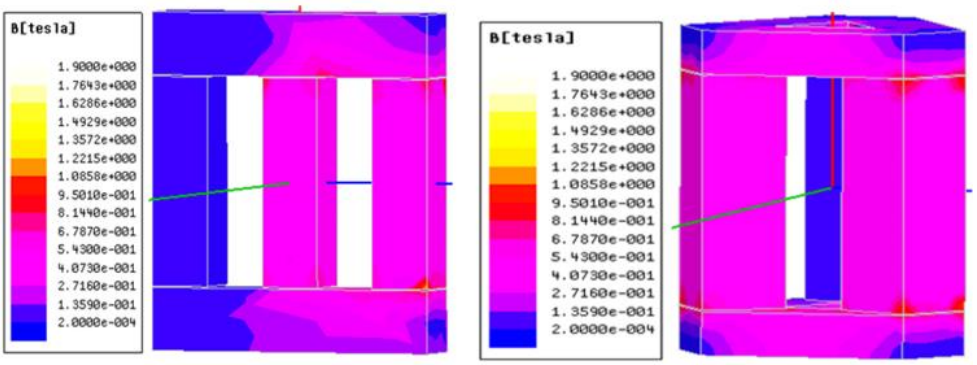

(a) (b)

Figure 4. 8 FE analysis for magnetic flux distribution in the core of inverter-side inductor. (a) Core #1: E-shaped composite core (b) Core #2: Δ-yoke composite core.

Table 4. 2 Core component dimensions (B23R085 silicon steel core)

Core component	Dimensions (mm)
Leg #1	25 × 25 × 83
Leg #2	25 × 25 × 30
Rectangular yoke	25 × 25 × 125
Δ-yoke	Refer to Fig.4.7

Table 4. 3 Simulation conditions

Conditions	Core #1	Core #2	Core #3	Core #4
Turns/ phase	21	21	Inv: 21; Grid: 10	Inv: 21; Grid: 10
Air gap (mm)	1	1	Inv: 1; Grid: 0.5	Inv: 1; Grid: 0.5

Table 4. 4 Simulated inductances of four different cores

Core types		Inductance value(μH)			B_{max} (T)
		Phase A	Phase B	Phase C	
Core #1		342.38	325.23	333.12	1.31
Core #2		332.82	328.48	332.6	1.16
Core #3	L_1	343.19	335.85	339.24	1.94
	L_2	130.84	132.07	130.91	
Core #4	L_1	324.56	323.63	322.48	1.48
	L_2	133.34	132.65	132.43	

4.3.4 Mutual coupling coefficient between two integrated inductors of LCL filter

Considering the merits of Δ-yoke core based there-phase inductor, it is extended to integrate two three-phase inductors for an LCL filter. According to (4.14), the mutual coupling coefficient between inverter-side and grid-side inductors can be reduced by increasing the common yoke thickness. Based on simulations, Figure 4.9 shows the mutual coupling coefficient as a function of the common yoke thickness. According to the intersection frequency [31], when the mutual coupling coefficient is chosen to around 0.015, the intersection frequency are up to 66 kHz and higher than the switching frequency 60 kHz where the dominant switching harmonics lie in, which means effective attenuation of switching harmonics. Based on the recommended mutual coupling

coefficient, the thickness of common yoke for Δ-yoke composite core is found to be 15.5 mm from Figure 4.9. The corresponding thickness for E-shaped composite core is around 25 mm. The mutual coupling coefficient between inverter-side and grid-side inductors for the three phases are tabulated in Tables 4.5 and 4.6 for E-shaped composite core and Δ-yoke composite core, respectively. These two tables show that the Δ-yoke composite core design has relative uniform common flux distribution in the common yoke, comparing to E-shaped composite core.

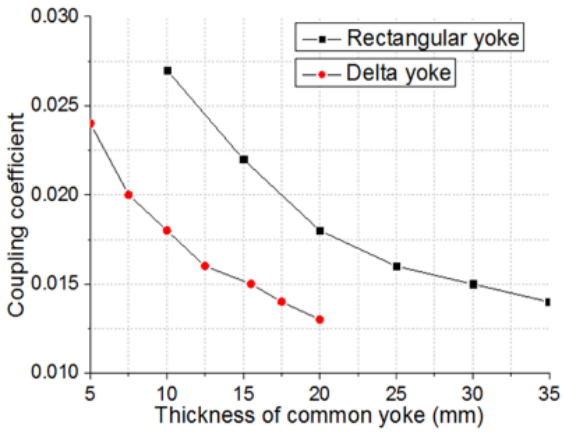

Figure 4. 9 The simulation results of inductive coupling coefficient and thickness of common core.

Table 4. 5 Mutual coupling coefficient between integrated inductors with E-shaped composite core

Inductors	A-inv	B-inv	C-inv
A-grid	0.016	0.011	0.007
B-grid	0.013	0.016	0.013
C-grid	0.008	0.011	0.016

Table 4. 6 Mutual coupling coefficient between integrated inductors with Δ-yoke composite core

Inductors	A-inv	B-inv	C-inv
A-grid	0.015	0.01	0.01
B-grid	0.01	0.015	0.01
C-grid	0.01	0.01	0.015

4.3.5 Magnetic integration of LCL filter

Again for comparison, magnetic integration the LCL filter using the following two types of core structures are modelled and simulated:

i. Two three-phase inductors on E-shaped composite core. It is named as Core #3, which is constructed with three leg #1, three leg #2 and three rectangular yokes, as illustrated in Figure 4.10 (a); and

ii. Two three-phase inductors on Δ-yoke composite core. It is named as Core #4, which is constructed with three leg #1, three leg #2 and three Δ-yokes, as shown in in Figure 4.10 (b).

The dimensions of the core components for cores #3 and #4 are also given in Table 4.2. The simulation conditions for cores #3 and #4 are also given in Table 4.3. The simulated inverter-side inductance L_1 and grid-side inductance L_2 with 10 A RMS current are also tabulated in Table 4.4. The simulated results in Table IV shows that inductances between cores #3 and #4 have little difference (< 6%). Due to asymmetry of the magnetic circuit of core #3, the individual inductances of each phase of core #3 have larger variation as compared to core #4. Similar to the earlier results of one three-phase inductor, the maximum flux density of 1.48 T in core #4 as shown in Figure 4.10 (b), is less than that of core #3 (1.94 T), as presented in Figure 4.10 (a). For practical design, the maximum operating magnetic flux density is limited to around 80 % of the saturation flux density for the chosen core (1.9 T for B23R085 core), to prevent core saturation as well as to reduce core loss. Based on the simulation results, core #3 is near

saturation. Therefore, the Δ-yoke composite core is less prone to core saturation because of lower maximum flux density for the same inductances.

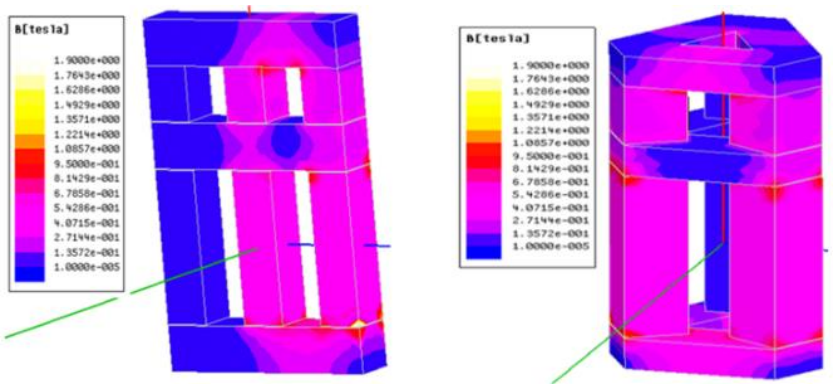

(a) (b)

Figure 4. 10 FE analysis of magnetic flux distributions in the core of inverter-side and grid-side inductors. (a) Core #3: E-shaped composite core (b) Core #4: Δ-yoke composite core.

4.4 Weight reduction

The total core material volumes of cores #1, #2, #3 and #4 are computed and tabulated in Table 4.7.

Table 4. 7 Core material volumes (mm^3)

Core Type	Leg Volume	Yoke Volume	Total
Core #1	155,625	156,250	311,875
Core #2	155,625	125,377	281,002
Core #3	211,875	234,375	446,250
Core #4	211,875	188,066	399,941

By comparing the total core material volumes for one three-phase inductor design using cores #1 and #2, the reduction in material volume is 9.9 %. For two three-phase inductors implementation of an LCL filter using cores #3 and #4, the reduction in material volume is 10.4%.

4.5 Experimental results analysis

Both the E-shaped core and the Δ-yoke core are designed and fabricated for experimental validation. Figure 4.11 shows the two three-phase inductors integrated on the same core to realize the LCL filter. For both cores, the B23R085 silicon steel is chosen as the core material. The LCL filter is finally integrated with a two-level three-phase inverter. The inverter specifications are given in Table 4.8.

Table 4. 8 Specifications of two-level three-phase inverter

Parameters	Core #3	Core #4
Inverter-side inductor	330 µH	320 µH
Grid-side inductor	130 µH	130 µH
Filter capacitor	2 µF	2 µF
Power	3.1 kW	
Input voltage	350 V	
Grid voltage	105 V	
Switching frequency	60 kHz	
Power frequency	400 Hz	

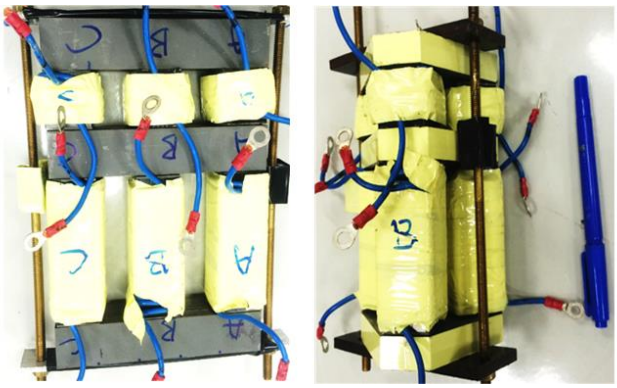

(a) (b)

Figure 4. 11 Three-phase inductors prototypes of the LCL filter with E-shaped core (a) and Δ-yoke core (b).

4.5.1 Temperature measurement for hot spots investigation

The thermal images of the two LCL filters with the two different types of cores are captured using the JENOPTIK thermography camera and presented in

Figure 4.12. Both integrated inductors are tested around half of an hour when the hot spot temperature was nearly stabilized. For the E-shape core, the hot spot occurs at the joint between the center leg and the middle yoke of inverter-side inductor, as this joint has higher magnetic flux density, comparing to other parts of the core, and the inverter-side has higher harmonics, comparing to grid-side. For the Δ-yoke core, the hot spot occurs at the joint between the legs and the yoke of inverter-side inductor, as the magnetic flux is relatively uniform, comparing to E-shaped core.

Overall, the highest temperature is almost the same for the two integrated inductors in Figure 4.12. The E – shaped integrated inductors have hot spots in the centre leg of inverter-side inductor, comparing to the other two side legs, while the legs of the Δ-yoke integrated inductors have the same thermal imaging of inverter-side legs.

(a) (b)

Figure 4. 12 Thermal imaging pictures of the integrated inductors with E-shaped core (a) and Δ-yoke core (b).

4.5.2 Measured current waveforms and total harmonic distortion (THD)

Figure 4.13 and Figure 4.14 show the inverter-side and grid-side current waveforms for both core structures, respectively.

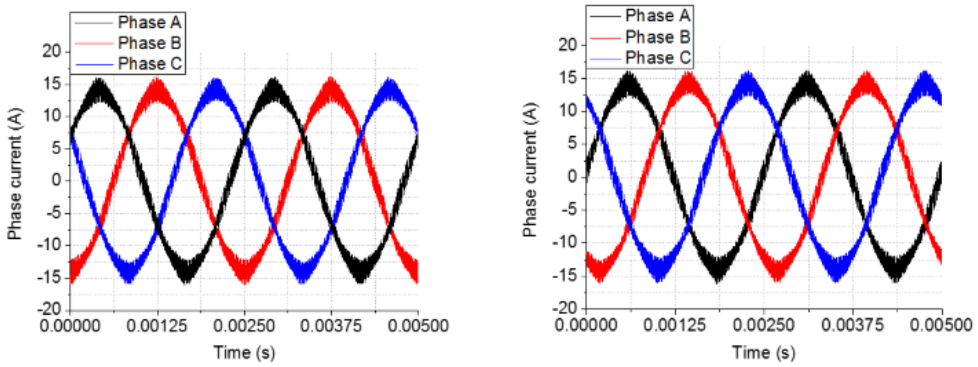

(a) (b)

Figure 4. 13 Measurements of inverter side current waveforms of the LCL filter with E-shaped core (a) and Δ-yoke core (b).

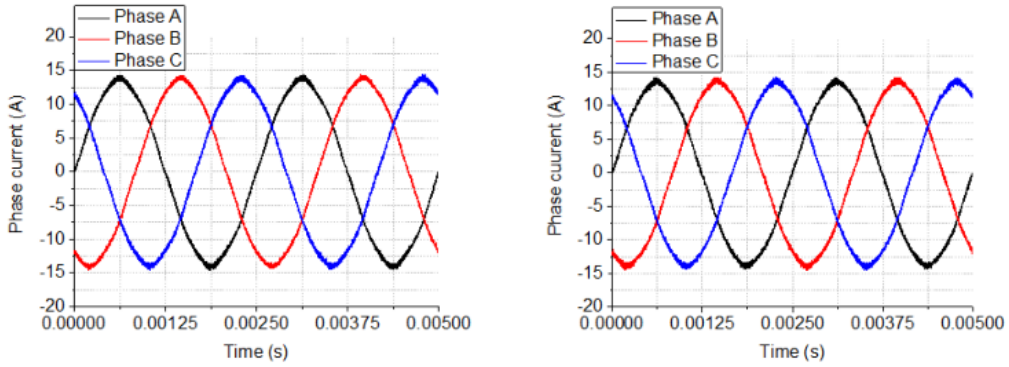

(a) (b)

Figure 4. 14 Measurements of grid side current waveforms of the LCL filter with E-shaped core (a) and Δ-yoke core (b).

Figure 4.15 shows that the THD reduces to 2.27 % and 2.20 % with E-shaped composite core and Δ-yoke composite core, respectively. In most power quality standards for aerospace applications, such as RTCA DO-160, EUROCAE ED-14F, ISO 1540-2006, Boeing D6-44588 and Airbus ABD-0100, the THD limit is < 3% [10].

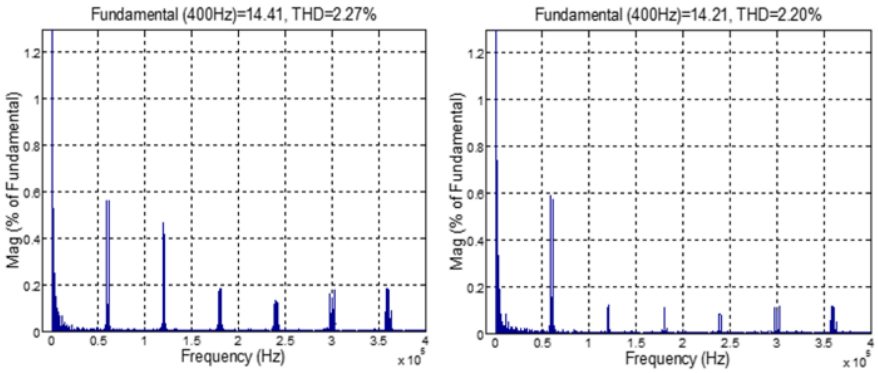

(a) (b)

Figure 4. 15 Grid-side current spectrum. (a) E-shaped composite core. (b) Δ-yoke composite core.

4.5.3 Lower order harmonics (≤ 40th order)

From Figure 4.15, besides the higher order harmonics of the switching frequency (60 kHz), lower order harmonics of the power frequency (400 Hz) are also exist. The limits of first 40th lower order harmonics for balanced three-phase electrical equipment in standard RTCA DO-160 [11], which is extracted and given in Table 2.1. The measured harmonics comparing against the limits are shown in Figure 4.16 and all of them are well below the limits. Hence, the designed LCL filter using both type of cores has met the power quality requirements.

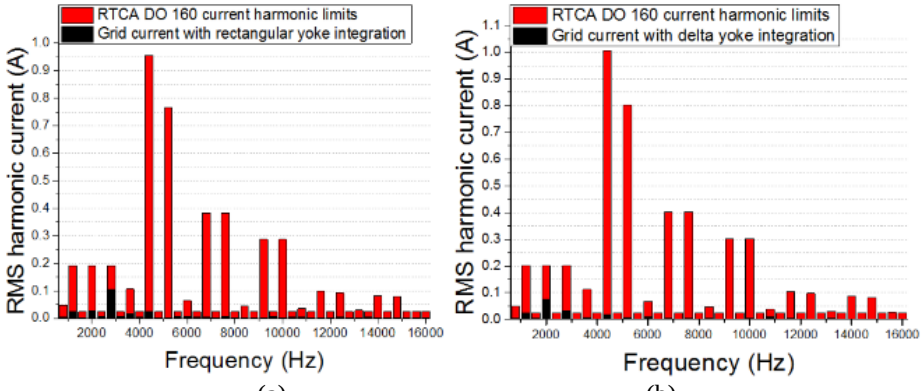

(a) (b)

Figure 4. 16 Grid-side harmonic current spectrum up to 40th order. (a) E-shaped composite core. (b) Δ-yoke composite core.

4.6 Summary

The magnetic integration of an LCL filter with Δ-yoke composite core for a three-phase inverter is proposed, designed and tested. The proposed core structure can achieve close to 10% weight reduction as compared to the conventional E-shaped core structure. Besides the weight reduction advantage, the Δ-yoke composite core design exhibit more balanced inductance in each phase and is less prone to core saturation. Not only the power quality requirement is met, the proposed core structure does not compromise in terms of mutual inductive coupling between integrated inductors as well as heat dissipation.

Chapter 5 Impact of Converter Configurations on Harmonic Filter Weight Reduction

Chapters 3 and 4 discussed the LCL filter design flow and magnetic integration of LCL filter to improve the power density of two-level three-phase inverter respectively. To increase the power rating, the parallel interleaved converters will be necessary. Hence, the coupled inductors to suppress the circulating current and the output harmonic filter to ensure the current still meets the THD standard requires optimization of the total harmonic filters' weight. On the other hand, different levels of converter also have great impacts on filter size and weight, so the harmonics and CM voltage with different converter configurations will be discussed and analyzed in this chapter.

5.1 Analysis and design of coupled inductor and output harmonic filter for interleaved three-phase VSCs

5.1.1 Introduction

Parallel interleaving three-phase PWM voltage source converters (VSCs) is commonly used in medium- and high power- converter systems. By shifting the carrier wave of individual converters with an appropriate angle for the same reference wave, the output voltage harmonics and EMI can be reduced, which results in smaller output harmonic and EMI filters [99, 100]. However, coupled inductors (CIs) are needed to suppress the circulating current between the two converters, which comes from the voltage difference of the parallel interleaving

VSCs[101]. In general, the total weight of inductor and capacitor can be reduced by adopting parallel interleaved VSCs.

There are numerous literatures studying the CIs in parallel interleaved VSCs [96, 102, 103], including design, integration, and controller, but there are very few study focused on design and optimization of coupled inductor and harmonic output filter. Figure 5.1 presents parallel interleaved three-phase voltage source converters with coupled inductors and output harmonic filter for grid application. For the first section of this chapter, the AC side harmonic current analysis and coupled inductance calculation will be discussed first. Then electrical circuits and electromagnetic simulation are presented. Finally, the total weight of coupled inductor and output filter with and without parallel interleaving will be compared.

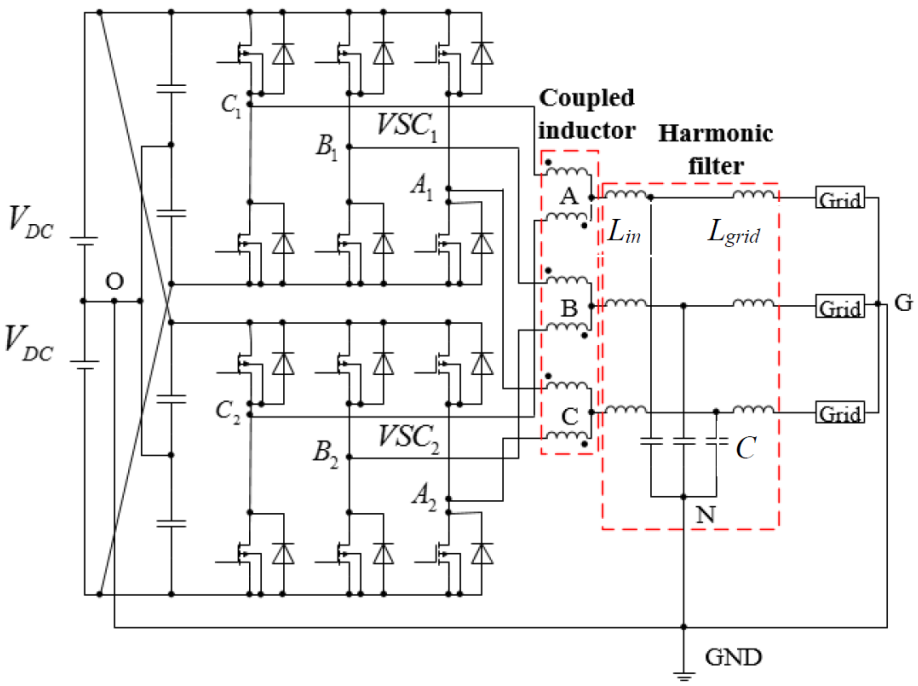

Figure 5. 1 Parallel interleaved three phase voltage source converters with coupled inductors and output harmonic filter for grid application

5.1.2 AC side harmonic current analysis, coupled inductance calculation, and output filter design

The individual converter output harmonics can be analysed in the frequency domain, applying the double integral Fourier analysis approach, the harmonic component between the ac terminal and dc-link midpoint, phase-leg voltage V_{A1O} in Figure 5.1, corresponding to frequency $m\omega_c + n\omega_0$ can be expressed as[75]

$$V_{A1N}(m,n)(t) = C_{mn}\cos[(m\omega_c + n\omega_0)t + \theta\omega_c + \theta\omega_0 + \theta_{mn}] \tag{5.1}$$

where C_{mn} is the harmonic amplitude, ω_c is the carrier angular frequency, m is the carrier integer indices, ω_0 is the fundamental line angular frequency, n is the baseband integer index, θ_c is the initial carrier angle, θ_0 is the initial reference angle, and θ_{mn} is a constant value, depending on the PWM scheme and operation condition. From (5.1), the phase-leg voltage is composed of DC offset (m=n=0), fundamental and baseband harmonics (m=0), carrier harmonics (n=0), and sideband harmonics ($n\neq0$). C_{mn} is only a function of modulation index M and PWM scheme, and based on the double integral Fourier analysis method, C_{mn} and θ_{mn} can be obtained as follows:

$$C_{mn}e^{j\theta_{mn}} = A_{mn} + jB_{mn} = \frac{V_{dc}}{\pi}\int_{-\pi}^{\pi}\int_{x_r}^{x_f} e^{j(mx+ny)}dxdy \tag{5.2}$$

Without interleaving, the amplitude of the average voltage for V_{A1O} and V_{A2O} is given by:

$$C_{mn\_avg} = 0.5(C_{mn1} + C_{mn2}) = C_{mn} \tag{5.3}$$

When the two converters in parallel interleaved with the phase shift κ for carrier waves, resulting in the $m\kappa$ angle shift between the voltages V_{A1O} and V_{A2O}, the average voltage with interleaving can be obtained by:

$$C_{mn\_avg}^{'} = 0.5\left|C_{mn1} + C_{mn2}e^{jm\kappa}\right| = C_{mn}\cos\left(m\kappa/2\right) \tag{5.4}$$

From (5.4), a specific κ is used, and different order switching frequency harmonics can be eliminated. For instance, all odd-order switching harmonics are eliminated from the output voltage with the phase-shifting of π, and in other words, these odd-order switching harmonics are flowing between two converters as presented in (5.5). Since a voltage difference between two converters are produced with interleaving, the harmonic voltage between the two converters is given by:

$$C_{mn\_diff}^{'} = C_{mn}\sin\left(m\kappa/2\right) \tag{5.5}$$

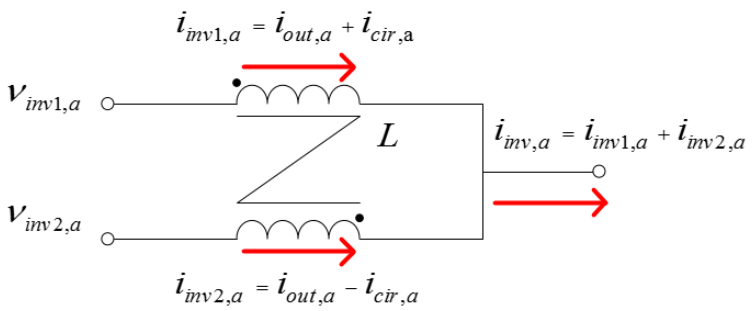

Figure 5. 2 Phase current analysis of two parallel interleaved three-phase VSIs

With interleaving, the phase current of the individual converter can be sub-divided into two parts, output current i_{out} and circulating current i_{cir}, as presented in Figure 5.2. The relationship of phase current, output current, and circulating current are given as follows:

$$I_{a1} = I_{out} + I_{cir} \tag{5.6}$$

$$I_{a2} = I_{out} - I_{cir} \tag{5.7}$$

$$I_{cir} = \frac{I_{a1} - I_{a2}}{2} \tag{5.8}$$

$$I_{out} = \frac{I_{a1} + I_{a2}}{2} \tag{5.9}$$

The circulating current equivalent circuit is shown in Figure 5.3. The coupled inductor is used to suppress the switching frequency circulating current. The relationship between the circulating current and the voltage difference in parallel interleaved VSCs is given by:

$$2(L_s + M)\frac{dI_{cir}}{dt} = V_{cir} \tag{5.10}$$

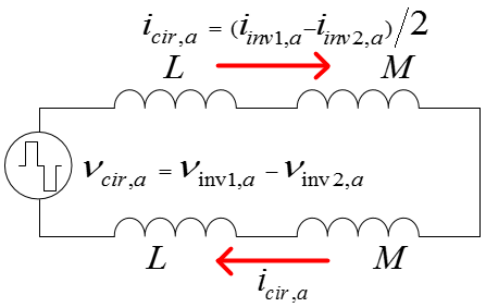

Figure 5. 3 Equivalent circuit for circulating current

For coupled inductors, the self-inductance L and the mutual-inductance are almost the same ($L \approx M$), since the magnetic fluxes in the core originating from the output current are opposite in direction and cancelled each other out, and the main flux originates from the circulating current. The peak-to-peak circulating current is determined by V_{dc}, coupled inductance and the switching frequency. The maximum peak to peak circulating current is when the time duration dt is half of the switching period [103], expressed as follows:

$$I_{cir,p\text{-}p,\max} \approx \frac{V_{dc}}{8L f_{sw}} \tag{5.11}$$

Through (5.11), the coupled inductance can be obtained.

Also, the product of the circulating current and the coupled inductance is a constant value, as formulated in (5.12).

$$8LI_{cir,p\text{-}p,\max} = \frac{V_{dc}}{f_{sw}} = Constant \tag{5.12}$$

$$L_0 = \frac{N_0^2}{R} = \frac{u_0 u_{rc} N_0^2 A_c}{l_c} \tag{5.13}$$

Based on (5.13), there are three methods to reduce the coupled inductance L_0 to L.

1) Decrease the cross-section area A_C, as I_{cir} increases, the core is prone to saturation;

2) Increase magnetic path length l_C, so that core volume increases; and

3) Decrease number of turns N, since $L*I$ is constant, then based on (5.14), the core is also prone to saturation;

$$B_{pk,0} = \frac{u_0 u_{rc} N_0 I_{L\max,0}}{l_c} < B_{pk} = \frac{u_0 u_{rc} N_0 I_{L\max,0}}{l_c} \times \frac{N_0}{N} \tag{5.14}$$

Therefore, the size of coupled inductor depends on voltage-seconds given in (5.12), and the coupled inductance can be made as large as possible, given a certain weight constraint.

Considering the grid-side inductance and the lower THD with interleaving, the topology of the output filter uses LC filter. In three-phase four-wire system

without interleaving, the maximum current ripple (M=0.5) at the inverter output is given by [30, 76]:

$$\Delta I_{L\max} = \frac{V_{DC}}{2L_{in\_maximum} f_{sw}} \tag{5.15}$$

where M is the SPWM modulation index. With interleaving for 180^0 phase-shifting carrier wave, the main switching frequency harmonic is in the range of 2fsw, and the rated current is also double with the same output voltage and twice the power. Hence, with 20% peak-to-peak current ripple, the inverter-side inductance can be estimated by

$$L_{in} \leq L_{in\_maximum} = \frac{V_{DC}}{8\Delta I_{L\max} f_{sw}} \tag{5.16}$$

Larger capacitor provides good filtering of high frequency ripple, but it also introduces reactive power, that changes the power factor, and increases the leakage current. Normally this reactive power is kept within 5% of total system power rating P_{rating}. The base impedance Z_{base} can be determined with line-to-line RMS voltage $V_{ll,rms}$ as follows:

$$Z_{base} = \frac{V_{ll,rms}^2}{P_{rating}} \tag{5.17}$$

The base capacitance C_{base} will be given by:

$$C_{base} = \frac{1}{\omega Z_{base}} = \frac{1}{2\pi f_0 Z_{base}} \tag{5.18}$$

Therefore, the maximum capacitance can be derived from (5.17) and (5.18). With the limit given in (5.19), a capacitor with 12 uF is chosen.

$$C \leq 5\% C_{base} \tag{5.19}$$

5.1.3 Electromagnetic and electrical circuit simulations

Since the converter systems shown in Figure 5.1 are used in aerospace power grid application, there is a need for an output filter to meet the power quality limit except for the coupled inductors. The coupled inductors have higher inductance and lower current, comparing to the inverter-side inductor of the output filter, so the nano-crystalline and amorphous magnetic material can be considered for coupled inductor and output filter inductor, respectively. The coupled inductors are lighter than the inductor of output filter. The system specifications are presented in Table 5.1.

The simulated interleaving angle versus THD without any filter is presented in Figure 5.4 (a), and the simulated interleaving angle versus circulating current with 1 mH coupled inductor is presented in Figure 5.4 (b). Therefore, it is obvious that 180^0 interleaving angle is a better choice for inductor weight reduction.

Table 5. 1 System specifications

Parameter	Variable	Value
DC input voltage	V_{DC}	± 375V
AC output voltage	V_{AC}	230V (phase to neutral)
Output voltage frequency	f_0	400 Hz
Switching frequency	f_{sw}	60 kHz
Output power	P	100 kW
Modulation index	M	0.867
Inverter side inductor	L_{in}	13.8 uH
Capacitor	C	12 uF
Coupled inductor	L	1.63 mH

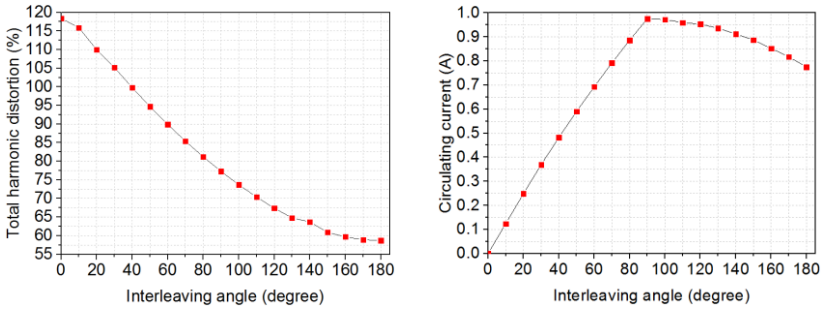

(a) (b)

Figure 5. 4 Simulated interleaving angle versus THD (a) and circulating current (b)

The inductance and maximum magnetic flux density for coupled inductor [104] and output filter inductor based on ANSYS Maxwell simulation are given in Table 5.2, and the flux distribution of the coupled inductor and the inverter-side inductor of the output filter are presented in Figures 5.5 (a) and 5.5 (b) respectively.

Table 5. 2 Inductor parameters

Types	Material	Inductance	B_{max} (T)
Coupled inductor	Nano-crystalline	1.63 mH	0.855
Filter inductor	Amorphous	13.8 uH	1.241

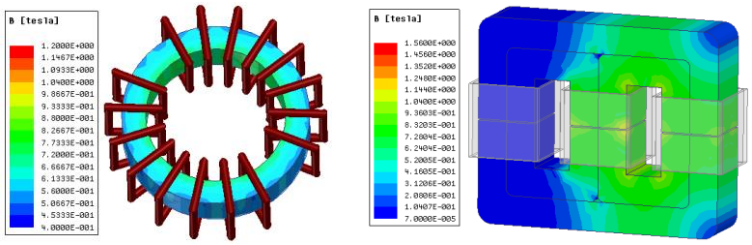

(a) (b)

Figure 5. 5 FEM simulation of flux distribution with coupled inductor (a) and inverter-side inductor of output filter (b).

Figure 5.6 presents the simulation results of the waveforms of voltage difference and the circulating current of two interleaved VSCs with 180^0 interleaving angle. Figure 5.7 shows the simulated inverter-side current and grid-side current waveforms, and the grid-side THD in Figure 5.8 meets the

requirement of RTCA DO-160 [11]. In this simulation, the leakage inductances of coupled inductor are ignored. In actual practical situation, these leakage inductances of the coupled inductors can be used as inverter-side inductors, but at the expense of higher losses in the coupled inductor.

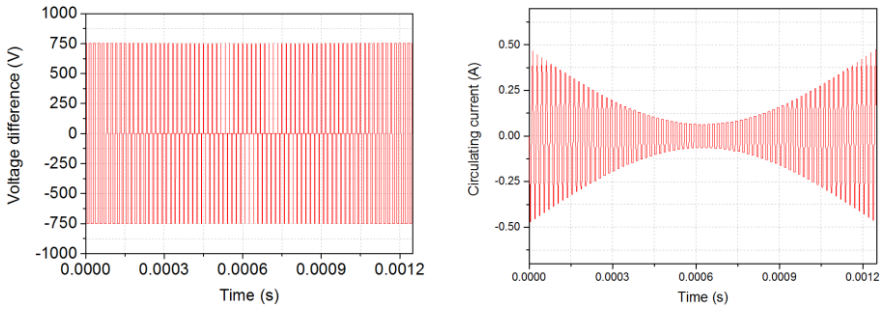

(a) (b)

Figure 5. 6 Simulation waveforms of voltage difference (a) and circulating current (b) of two interleaved VSCs for 180^0 interleaving angle.

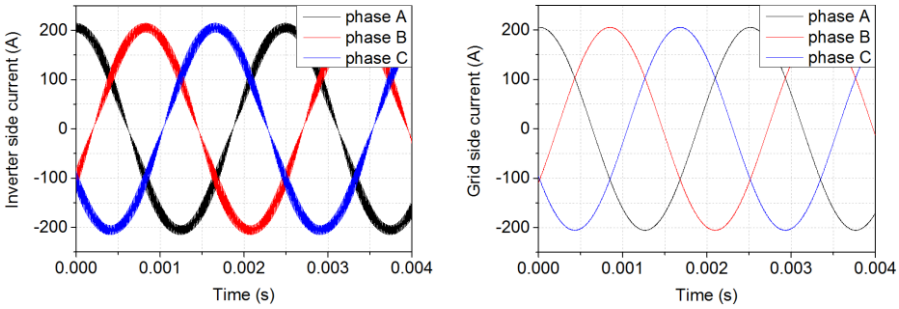

(a) (b)

Figure 5. 7 Simulation waveforms with inverter-side current (a) and grid-side current (b).

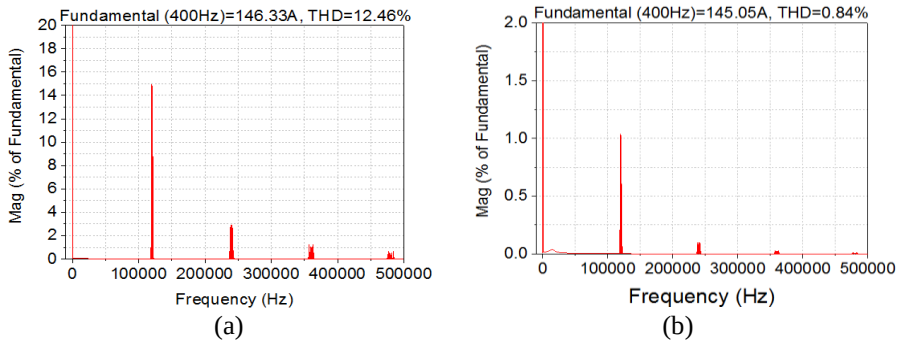

(a) (b)

Figure 5. 8 Simulation spectrum waveforms with inverter-side current (a) and grid-side current (b).

5.1.4 Inductor weight comparison with and without interleaving

The weights of the coupled inductor and the output filter inductor with and without interleaving are calculated with area product method and are presented in Table 5.3. For the interleaved converters system, the output filter inductor's weight reduces by 60.7%, and the total weight of the coupled inductor and the output filter inductor reduces by 38.7%. Therefore, interleaving method for VSCs is a good choice to increase the power density of the converter.

Table 5. 3 Weight comparison of coupled inductor and output filter inductor w and w/o interleaving with 60 kHz switching frequency

Weight (kg)	Output filter inductor	Coupled inductor	Total (kg)
W/O interleaving	15 (L_{in}:12 kg and 55 uH ; L_{grid}:3 kg and 33 uH)	0	15
W interleaving	5.9 (L_{in}:5.9 kg and 13.8 uH)	3.3	9.2
% Change	60.7		38.7

5.2 Harmonics and Common Mode Voltage Analysis with Different Power Converter Configurations

5.2.1 Introduction

With the exception of harmonics, CM voltage produced by standard PWM inverters is another major issue to cause EMI emissions [40, 105], which will affect the operation of some sensitive loads that shared the same aircraft power grid. Therefore, CM voltage analysis with different levels of power converter is necessary and will be discussed in this section. Figure 5.9 shows an example of the back-to-back converter system in MEA. In this section of chapter 5, it focuses on DC to AC inverter side of the back-to-back converter systems. The inverter configurations and three-phase aircraft power grids are firstly introduced. Then

analysis of harmonics in different inverter systems are given, and the CM voltage is evaluated. The methods to reduce harmonics and CM voltage will be reviewed. Finally, experimental verification and conclusions are summarized.

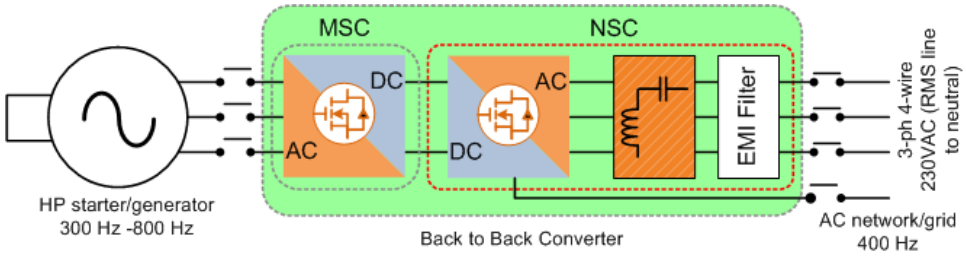

Figure 5. 9 Back to back converter system in aircraft.

5.2.2 Three-phase inverter configurations

Three kinds of inverter topologies namely two-level, three-level, and five-level are presented in Figure 5.10.

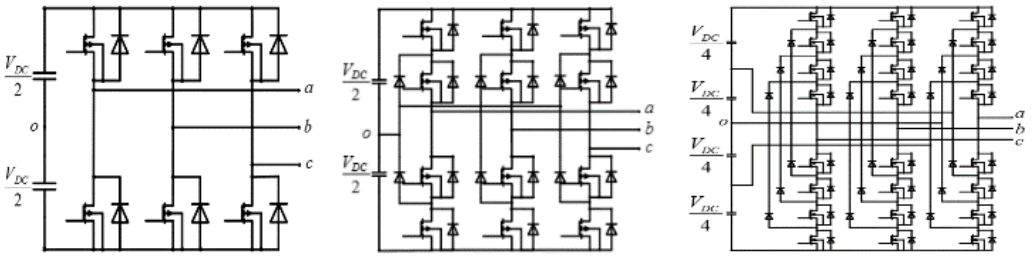

(a) (b) (c)

Figure 5. 10 Configurations of two-level inverter (a), three-level NPC inverter (b), five-level NPC inverter (c).

There are two three-phase configurations in different grid applications, the star and delta configurations. The delta configuration only needs three wires for power grid, while the star configuration utilizes the forth wire as the neutral wire. However, the star configuration produces higher output harmonics, as compared to delta configuration, as shown in Figure 5.11 (a), due to some of triple frequency harmonics flowing back to inverter from the neutral line.

5.2.3 THD analysis with passive filter

Table 5.4 gives the technical specifications of the inverter. Since there are higher losses in the inverter-side inductors with high switching frequency harmonics, the inverter-side current THD will be important to determine the weight of passive filter. Figure 5.11 (b) presents the THD of inverter-side with the same passive filter. It is obvious that higher level converter produces lower harmonics, and four-wire system also has higher THD.

Table 5. 4 Technical Specifications of the Inverter

Parameter	Variable	Value
DC input voltage	$V_{DC\text{-}input}$	± 375V
AC output voltage	$V_{AC\text{-}output}$	230V (phase to neutral)
Line frequency	f_0	400 Hz
Switching frequency	f_{SW}	60 kHz
Output power	P	50 kW

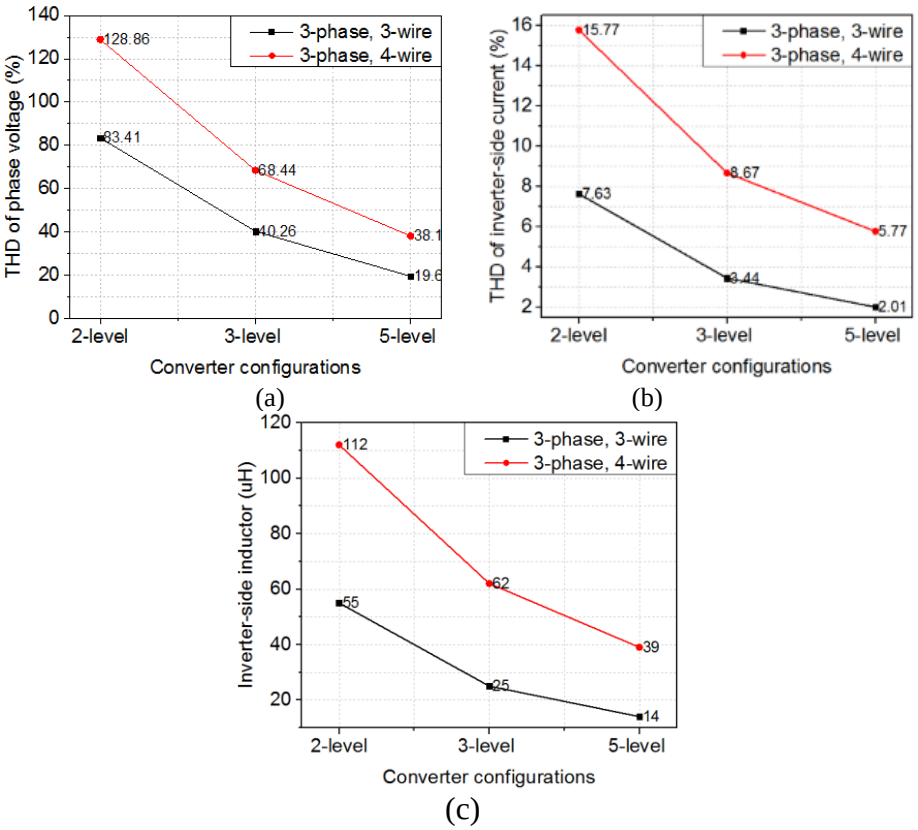

Figure 5. 11 (a) Phase voltage THD comparison with different converter systems; (b) Inverter-side current THD comparison with same passive filter and different converter systems; (c) Inverter-side inductance comparison with same inverter-side current THD.

The inverter-side current THD maintains around 7.7 %, and the inverter-side inductances of the passive filter are presented in Figure 5.11 (c). It indicates the feasibility of multi-level converter to reduce the weight of passive filter.

5.2.4 Common-mode voltage for different levels of inverters

The inverter CM voltage according to Figure 5.10 is defined as the voltage between mid-point of the DC-link capacitor and neutral point of phase leg as given by

$$V_{cm} = \frac{V_{ao} + V_{bo} + V_{co}}{3} \tag{5.20}$$

Where, V_{ao}, V_{bo}, and V_{co} are voltages of phases A, B, and C respectively.

The CM voltages under different switching states in Table 5.5 for a two-level inverter are listed in Table 5.6, with "1" and "0" denote the on-state of the upper and lower switching devices in one phase leg, respectively. For example, state "000" means that all lower switching devices of phases A, B and C are turned on.

Table 5. 5 Switching states of one phase leg with three-level NPC inverter

State of (S1, S2)		Phase voltage
1	0	$(+1/2)\cdot V_{DC}$
0	1	$(-1/2)\cdot V_{DC}$

Table 5. 6 CM voltage of two-level inverter for various switching states

State			CM voltage
0	0	0	$(-1/2)\cdot V_{DC}$
0	0	1	$(-1/6)\cdot V_{DC}$
0	1	0	$(-1/6)\cdot V_{DC}$
0	1	1	$(+1/6)\cdot V_{DC}$
1	0	0	$(-1/6)\cdot V_{DC}$
1	0	1	$(+1/6)\cdot V_{DC}$
1	1	0	$(+1/6)\cdot V_{DC}$
1	1	1	$(+1/2)\cdot V_{DC}$

The possible switching states with three-level neutral point clamped (NPC) converter for one phase leg is tabulated in Table 5.7. Three are four switches from upper to bottom in one phase leg: S1, S2, S3, and S4. According to Table 5.7, there are four kinds of CM voltages: 0, $\pm\frac{1}{6}V_{DC}$, $\pm\frac{1}{3}V_{DC}$, $\pm\frac{1}{2}V_{DC}$. However, with SPWM for a three-level inverter, the CM voltage of $\pm\frac{1}{2}V_{DC}$ will not occur. Therefore, there are only CM voltage with 0, $\pm\frac{1}{6}V_{DC}$, and $\pm\frac{1}{3}V_{DC}$ for a three-level inverter. The CM voltage of a three-level inverter is lower than that of a two-level inverter.

Table 5. 7 Switching states of one phase leg with three-level NPC inverter

State of (S1, S2, S3, S4)				Phase voltage
1	1	0	0	$(+1/2)\cdot V_{DC}$
0	1	1	0	0
0	0	1	1	$(-1/2)\cdot V_{DC}$

The phase voltage under different switching states of a five-level NPC for one phase leg is tabulated in Table 5.8. Three are eight switches from upper to bottom in one phase leg: S1, S2, S3, S4, S5, S5, S7, and S8. With SPWM for a five-level inverter, the CM voltage level of 0, $\pm\frac{1}{12}V_{DC}$, and $\pm\frac{1}{6}V_{DC}$ exists. The five-level inverter has the lowest CM voltage amongst these three inverter configurations.

Table 5. 8 Switching states of one phase leg with five-level NPC inverter

State of (S1, S2, S3, S4, S5, S5, S7, S8)								Phase voltage
1	1	1	1	0	0	0	0	$(+1/2)\cdot V_{DC}$
0	1	1	1	1	0	0	0	$(+1/4)\cdot V_{DC}$
0	0	1	1	1	1	0	0	0
0	0	0	1	1	1	1	0	$(-1/4)\cdot V_{DC}$
0	0	0	0	1	1	1	1	$(-1/2)\cdot V_{DC}$

The CM voltage (V) for two-level, three-level, and five-level inverter configurations are simulated and shown in Figure 5.12, which is the consistant

with the earlier analysis. The high-level inverter contributes to lower CM voltage. Also, there is no zero CM voltages in a two-level converter, but the multi-level inverter has zero CM voltage in some switching states.

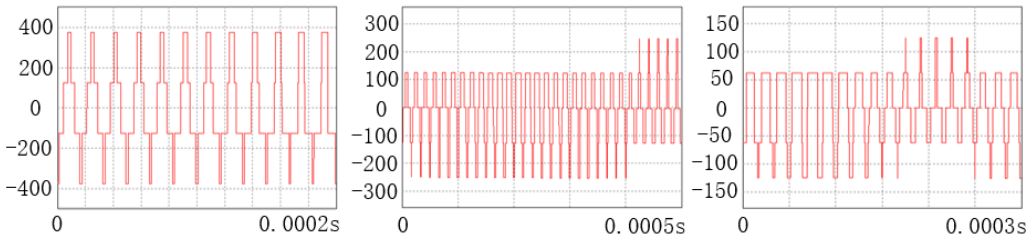

(a) (b) (c)

Figure 5. 12 Common mode voltage of two-level inverter (a), three-level NPC inverter (b), five-level NPC inverter (c).

5.2.5 Experimental results

The inverter systems with two-level three-phase three-wire and two-level three-phase four-wire configurations are tested with the passive filter.

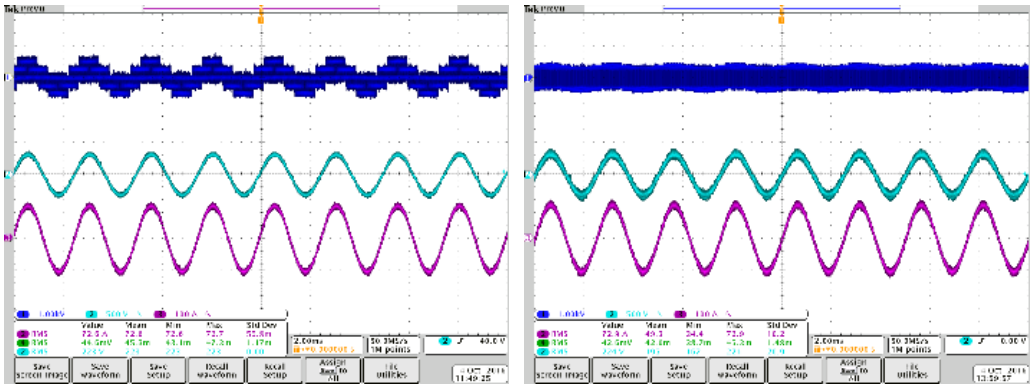

(a) (b)

Figure 5. 13 Inverter side phase voltage (channel-1), network-side phase voltage (channel-2), and network-side current (channel-3) of two-level inverter with (a) three-phase three-wire and (b) three-phase four-wire inverter.

From the measured waveforms in Figure 5.13, the voltage THD of the inverter-side and the network-side for two-level three-phase three-wire system are 85.21% and 6.65%, respectively. While for the two-level three-phase four-wire system, the voltage THD of the inverter-side and the network-side are 116.91%

and 12.17% respectively. Hence, the three-wire system has lower harmonics than that of the four-wire system.

5.3 Summary

With optimal design of the coupled inductor and output filter inductor, the first section presents a detailed THD analysis for an interleaved three-phase VSCs with grid-connected application. The FEM simulation of the coupled inductor and the output filter inductor determines the inductances with magnetic flux density constraints. The electrical circuit simulation results show that the given coupled inductance and output filter inductance have the ability to bring the grid-side current harmonics below the THD limit.

This second section has analyzed the harmonic and CM voltage generated by different inverter configurations in the aircraft power network. The three-phase three-wire system has lower THD, as compared to three-phase four-wire system, which is verified experimentally with a two-level inverter system. Multi-level inverter will require smaller size of passive filter to meet the power quality requirement, but at the expense of additional switching devices, heatsinks, and auxiliary circuits. In addition, the inverter with higher level leads to lower CM voltage. Therefore, optimization and selection of inverter topology and the required filter are important to MEA network.

Chapter 6 Evaluation of Electrical-Magnetic-Thermal Characteristics for Three-Phase Common Mode Choke

In this chapter, the design of key component of coupled inductor and EMI filter, namely common-mode choke (CMC), will be analysed. Various design parameters that effect its performance are investigated and verified experimentaliry.

6.1 Electromagnetic characteristics of three-phase common-mode choke

6.1.1 Introduction

Due to high frequency switching and parasitic elements of power semiconductor devices, CM and DM conducted EMI will be generated in power converter system. To meet the electromagnetic compatibility (EMC) requirement, an EMI filter is necessary. One of the key filtering components of the EMI filter is a CMC, which provides high CM impedance to suppress CM current. Besides CM inductance, a CMC also exhibits finite DM inductance due to leakage inductance. In addition, the maximum flux density that causes saturation in the magnetic core and the parasitic capacitance of the CMC also affect its overall EMI suppression performance. Hence, a comprehensive study of how these parameters affect its performance will be useful to achieve optimal CMC design.

3D finite element method (FEM) simulation tool is adopted for the CMC analysis. Zhu, Ning, et al adopt the FEM for calculating CM and DM inductances under linear condition [106]. A Khodakarami, et al use ANSYS to investigate the leakage inductance of a pulse transformer [107]. Chen, Henglin, et al analyses

the core saturation due to DM current for a CMC [108]. Kovacic, Marinko, et al extract the parasitic capacitance of CMC with FEM [109]. The motivation of the first section for this chapter aims to extract all these parameters and investigate their impacts on a CMC's EMI suppression performance.

6.1.2 Extraction of CM and DM Inductances

The primary function of a CMC is to provide CM inductance. When the CM current flows through a CMC, the magnetic flux in the core adds and produces a CM inductance to suppress CM current. Ideally, the sum of the three-phase balanced DM current equals to zero and the magnetic flux within the core produced by the DM current cancel out. In reality, the CM and DM currents not only generate the magnetic fluxes inside the core, but also generate magnetic flux outside the core, and this external flux results in leakage inductance and at the same time gives rise to partial saturation of the core, as illustrated in Figure 6.1. The CM currents are in the same direction and in phase; and the DM current has 120^{o} phase difference between any two phases. To validate the FEM model of, a three-phase CMC with VAC 6123 × 140 toroidal core, as illustrated in Figure 6.2, will be simulated and compared with measurement results. The magnetic properties of the toroidal are specified in [110]. For the CMC model, the initial relative permeability is close to 7.7×10^{4} in the frequency range 1 kHz – 100 MHz, and for high frequency, the complex permeability need to be considered for proper modelling of core material.

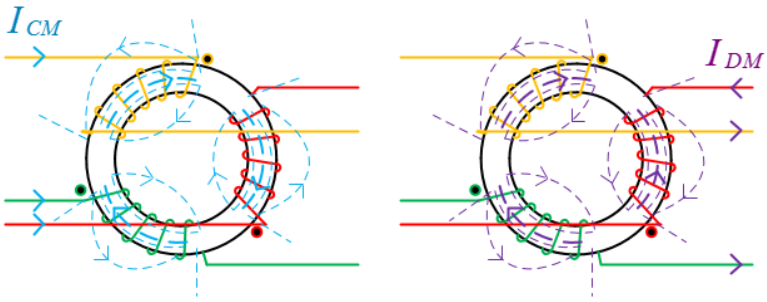

Figure 6. 1 Magnetic fluxes due to CM and DM currents flowing in a three-phase CMC

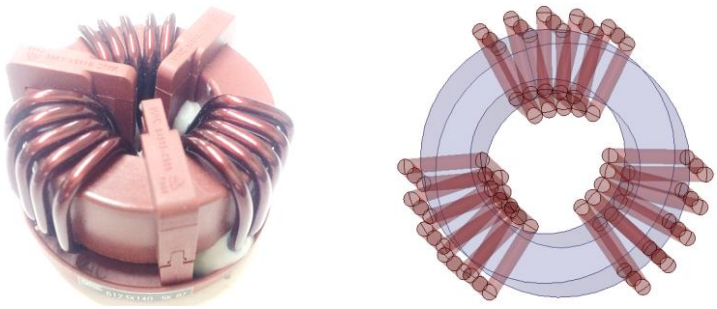

(a) (b)

Figure 6. 2 Three-phase CMC with VAC 6123 × 140 core (a) and its 3D FE model (b)

The CM currents flowing in three-phase inductors wound on the toroidal core generate the magnetic flux within the core with the same polarity. For three-phase balanced windings, the common-mode (CM) inductance is given by

$$L_{CM} = N^2 A_c \frac{u_0 u_r}{l_c} \tag{6.1}$$

where N is the number of turns per phase, A_c is the cross section of the magnetic core, μ_o is the permeability of vacuum, μ_r is the relative permeability of magnetic core, and l_c is the magnetic path of within the core.

The DM inductance is owing to the leakage flux outside the core, as mentioned earlier and shown in Figure 6.1. The leakage flux has lower effective permeability and results in finite DM inductance. In FEM model, the leakage

inductance can be obtained from the difference between the total energy of the CMC and the energy within the core as follows

$$W_{leakage} = W_{total} - W_{core} \tag{6.2}$$

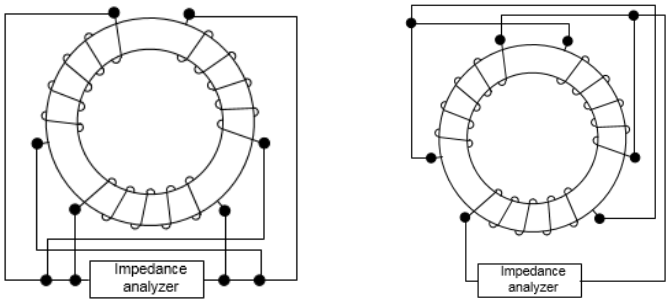

(a) (b)

Figure 6. 3 CM and DM inductances measurement setups. (a) CM (b) DM

Once the leakage energy is obtained, the DM inductance can be calculated by

$$L_{DM} = \frac{2W_{leakage}}{i_{DM}^2} \tag{6.3}$$

The CM and DM inductances measurement setups are shown in Figure 6.3 (a) and Figure 6.3(b), respectively. Table 6.1 compares the simulated and measured CM and DM inductances at the frequency of 1 kHz with HP 4294A Precision Impedance Analyzer. It shows that the extracted CM and DM inductances from the FEM model agree reasonably well with the measured results.

Table 6. 1 Simulated and Measured CM and DM inductances

	CM inductance (mH)	DM inductance (μH)
Simulation	3.058	1.997
Measurement	3.001	2.506

6.1.3 Core saturation analysis CM and DM currents excitation

In CMC design, the maximum flux density is also an important determinant to consider for core saturation and core loss. This section analyses the core saturation of CMC due to the sum of CM and DM currents. The magnetic flux due to CM current can be computed as follows

$$B_{CM,pk} = \frac{u_0 u_r 3NI_{CM,\max}}{l_c} \tag{6.4}$$

High DM current and leakage flux due to winding structure has a strong influence on the core saturation. Taking into account both CM and DM magnetic fluxes within the core, total magnetic flux density must meet the following requirement to avoid core saturation.

$$B_{CM,pk} + B_{DM,pk} \leq B_{sat} \tag{6.5}$$

The magnetic flux density distributions are computed by 3D Ansys maxwell, as shown in Figure 6.4. By increasing the CM current from 10 mA to 40 mA, the magnetic flux density increases from 0.269 T to 1.077 T, as given in the plot shown in Figure 6.7.

Because of the leakage flux produced by the three-phase DM current, it causes non-zero flux density within the core, as depicted in Figure 6.5. The relationship between flux density and the DM current is shown in Figure 6.8.

Under practical operations, both CM and DM currents co-exist. The resultant maximum magnetic flux density within the core due to the combined CM and DM currents is shown in Figure 6.6. It is found that the total flux density

with combined CM and 25 A DM currents is higher than the magnetic flux densities with only CM current excitations, as plotted in Figure 6.9.

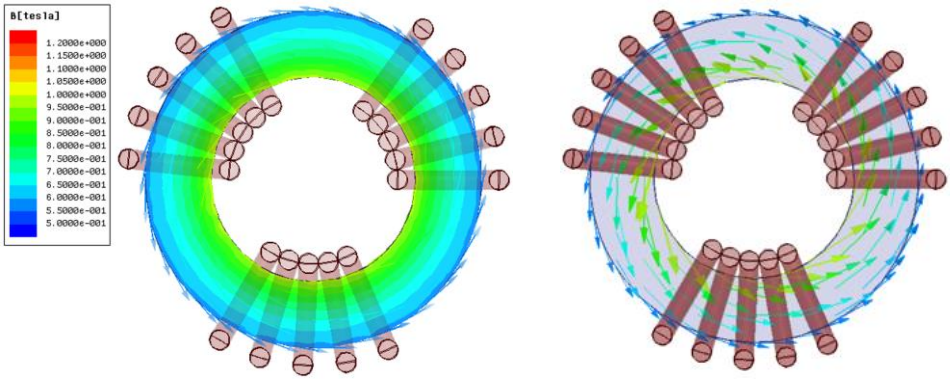

Figure 6. 4 CM magnetic flux density and vector distribution under 40 mA CM current excitation

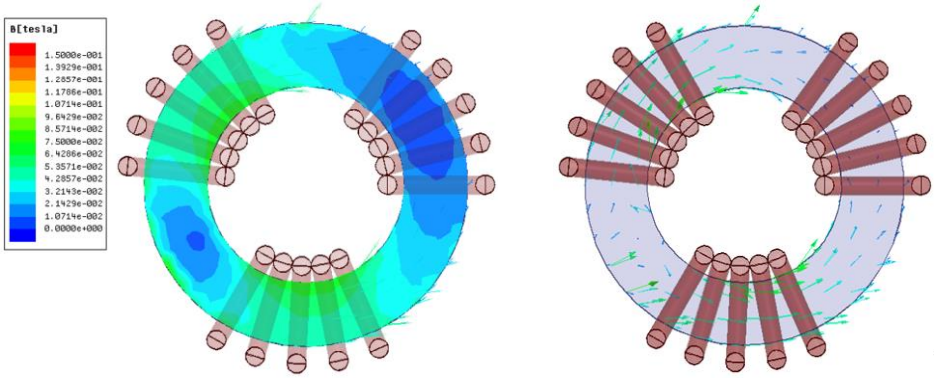

Figure 6. 5 DM magnetic flux density and vector distribution under 25 A DM current excitation

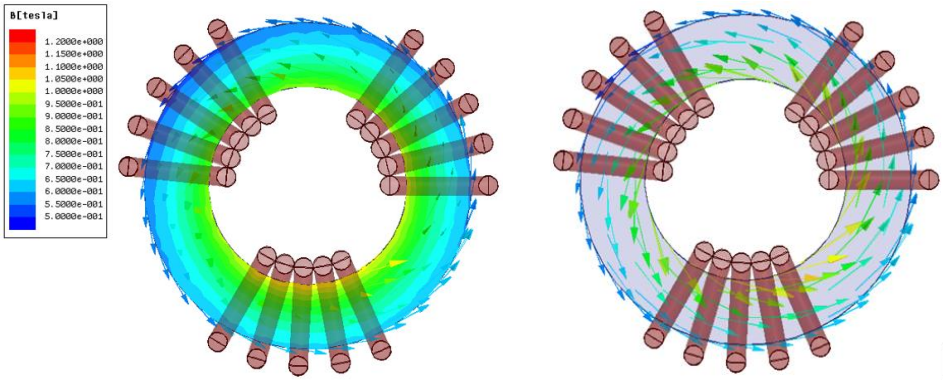

Figure 6. 6 Combined magnetic flux density and vector distribution under both 40 mA CM current and 25 A DM currents excitation

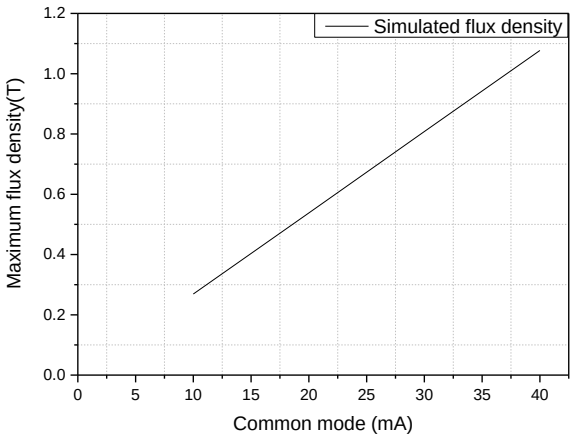

Figure 6. 7 Magnetic flux density with CM current excitation

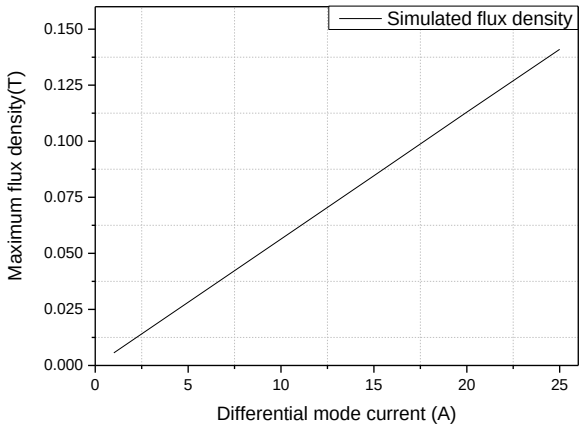

Figure 6. 8 Magnetic flux density with DM current excitation

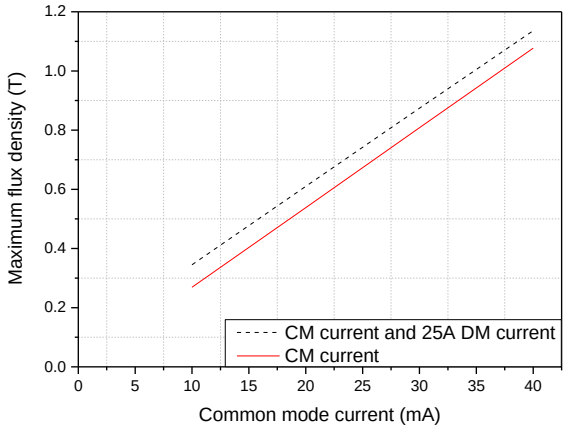

Figure 6. 9 Magnetic flux density with combined CM and CM currents excitation

6.1.4 Parasitic capacitances and impedance frequency responses

If one turn is energized with 1 V and the other turns of the core is set at 0 V, the parasitic capacitance can be calculated from the surface charge and the potential difference between the energized objects with the following expressions,

$$C = \frac{Q}{V} \tag{6.6}$$

where C is the parasitic capacitance, Q is the surface charge,

and V is the electric potential between the objects.

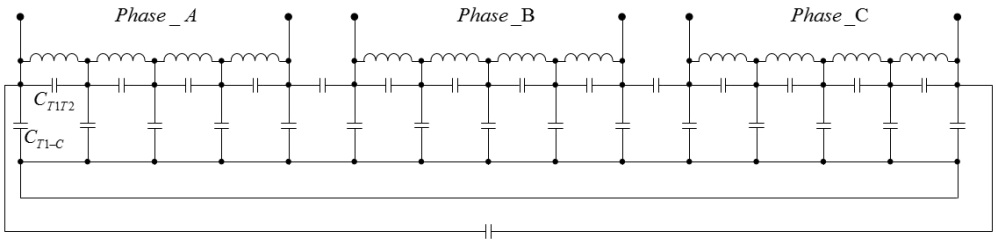

Figure 6. 10 Turn-to-turn capacitance and turn-to-core capacitance of a CMC.

The CMC has two contributors of parasitic capacitance, the turn-to-turn capacitance and turn-to-core capacitance, as illustrated in Figure 6.10.

To investigate the influence of winding layout on the parasitic capacitance, two different winding layouts of a CMC with the similar core structure are modeled and simulated. Each phase of winding has 5 turns. The first winding layout has is 13.5^{o} interval between turns and the winding of each phase is separated further apart, as shown in Figure 6.11 (a). The second winding layout has 24^{o} interval between turns and the winding of each phase is evenly spaced, as illustrated in Figure 6.11 (b). The extracted turn-to-turn capacitances and turn-to-core capacitances are tabulated in Tables 6.2 and 6.3, respectively.

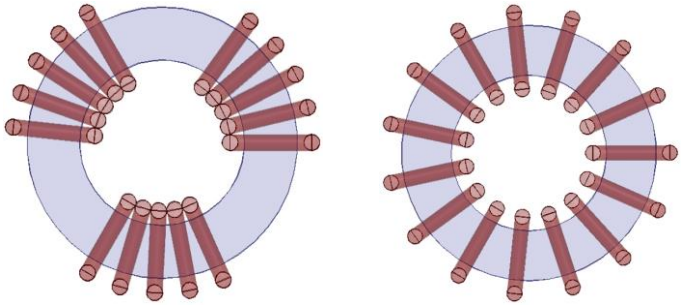

(a) (b)

Figure 6. 11 Three-phase balanced CMC with two winding layouts. (a) 13.5° interval between turns (b) 24° interval between turns

Table 6. 2 Turn-to-turn capacitance Comparison

Turn-to-turn capacitance					
13.5° interval			24° interval		
From	to	Capacitance, pF	From	to	Capacitance, pF
A1	A2	7.15	A1	A2	1.96
A2	A3	8.36	A2	A3	1.96
A3	A4	7.52	A3	A4	1.96
A4	A5	7.73	A4	A5	1.95
A5	B1	2.80	A5	B1	1.96
B1	B2	7.87	B1	B2	1.96
B2	B3	7.62	B2	B3	1.97
B3	B4	7.94	B3	B4	1.96
B4	B5	7.66	B4	B5	1.95
B5	C1	2.83	B5	C1	1.96
C1	C2	7.35	C1	C2	1.97
C2	C3	7.35	C2	C3	1.96
C3	C4	7.92	C3	C4	1.96
C4	C5	7.95	C4	C5	1.96
C5	A1	2.85	C5	A1	1.96

In Table 6.2, A, B and C denote the respective windings of the three phases. The numbers 1, 2, 3, 4 and 5 denote the specific turn of each winding.

It is obvious that the second winding layout exhibits smaller turn-to-turn and turn-to-core parasitic capacitances, which is expected to enhance the high frequency performance of the CMC. Based on the equivalent circuit model given in Figure 6.10, the CM and DM impedances of the CMC versus frequency are simulated and measured, as given in Figures 6.12 and 6.13, respectively.

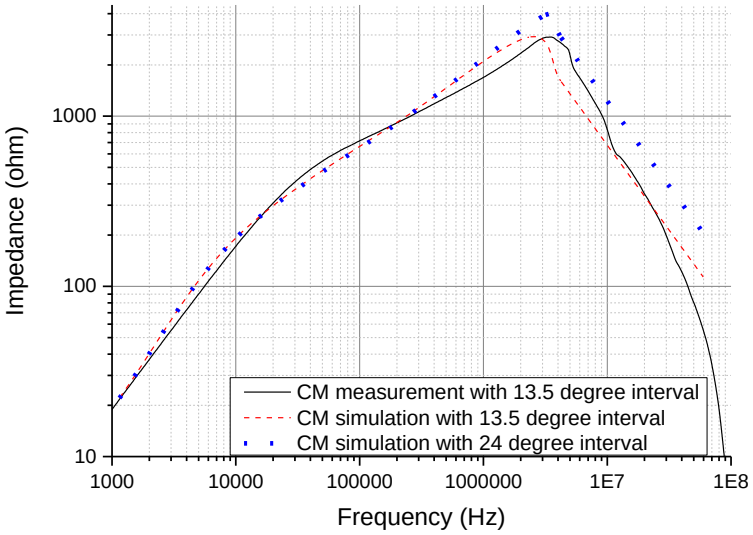

Figure 6. 12 CM impedance versus frequency

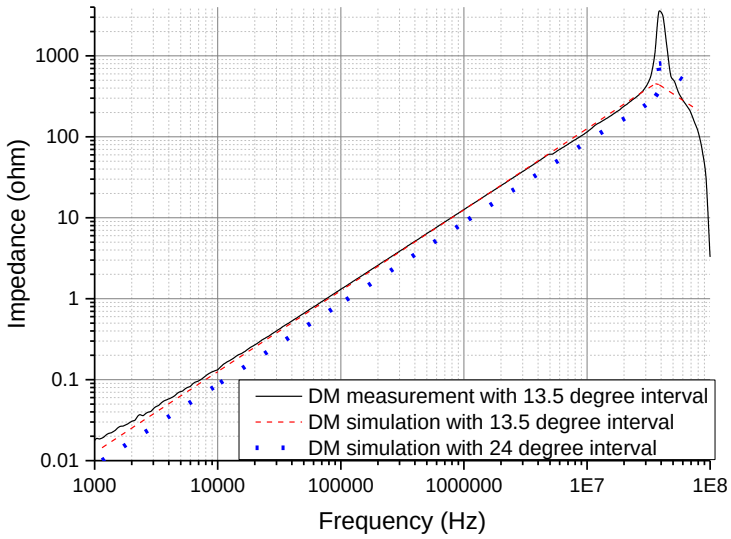

Figure 6. 13 DM impedance versus frequency

Based on the CM and DM impedance responses, the effective CM and DM parasitic capacitances of the two winding layouts are extracted and given in Table

6.4. It confirms that the second winding layout is better due to much lower CM and DM parasitic capacitances.

6.1.5 Evaluation of different core structures

Besides the winding layouts, cross-sectional shapes of magnetic core will also affect the CMC's performance. Four different core structures with different cross-sectional shapes, as shown in Figure 6.14, will be evaluated.

Table 6. 3 Turn-to-core capacitance Comparison

Turn-to-core capacitance			
13.5º interval		24º interval	
From	Capacitance, pF	From	Capacitance, pF
A1	5.02	A1	3.30
A2	6.17	A2	3.26
A3	6.48	A3	3.28
A4	6.22	A4	3.31
A5	5.15	A5	3.28
B1	5.10	B1	3.30
B2	6.02	B2	3.27
B3	6.37	B3	3.29
B4	6.20	B4	3.28
B5	5.00	B5	3.27
C1	5.15	C1	3.27
C2	6.11	C2	3.27
C3	6.35	C3	3.30
C4	6.21	C4	3.27
C5	5.18	C5	3.27

Table 6. 4 Effective CM and DM Parasitic Capacitances

Parasitic capacitance	13.5º interval	24º interval
CM	23.52 pF	12.97 pF
DM	9.40 pF	5.25 pF

Their maximum magnetic flux densities and inductances at 0.01 mA CM current and 1 kHz frequency are simulated and tabulated in Table 6.5. The cross section 32 mm×4 mm of core almost has the same CM inductance but is not easily saturated and has higher DM inductance, comparing to the other three different core structures.

Table 6. 5 Comparison of Maximum magnetic flux density and inductance with four different core cross sections

Core height (mm) ×thickness (mm)	Bsat (T) Bmax=1.22 T	CM Inductance (mH)	DM inductance (uH)
16×8 (13.5°)	0.237	3.058	1.997
11.3×11.3 (square)	0.263	3.112	1.723
Radius=6.38 (circular)	0.243	3.075	1.633
32×4	0.213	3.003	2.717

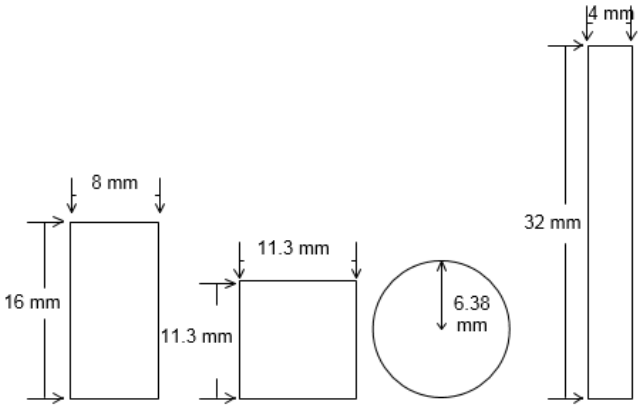

Figure 6. 14 Four different cross section of CMC

6.2 Thermal analysis of three-phase common-mode choke

6.2.1 Introduction

Besides harmonics, the CM voltage produced by SPWM inverters also generates EMI emissions [40, 105], Therefore, passive filters are needed at the grid-side of the HPDC to ensure both power quality [30] and EMC. To achieve compactness, the switching frequency of the power converter has been increasing in recent years with the development of WBG devices [111], which results in higher core loss in the CMC. The focus of the second section for this chapter will be on thermal analysis of CMC with the aid of 3-D FEM computational fluid dynamics (CFD). Nano-crystalline and Finemet cores are usually chosen for CMC design for their high permeability [81, 82].

An indirect air cooling system for magnetic devices which combines the transformer with a heat sink and a heat transfer component is presented[112]. High density EMI filter design in high power three-phase motor drive systems with liquid cooling system was reported, but no comprehensive thermal analysis using 3-D FEM+CFD for CMC with liquid cooling system was carried out [39]. The 3-D thermal finite analysis coupled to models for inductor core and winding loss has been studied [113]. However, the in-depth understanding of the interactions between the losses of CMC and its temperature with a liquid cooling system is very useful to evaluate its performance under specific operating conditions, which is the objective of this section.

6.2.2 Thermal modelling and temperature rise prediction

When DM and CM currents flow into the windings of CMC, the copper and core losses will be produced. Prediction of the temperature rise of CMC is needed to ensure it meets its intended operating temperature environment. The CMC equivalent thermal circuit model is the same as the inductor's thermal model as illustrated in Figure 3.10. The definition of thermal resistance R is given by:

$$R = \frac{q}{\theta} \tag{6.7}$$

where q is loss and θ is the temperature rise.

From (6.7) and thermal modelling, the temperature of CMC mainly depends on the total loss of CMC, the ambient temperature, and the thermal resistance between liquid and ambient. In addition, the thermal conductivity coolant

encapsulated into casing, flow rate of piped coolant and properties of inlet coolant of the pipe of the cooling system will also have their effects on the temperature of CMC.

The three-phase CMC with VAC V080 core and Litz wire handling 100 A peak current of 5 turns per phase is selected and analyzed, and the CM inductance is 0.644 mH. The core surface is around 212.5 cm^2, the core weight is about 0.59 kg and the total weight of CMC is around 1.05 kg. The temperature rise equation of inductor in terms of various losses and the core surface is related by [114]:

$$\Delta T = 450\left(\frac{p_{core} + p_{copper} + p_{air\ gap}}{A_{sur}}\right)^{0.826} (^{\circ}C) \tag{6.8}$$

As an example, the maximum tolerable loss is about 15 W if the allowable temperature rise is 50 ^{o}C. Also, it is worth to note that the major contribution of the total loss comes from the core loss. To enhance the power density of CMC, liquid cooling is the only option.

6.2.3 3-D simulation of liquid cooling for CMC

The CMC is investigated by CFD with ANSYS Fluent, which has been verified as a good thermal simulation tool in chapter 3. Coolants such as oil and fuel are readily available in aircraft at 343.15 K. Table 3.11 lists three common liquid coolants. The CMC with toroidal core is placed within an Aluminum casing and encapsulated with high thermal conductivity coolant, Duralco 128, as shown in Figure 6.15. The net weight of one-side cooling system is 0.85 kg and the net weight of two-side cooling system is 1.17kg.

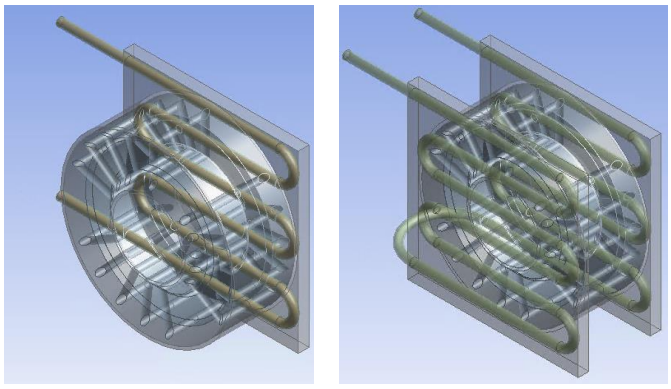

(a) (b)

Figure 6. 15 CMC liquid cooling system with one-side cooling (a) and two-side cooling (b)

Table 6.6 gives the thermal properties of the liquid cooling system. Figure 6.16 shows the nanocrystalline core segment. The thermal conductivity is 10 W/(m·K) along the lamination and the thermal conductivity is 0.5 W/(m·K) against the lamination. Therefore, to increase the thermal conduction of CMC, the liquid cooling system design is better to be on the two sides of the toroidal core.

Table 6. 6 Thermal properties for CMC liquid cooling system

Name	Density (kg/m^3)	Specific heat (J/kg-K)	Thermal conductivity (w/m-K)
Nanocrystalline	7300	~500	10 (lamination)
Duralco 128	980.6	1000	4.324
Water	998.2	4182	0.6
PBT (bobbin)	1630	1200	0.24
Copper	8978	381	387.6
Aluminium	2719	871	202.4

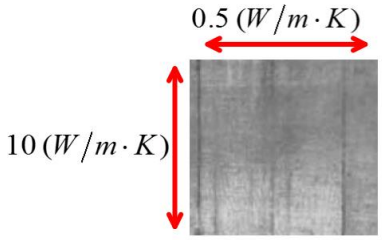

Figure 6. 16 Thermal conductivity of Nanocrystalline segments.

Table 6. 7 Properties for Nanocrystalline

Saturation flux density	1.2 T
Core filling factor	0.7
Continuous operating temperature	120 ℃

Table 6.7 gives the magnetic and thermal properties of nanocrystaline at 120 ℃ since this material recrystallization with high temperature may produce thermal ageing [115]. Then the simulation with different conditions are presented. Firstly, the two different cooling systems, one-side and two-side cooling systems are compared. As expected, the two-side cooling system has a better thermal performance. Then, the different losses of CMC are also analyzed and the maximum tolerable total loss is determined by the 3-D modelling analysis. Since the lower flow rate cannot absorb so much heat and the higher flow rate will be saturated, the most optimal flow rate can be simulated and selected. Finally, the ambient temperature and different coolants and their effects on the liquid cooling system are evaluated.

Firstly, the one-side and two-side cooling systems are as shown in Figures 6.15 (a) and (b), respectively. Figure 6.17 shows the core temperature distribution with liquid cooling under the following conditions: 60 W core loss, 2 LPM flow rate and 343.15 K ambient temperature. Table 6.8 presents the simulation results.

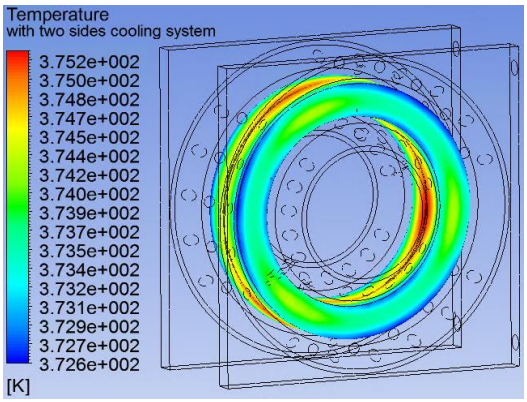

Figure 6. 17 CMC core temperature distribution with the core loss of 60 W, flow rate of 2 LPM and ambient temperature of 343.15 K.

Table 6. 8 Cooling sides effects on core temperature rise（℃）

Core loss (W)	60	80	100
1-side cooling	84.28	123.04	135.80
2-side cooling	77.35	115.16	125.01

Secondly, this simulation investigates the core loss effects on core temperature. The ambient temperature is 343.15 K and the flow rate is 2 LPM. The simulation results are tabulated in Table 6.9.

Table 6. 9 Core loss effects on core temperature（℃）

Core loss (W)	60	80	100
2-side cooling	77.35	115.16	125.01

Thirdly, different flow rates are simulated to cool the CMC, with the same core loss of 100 W and ambient temperature of 343.15 K. Table 6.10 shows the flow rate effects on core temperature.

Table 6. 10 Flow rate effects on core temperature（℃）

Flow rate (LPM)	2	4	6
2-side cooling	125.01	99.62	99.55

Fourthly, to understand the ambient temperature effect on core temperature, the simulation with three different ambient temperatures are done under the same core loss of 100 W and flow rate of 2 LPM, as shown in Table 6.11.

Table 6. 11 Ambient temperature effects on core temperature rise（℃）

Ambient temperature (K)	298.15	320.65	343.15
2-side cooling	54.44	76.83	125.01

Lastly, the coolants of water, oil and fuel are simulated with the same core loss of 100 W, flow rate of 2 LPM and ambient temperature of 343.15 K, as given in Table 6.12

Table 6. 12 Coolants effects on core temperature rise（℃）

Ambient temperature (K)	Water	fuel	oil
2-side cooling	125.01	130.23	173.56

Overall, the increase of twice the weight of CMC with the liquid cooling system allows six times higher loss of CMC as compared to the case without the liquid cooling system. Hence, CMC with liquid cooling system is worth exploring for HPDC design.

6.3 Summary

In the first section and based on the 3D FEM electromagnetic model, the CM inductance and leakage inductance for a CMC are extracted. Then the magnetic flux densities excited by the CM current, DM current, combined CM and DM currents are also analyzed. To optimize the design of CMC, parasitic capacitance with two different winding layouts is investigated, and the second winding layout with 24^{o} interval between turns has smaller parasitic capacitance; finally, maximum flux density and inductance of with four different cores are

evaluated. They have almost the same CM inductance, and the core with the cross section 32 mm×4 mm is found to be less prone to be saturated and exhibits higher DM inductance, compared to the other three types of cores.

The second section reviews the cooling concepts for high power density magnetic components. The liquid cooling system is also proposed for CMC in HPDC application. With CFD analysis, the different conditions include core loss, flow rate, sides cooling, ambient temperature, coolants are investigated and discussed, which serves a useful guide to design high power density CMC.

Chapter 7 Conclusion and Future work

7.1 Conclusion

In this thesis, the major contributions are the development of systematic approach of filter design and optimization of magnetic components for HPDC with size and thermal considerations. The main focuses of this thesis are summarized as follows.

A comprehensive electric-magnetic-thermal-fluid analysis of LCL filter design is first presented. The HPDC with PWM modulation generates high switching frequency and multiples of switching frequency harmonics, as well as their side-band harmonics. With the carefully designed LCL filter, the calculated harmonics agree well with the measured results, and the THD has met the power quality requirement. Then these harmonic components are used to calculate the loss of the Litz wire with Dowell's equation. The prototype of an inductor with magnetic and thermal design via is fabricated, whose losses are measured by power analyzer. The inductor core losses are obtained though that the inductor loss subtracts the wire loss. After that, the inductor core losses and the wire losses are put into the ANSYS Fluent to analyze the temperature distribution and cooling system design. The comparison error of simulation and experiment for cooling system model is around 10 %, which validates that the model is effective. To further investigates the cooling system, the cooling performance of these three liquids such as water, fuel, and oil are compared and discussed, and the fuel is the best solution for aerospace applications.

Magnetic integration can reduce the total weight and size of LCL filter in HPDC system. The delta-yoke composite core is proposed to improve the density of LCL filter, compared to rectangular yoke core. The delta-yoke composite core with one inductor is first compared with the rectangular yoke core, which indicates that the inductor with the delta-yoke composite core has more balance three-phase inductances and lower flux density. Then the delta-yoke composite core moves to magnetic integration of LCL filter, and the mutual coupling coefficient between two inductors integration of LCL filter are analyzed by ANSYS Maxwell. With the same thickness of common yoke, the delta-yoke integrated inductors have lower coupling coefficient, which has lower side effect on the performance of LCL filter. Finally, the three-phase integrated inductors prototypes of LCL filter with rectangular yoke and delta-yoke are verified with temperature measurement for hot spot investigation and THD detection, and both integrated inductor meet the THD and thermal requirements. Besides, the delta-yoke integrated inductors not only can reduce the weight, but also has lower flux density and lower mutual coupling coefficient.

To further improve power density of HPDC system, the parallel interleaved and multi-level converter configuration are investigated. First, the parallel interleaved two voltage source converters are analyzed and simulated. The double integral Fourier analysis approach are employed to analyze AC side harmonics current, and some of switching harmonics can be eliminated with the certain phase-shifting of carrier wave between these two VSCs. What's more, to suppress the circulating current between these two VSCs, the coupled inductors

can be injected. Then, the coupled inductance and output filter parameters are finalized with the variance of phase-shifting, and the 180^o gives the lowest weight of coupled inductor and output filter, which is reduced by 38.7 % compared to the non-interleaved two VSCs. Secondly, analysis of harmonic and CM voltage with two-level, three-level, and five-level converter topologies are presented. The multi-level converters such as three-level and five-level, have lower output harmonics and CM voltage, compared to two-level. The output THD are almost reduced to half with the two-level to three-level, or three-level to five-level, as well as the amplitude of CM voltage, which leads to smaller output filter and EMI filter. However, multi-level converter needs more complex control and hardware design. The trade-off between level of converter and weight of converter should be optimized in future work.

Due to the high frequency switching and the parasitic parameters of SiC MOSFET devices, the high frequency noises such as coupled inductor for circulating current and common mode choke for common mode noise are required to be reduced or suppressed, and the performance evaluation of common mode choke is good for coupled inductor design and EMI filter design. The characteristics of CIs or CMC mainly include CM inductance and leakage inductance, the magnetic flux density excited by CM and DM current, parasitic capacitance with different winding layout, and magnetic flux density and inductances with different core structures. These characteristics are first analyzed with formula or simulated by 3-D FEM, and are then verified by experiments. The differences between simulation and experiment are within the acceptable

range. In addition, due to higher core loss and harsh operating temperature environment in aerospace, thermal analysis of CMC is also necessary as part of the EMI filter design. Then the second section of this chapter reviews of cooling concepts for high power density magnetic components, and thermal modeling of CMC. Cooling systems of CMC with 3-D FEM method are designed and compared with different operating conditions.

7.2 Future work

The future works that are worth exploring are recommended below.

Optimization of the coupled inductors and output filter of different magnetic material at high switching frequency with cooling system for high power density two parallel interleaved voltage sources converters can be further investigated. The parallel interleaved VSCs not only increases the output power, but also reduces the weight of the passive filter with high switching frequency. Because of high operating temperature in aircrafts, the advanced liquid cooling system design for passive components can further improve power density, compared to forced air cooling.

Further work on the multi-level converter such as three-level converter is also one possible future direction for high power density system. On one hand, the output THD of three-level converter can be reduced to half, compared to two-level converter, on the other hand, the three-level converter is easier to control and balance the DC-link capacitor voltage, compare to five-level or higher levels

converter. Another consideration of selecting the level for converter is the weight trade-off among devices, heatsink, and passive filter.

With the switching frequency continues to increase, the high frequency modelling of inductor's core losses still has room for further research, as accurate estimation of these losses allows proper choices of thermal management for pushing the boundary of high power and high density magnetic component design.

List of Publications

Journal Publications

As first author:

1. **Y. Liu**, K. Y. See, S. Yin, R. Simanjorang, C. F. Tong, A. Nawawi, and J. S. Lai, "LCL Filter Design of 50 kW 60 kHz SiC Inverter with Size and Thermal Considerations for Aerospace Applications." *IEEE Transactions on Industrial Electronics*, vol. 64, No. 10, pp. 8321 – 8333, 2017.

2. **Y. Liu**, K. Y. See, K. J. Tseng, R. Simanjorang, and J. S. Lai, "Magnetic Integration of Three-Phase LCL filter with Delta-Yoke Composite Core." *IEEE Transactions on Power Electronics*, vol. 32, No. 5, pp. 3835 - 3843, 2017.

3. **Y. Liu**, K. Y. See, S. Yin, R. Simanjorang, A. K. Gupta and J. S. Lai, "Equivalent Circuit Model of High Power Density SiC Converter for Common-Mode Conducted Emission Prediction and Analysis." *IEEE Electromagnetic Magazine*, 2017, accepted.

As co-author:

4. A. Nawawi, C. F. Tong, S. Yin, A. Sakanova, Y. T. Liu, **Y. Liu**, K. Men, K. Y. See et al. "Design and Demonstration of High Power Density Inverter for Aircraft Applications." *IEEE Transactions on Industry Applications*, vol. 53, No. 5, pp. 1168 - 1176, March-April 2017.

Conference papers

As first author:

1. **Y. Liu**, K. Y. See, R. Simanjorang, Z. Y. Lim, Z. Y. Zhao, "Modeling and Simulation of Switching Characteristics of Half-Bridge SiC Power Module in Single Leg T-type Converter for EMI Prediction." Joint IEEE International and Asia-Pacific Symposium on Electromagnetic Compatibility, May 2018, accepted for publication.

2. **Y. Liu**, K. Y. See, R. Simanjorang, and J. S. Lai,. " LCL+L filter for three-phase four-wire high power density converter." In Energy, Power and Transportation Electrification (ACEPT), Asian Conference on, pp. 1-6. IEEE, Oct 2017.

3. **Y. Liu**, K. Y. See, S. Yin, R. Simanjorang, C. F. Tong, A. Nawawi, and J. S. Lai, "Multi-domain Design of Inverter-side Inductor for LCL Filter with 50kW 60 kHz High Power Density Converter" IEEE Applied Power Electronics Conference and Exposition, pp. 2527-2533, March 2017.

4. **Y. Liu**, K. Y. See, R. Simanjorang, A. Nawawi, Z. Y. Lim, " Harmonics and Common Mode Voltage Analysis with Different Power Converter Configurations in Aircraft Grid Application" Asia-Pacific International Symposium on Electromagnetic Compatibility (APEMC), pp. 82-84, June 2017.

5. **Y. Liu**, K. Y. See, R. Simanjorang, " 3-D Modeling of Common Mode Choke for Thermal Analysis" Asia-Pacific International Symposium on Electromagnetic Compatibility (APEMC), pp. 79-81, June 2017.

6. **Y. Liu**, K. Y. See, J. S. Lai, K. J. Tseng, Y. T. Liu, C. T. Tong, A. Nawawi et al. "FEM Modelling of Three-phase Common Mode Choke for Performance Evaluation." Asia-Pacific International Symposium on Electromagnetic Compatibility (APEMC), vol. 1, pp. 96-99. Shenzhen, China, May 2016.

7. **Y. Liu**, K. Y. See, L. Ziyou, R. Simanjorang, S. Yin, C. F. Tong, et al., "Analysis and Design of Coupled Inductor and Output Harmonic Filter for Interleaved Three Phase VSCs," IEEE Region 10 Conference (TENCON), 2016, pp. 2884-2887, Nov 2016.

As co-author:

8. Y. T. Liu, K. Y. See, R. Simanjorang, **Y. Liu**, C. Gajanayake, C. F. Tong, et al., "Evaluation on Filter Topologies in High Power Density Converter Design for Power Quality and EMI Control," Asia-Pacific Symposium on Electromagnetic Compatibility (APEMC), pp. 20-23, May 2015.

9. A. Nawawi, C. F. Tong, Y. T. Liu, A. Sakanova, S. Yin, **Y. Liu**, K. Men, K. Y. See et al. "Design of High Power Density Converter for Aircraft Applications." IEEE International Conference on Electrical Systems for Aircraft, Railway, Ship Propulsion and Road Vehicles (ESARS), pp. 1-6, March 2015.

10. S. Yin, K. J. Tseng, C. F. Tong, R. Simanjorang, C. J. Gajanayake, A. Nawawi, Y. T. Liu, **Y. Liu,** K. Y. See, et al. "Gate Driver Optimization to Mitigate Shoot-through in High-speed Switching SiC Half Bridge Module." IEEE 11th International Conference on Power Electronics and Drive Systems (PEDS), pp. 484-491. June 2015.

11. A. Sakanova, S. Yin, **Y. Liu**, K. Men, J. Y. Zhao, K. Y. See, K. J. Tseng et al. "Heatsink Design for High Power Density Converter in Aircraft Applications: Parameter Sensitivity Analysis." IEEE International Conference on Electrical Systems for Aircraft, Railway, Ship Propulsion and Road Vehicles (ESARS), pp. 1-6, March2015.

12. C. F. Tong, A. Nawawi, Y. T. Liu, S. Yin, K. J. Tseng, **Y. Liu**, K. Y. See et al. "Challenges in switching waveforms measurement for a high-speed switching module." IEEE Energy Conversion Congress and Exposition (ECCE), pp. 6175-6179. September 2015.

References

[1] International Air Transport Association., "IATA Economic briefing-Airline fuel and labour cost share," IAIA, 2007.

[2] J. Rosero, J. Ortega, E. Aldabas, and L. Romeral, "Moving towards a more electric aircraft," *Aerospace and Electronic Systems Magazine, IEEE*, vol. 22, pp. 3-9, 2007.

[3] P. Wheeler and S. Bozhko, "The More Electric Aircraft: Technology and challenges," *Electrification Magazine, IEEE*, vol. 2, pp. 6-12, 2014.

[4] R. Quigley, "More electric aircraft," in *Applied Power Electronics Conference and Exposition, 1993. APEC'93. Conference Proceedings 1993., Eighth Annual*, pp. 906-911, 1993.

[5] J. S. Cloyd, "Status of the United States Air Force's more electric aircraft initiative," *IEEE Aerospace and Electronic Systems Magazine*, vol. 13, pp. 17-22, 1998.

[6] J. Chen, X. Zhang, and C. Wen, "Harmonics Attenuation and Power Factor Correction of a More Electric Aircraft Power Grid Using Active Power Filter," *IEEE Transactions on Industrial Electronics*, vol. 63, pp. 7310-7319, 2016.

[7] K. J. Karimi, "Future Aircraft Power Systems-Integration Challenges," *The Boeing Company*, 2007.

[8] A. K. Singh, P. Das, and S. Panda, "A high power density three phase AC-DC converter for more electric aircraft (MEA)," in *Power Electronics and ECCE Asia (ICPE-ECCE Asia), 2015 9th International Conference on*, pp. 1362-1367, 2015.

[9] H.-G. Jeong, K.-B. Lee, S. Choi, and W. Choi, "Performance improvement of LCL-filter-based grid-connected inverters using PQR power transformation," *Power Electronics, IEEE Transactions on*, vol. 25, pp. 1320-1330, 2010.

[10] S. Zhu and W. Ma, "Methods of Aircraft Grid Harmonic Reduction: A Review," *Scholars Journal of Engineering and Technology (SJET)*, vol. 2, pp. 270-275, 2014.

[11] R. DO160D, "Environmental Conditions and Test Procedures for Airborne Equipment," ed: INTERNATIONAL ELECTROTECHNICAL COMMISSION, 1997.

[12] A. Nawawi, C. F. Tong, Y. Liu, A. Sakanova, S. Yin, Y. Liu, *et al.*, "Design of high power density converter for aircraft applications," in *Electrical Systems for Aircraft, Railway, Ship Propulsion and Road Vehicles (ESARS), 2015 International Conference on*, pp. 1-6, 2015.

[13] Z. Chen, Y. Yao, D. Boroyevich, K. D. Ngo, P. Mattavelli, and K. Rajashekara, "A 1200-V, 60-A SiC MOSFET multichip phase-leg module for high-temperature, high-frequency applications," *IEEE Transactions on Power Electronics,* vol. 29, pp. 2307-2320, 2014.

[14] S. Yin, K. Tseng, C. Tong, R. Simanjorang, C. Gajanayake, and A. K. Gupta, "A novel gate assisted circuit to reduce switching loss and eliminate shoot-through in SiC half bridge configuration," in *2016 IEEE Applied Power Electronics Conference and Exposition (APEC)*, pp. 3058-3064, 2016.

[15] J. Mühlethaler, M. Schweizer, R. Blattmann, J. W. Kolar, and A. Ecklebe, "Optimal design of LCL harmonic filters for three-phase PFC rectifiers," *Power Electronics, IEEE Transactions on,* vol. 28, pp. 3114-3125, 2013.

[16] P. Channegowda and V. John, "Filter optimization for grid interactive voltage source inverters," *IEEE Transactions on Industrial Electronics,* vol. 57, pp. 4106-4114, 2010.

[17] Y. Jiao and F. C. Lee, "LCL Filter Design and Inductor Current Ripple Analysis for a Three-Level NPC Grid Interface Converter," *Power Electronics, IEEE Transactions on,* vol. 30, pp. 4659-4668, 2015.

[18] A. Sakanova, C. F. Tong, A. Nawawi, R. Simanjorang, K. Tseng, and A. Gupta, "Investigation on weight consideration of liquid coolant system for power electronics converter in future aircraft," *Applied Thermal Engineering,* vol. 104, pp. 603-615, 2016.

[19] X. Zhang, "Passive component weight reduction for three phase power converters." PhD diss., Virginia Polytechnic Institute and State University, 2014.

[20] B. K. Bose, "Evaluation of modern power semiconductor devices and future trends of converters," *Industry Applications, IEEE Transactions on,* vol. 28, pp. 403-413, 1992.

[21] H. Akagi and T. Shimizu, "Attenuation of conducted EMI emissions from an inverter-driven motor," *Power Electronics, IEEE Transactions on,* vol. 23, pp. 282-290, 2008.

[22] L. Asimmoaei, E. Aeloiza, J. Kim, P. Enjeti, F. Blaabjerg, L. Moran, *et al.*, "An interleaved active power filter with reduced size of passive components," in *Applied Power Electronics Conference and Exposition, 2006. APEC'06. Twenty-First Annual IEEE*, (pp. 8-pp), 2006.

[23] J. W. Kolar, U. Drofenik, J. Biela, M. L. Heldwein, H. Ertl, T. Friedli, *et al.*, "PWM converter power density barriers," in *Power Conversion Conference-Nagoya, 2007. PCC'07*, pp. P-9-P-29, 2007.

[24] J. Rodriguez, J.-S. Lai, and F. Z. Peng, "Multilevel inverters: a survey of topologies, controls, and applications," *IEEE Transactions on Industrial Electronics,* vol. 49, pp. 724-738, 2002.

[25] J.-S. Lai and F. Z. Peng, "Multilevel converters-a new breed of power converters," *IEEE Transactions on Industry Applications*, vol. 32, pp. 509-517, 1996.

[26] A. Sakanova, S. Yin, Y. Liu, K. Men, J. Zhao, K. See, *et al.*, "Heatsink design for high power density converter in aircraft applications: parameter sensitivity analysis," in *Electrical Systems for Aircraft, Railway, Ship Propulsion and Road Vehicles (ESARS), 2015 International Conference on*, pp. 1-6, 2015.

[27] R. Wrobel, N. McNeill, and P. H. Mellor, "Performance analysis and thermal modeling of a high-energy-density prebiased inductor," *IEEE Transactions on Industrial Electronics*, vol. 57, pp. 201-208, 2010.

[28] R. Wrobel and P. H. Mellor, "Thermal design of high-energy-density wound components," *IEEE Transactions on Industrial Electronics*, vol. 58, pp. 4096-4104, 2011.

[29] L. Jiang, Q. Chen, and X. Ren, "Analysis of a novel coupled inductor for LCL filter in grid-connected inverter," in *Power Electronics Conference (SPEC), IEEE Annual Southern*, pp. 1-6, 2016.

[30] Y. Liu, K. Y. See, K. J. Tseng, R. Simanjorang, and J. S. Lai, "Magnetic Integration of Three-Phase LCL Filter With Delta-Yoke Composite Core," *IEEE Transactions on Power Electronics*, vol. 32, pp. 3835-3843, 2017.

[31] D. Pan, X. Ruan, C. Bao, W. Li, and X. Wang, "Magnetic integration of the LCL filter in grid-connected inverters," *IEEE Transactions on Power Electronics*, vol. 29, pp. 1573-1578, 2014.

[32] P. Zumel, O. Garcia, J. Cobos, and J. Uceda, "Magnetic integration for interleaved converters," in *Applied Power Electronics Conference and Exposition, 2003. APEC'03. Eighteenth Annual IEEE*, 2003, pp. 1143-1149.

[33] J. Fang, H. Li, and Y. Tang, "A Magnetic Integrated LLCL Filter for Grid-Connected Voltage-Source Converters," *IEEE Transactions on Power Electronics*, vol. 32, pp. 1725-1730, 2017.

[34] A. Ferreira, A. Carvalho, A. Martins, F. Pereira, and V. Sobrado, "Comparison of PWM methods for current harmonic reduction in a non-ideal grid," in *Industrial Electronics Society, IECON 2013-39th Annual Conference of the IEEE*, pp. 538-543, 2013.

[35] P. Sugirtha and S. Rajanbabu, "Reduction of harmonics based on online-SHE compensation technique for PWM inverter," in *Computation of Power, Energy Information and Commuincation (ICCPEIC), 2016 International Conference on*, pp. 572-580, 2016.

[36] Y. Liu, K. Y. See, S. Yin, R. Simanjorang, C. F. Tong, A. Nawawi, *et al.*, "LCL Filter Design of 50 kW 60 kHz SiC Inverter with Size and Thermal

Considerations for Aerospace Applications," *IEEE Transactions on Industrial Electronics*, vol. 64, No. 10, pp. 8321 – 8333, 2017.

[37] O. Vodyakho and C. C. Mi, "Three-level inverter-based shunt active power filter in three-phase three-wire and four-wire systems," *IEEE Transactions on Power Electronics*, vol. 24, pp. 1350-1363, 2009.

[38] C.-S. Lam and M.-C. Wong, *Design and control of hybrid active power filters*: Springer, 2014.

[39] J. Xue, "High Density EMI Filter Design in High Power Three-Phase Motor Drive Systems," PhD diss., The Tennessee of University, Knoxville, 2014.

[40] J. Huang and H. Shi, "Reducing the common-mode voltage through carrier peak position modulation in an SPWM three-phase inverter," *IEEE Transactions on Power Electronics*, vol. 29, pp. 4490-4495, 2014.

[41] K. Euerle, K. Iyer, E. Severson, R. Baranwal, S. Tewari, and N. Mohan, "A compact active filter to eliminate common-mode voltage in a SiC-based motor drive," in *Energy Conversion Congress and Exposition (ECCE), 2016 IEEE*, pp. 1-8.

[42] C. T. Morris, D. Han, and B. Sarlioglu, "Reduction of Common Mode Voltage and Conducted EMI Through Three-Phase Inverter Topology," *IEEE Transactions on Power Electronics*, vol. 32, pp. 1720-1724, 2017.

[43] M. S. Rylko, B. J. Lyons, J. G. Hayes, and M. G. Egan, "Revised magnetics performance factors and experimental comparison of high-flux materials for high-current DC–DC inductors," *IEEE Transactions on Power Electronics*, vol. 26, pp. 2112-2126, 2011.

[44] R. Lee and D. S. Stephens, "Influence of core gap in design of current-limiting transformers," *Magnetics, IEEE Transactions on*, vol. 9, pp. 408-410, 1973.

[45] M. K. Kazimierczuk, *High-frequency magnetic components*: John Wiley & Sons, 2009.

[46] W. Wu, Y. He, and F. Blaabjerg, "An LLCL power filter for single-phase grid-tied inverter," *Power Electronics, IEEE Transactions on*, vol. 27, pp. 782-789, 2012.

[47] F. Li, X. Zhang, H. Zhu, H. Li, and C. Yu, "An LCL-LC filter for grid-connected converter: topology, parameter, and analysis," *IEEE Transactions on Power Electronics*, vol. 30, pp. 5067-5077, 2015.

[48] W. Wu, Y. Sun, Z. Lin, T. Tang, F. Blaabjerg, and H. S.-H. Chung, "A new $ LCL $-filter with in-series parallel resonant circuit for single-phase grid-tied inverter," *IEEE Transactions on Industrial Electronics*, vol. 61, pp. 4640-4644, 2014.

[49] J. Xu, J. Yang, J. Ye, Z. Zhang, and A. Shen, "An LTCL Filter for Three-Phase Grid-Connected Converters," *Power Electronics, IEEE Transactions on*, vol. 29, pp. 4322-4338, 2014.

[50] A. M. Cantarellas, E. Rakhshani, D. Remon, and P. Rodriguez, "Design of passive trap-LCL filters for two-level grid connected converters," in *Power Electronics and Applications (EPE), 2013 15th European Conference on*, pp. 1-9, 2013.

[51] V. Dzhankhotov and J. Pyrhönen, "Passive $ LC $ Filter Design Considerations for Motor Applications," *IEEE Transactions on Industrial Electronics,* vol. 60, pp. 4253-4259, 2013.

[52] X. Wang, F. Blaabjerg, and P. C. Loh, "Virtual RC damping of LCL-filtered voltage source converters with extended selective harmonic compensation," *IEEE Transactions on Power Electronics,* vol. 30, pp. 4726-4737, 2015.

[53] S. M. Sharkh, M. A. Abu-Sara, G. I. Orfanoudakis, and B. Hussain, *Power electronic converters for microgrids*: John Wiley & Sons, 2014.

[54] K. Koiwa, M. Rosyadi, A. Umemura, R. Takahashi, and J. Tamura, "Sensorless virtual resistance damping method for grid-connected three-phase PWM converter with LCL filter," in *Electrical Machines and Systems (ICEMS), 2013 International Conference on*, pp. 1746-1749, 2013.

[55] Y. Lei, Z. Zhao, F. He, S. Lu, and L. Yin, "An improved virtual resistance damping method for grid-connected inverters with LCL filters," in *Energy Conversion Congress and Exposition (ECCE), 2011 IEEE*, pp. 3816-3822, 2011.

[56] R. N. Beres, X. Wang, F. Blaabjerg, M. Liserre, and C. L. Bak, "Optimal design of high-order passive-damped filters for grid-connected applications," *IEEE Transactions on Power Electronics,* vol. 31, pp. 2083-2098, 2016.

[57] A. Boglietti, A. Cavagnino, and D. A. Staton, "TEFC induction motors thermal models: A parameter sensitivity analysis," *IEEE Transactions on Industry Applications,* vol. 41, pp. 756-763, 2005.

[58] D. A. Staton and A. Cavagnino, "Convection heat transfer and flow calculations suitable for electric machines thermal models," *IEEE Transactions on Industrial Electronics,* vol. 55, pp. 3509-3516, 2008.

[59] F. Marignetti, V. D. Colli, and Y. Coia, "Design of axial flux PM synchronous machines through 3-D coupled electromagnetic thermal and fluid-dynamical finite-element analysis," *IEEE Transactions on Industrial Electronics,* vol. 55, pp. 3591-3601, 2008.

[60] P. Mellor, D. Roberts, and D. Turner, "Lumped parameter thermal model for electrical machines of TEFC design," in *IEE Proceedings B-Electric Power Applications*, pp. 205-218, 1991.

[61] A. Boglietti, A. Cavagnino, D. Staton, M. Shanel, M. Mueller, and C. Mejuto, "Evolution and modern approaches for thermal analysis of electrical machines," *IEEE Transactions on Industrial Electronics,* vol. 56, pp. 871-882, 2009.

[62] C. Zhang, T. Dragicevic, J. C. Vasquez, and J. M. Guerrero, "Resonance damping techniques for grid-connected voltage source converters with LCL filters—A review," in *Energy Conference (ENERGYCON), 2014 IEEE International*, pp. 169-176, 2014.

[63] W. Wu, Y. He, T. Tang, and F. Blaabjerg, "A new design method for the passive damped LCL and LLCL filter-based single-phase grid-tied inverter," *IEEE Transactions on Industrial Electronics,* vol. 60, pp. 4339-4350, 2013.

[64] M. Malinowski, M. P. Kazmierkowski, W. Szczygiel, and S. Bernet, "Simple sensorless active damping solution for three-phase PWM rectifier with LCL filter," in *31st Annual Conference of IEEE Industrial Electronics Society, 2005. IECON 2005.*, (pp. 5-pp), 2005.

[65] M. Liserre, F. Blaabjerg, and S. Hansen, "Design and control of an LCL-filter-based three-phase active rectifier," *Industry Applications, IEEE Transactions on,* vol. 41, pp. 1281-1291, 2005.

[66] J. R. Massing, M. Stefanello, H. A. Grundling, and H. Pinheiro, "Adaptive current control for grid-connected converters with LCL filter," *IEEE Transactions on Industrial Electronics,* vol. 59, pp. 4681-4693, 2012.

[67] Y. Tang, P. C. Loh, P. Wang, F. H. Choo, F. Gao, and F. Blaabjerg, "Generalized design of high performance shunt active power filter with output LCL filter," *IEEE Transactions on Industrial Electronics,* vol. 59, pp. 1443-1452, 2012.

[68] G. Shen, X. Zhu, J. Zhang, and D. Xu, "A new feedback method for PR current control of LCL-filter-based grid-connected inverter," *IEEE Transactions on Industrial Electronics,* vol. 57, pp. 2033-2041, 2010.

[69] F. Liu, Y. Zhou, S. Duan, J. Yin, B. Liu, and F. Liu, "Parameter design of a two-current-loop controller used in a grid-connected inverter system with LCL filter," *IEEE Transactions on Industrial Electronics,* vol. 56, pp. 4483-4491, 2009.

[70] L. Wei and R. A. Lukaszewski, "Optimization of the main inductor in a LCL filter for three phase active rectifier," in *Industry Applications Conference, 2007. 42nd IAS Annual Meeting. Conference Record of the 2007 IEEE*, pp. 1816-1822, 2007.

[71] K.-B. Park, F. Kieferndorf, U. Drofenik, S. Pettersson, and F. Canales, "Weight minimization of LCL filters for high power converters," in *Power Electronics and ECCE Asia (ICPE-ECCE Asia), 2015 9th International Conference on*, pp. 142-149, 2015.

[72] X. She, X. Yu, F. Wang, and A. Q. Huang, "Design and demonstration of a 3.6-kV–120-V/10-kVA solid-state transformer for smart grid application," *IEEE Transactions on Power Electronics*, vol. 29, pp. 3982-3996, 2014.

[73] E. Laloya, O. Lucia, H. Sarnago, and J. Burdio, "Thermal Management in Power Converters: From State-of-the-Art to Future Ultra High Efficiency Systems." *IEEE Transactions on Power Electronics*, vol. 31, pp. 7896-7908, 2016.

[74] A. Fluent, "Ansys Fluent Theory Guide," *ANSYS Inc., USA*, 2011.

[75] D. G. Holmes and T. A. Lipo, *Pulse width modulation for power converters: principles and practice* vol. 18: John Wiley & Sons, 2003.

[76] A. Reznik, M. G. Simoes, A. Al-Durra, and S. Muyeen, "Filter Design and Performance Analysis for Grid-Interconnected Systems," *Industry Applications, IEEE Transactions on*, vol. 50, pp. 1225-1232, 2014.

[77] S. Maniktala, *Switching Power Supplies A-Z*: Elsevier, 2012.

[78] V. A. KUMAR and T. KUMAR, "LCL Filter Design and Performance Analysis for Grid-Interconnected Systems," *Int. J. Adv. Technol. Innovative Res.* 7, no. 9, 1549-1554, 2015.

[79] N. Kurita, K. Onda, K. Nakanoue, and K. Inagaki, "Loss Estimation Method for Three-Phase AC Reactors of Two Types of Structures Using Amorphous Wound Cores in 400-kVA UPS," *Power Electronics, IEEE Transactions on*, vol. 29, pp. 3657-3668, 2014.

[80] H. Fukunaga, T. Eguchi, Y. Ohta, and H. Kakehashi, "Core loss in amorphous cut cores with air gaps," *Magnetics, IEEE Transactions on*, vol. 25, pp. 2694-2698, 1989.

[81] W. Chen, X. Yang, and Z. Wang, "A novel hybrid common-mode EMI filter with active impedance multiplication," *IEEE Transactions on Industrial Electronics*, vol. 58, pp. 1826-1834, 2011.

[82] H. Akagi and S. Tamura, "A passive EMI filter for eliminating both bearing current and ground leakage current from an inverter-driven motor," *IEEE Transactions on Power Electronics*, vol. 21, pp. 1459-1469, 2006.

[83] J. Rekola, J. Jokipii, and T. Suntio, "Losses of converters with iron and amorphous core AC-filter inductors in LVDC distribution," in *Industrial Electronics Society, IECON 2014-40th Annual Conference of the IEEE*, pp. 1587-1593, 2014.

[84] J. Xue, "Single-phase vs. Three-phase High Power High Frequency Transformers," Master diss., Virginia Polytechnic Institute and State University, 2010.

[85] C. W. T. McLyman, *Transformer and inductor design handbook*: CRC press, 2011.

[86] H. Rossmanith, M. Doebroenti, M. Albach, and D. Exner, "Measurement and characterization of high frequency losses in nonideal litz wires," *IEEE Transactions on Power Electronics,* vol. 26, pp. 3386-3394, 2011.

[87] F. Liu, X. Zha, Y. Zhou, and S. Duan, "Design and research on parameter of LCL filter in three-phase grid-connected inverter," in *Power Electronics and Motion Control Conference, 2009. IPEMC'09. IEEE 6th International*, pp. 2174-2177, 2009.

[88] M. Huang, F. Blaabjerg, Y. Yang, and W. Wu, "Step by step design of a high order power filter for three-phase three-wire grid-connected inverter in renewable energy system," in *Power Electronics for Distributed Generation Systems (PEDG), 2013 4th IEEE International Symposium on*, pp. 1-8, 2013.

[89] F. Li, X. Zhang, H. Zhu, H. Li, and C. Yu, "An LCL-LC Filter for Grid-Connected Converter: Topology, Parameter, and Analysis," *IEEE Transactions on Power Electronics,* vol. 30, pp. 5067-5077, 2015.

[90] C. Wei, H. Jiannong, and H. Tianding, "Design considerations of inductor for 500 kVA PV inverter based on Euro efficiency," in *Power Electronics for Distributed Generation Systems (PEDG), 2014 IEEE 5th International Symposium on*, pp. 1-4, 2014.

[91] T. S. J. S. S. OUTTEN, T. H. M. CARLEN, and A. ABB, "BENEFITS OF TRANSFORMERS BASED ON TRIANGULAR WOUND CORE CONFIGURATIONS."CIGRE, 2012.

[92] C. Deng, D. Xu, P. Chen, C. Hu, W. Zhang, Z. Wen, *et al.*, "Integration of both EMI filter and boost inductor for 1-kW PFC converter," *IEEE Transactions on Power Electronics,* vol. 29, pp. 5823-5834, 2014.

[93] K. Umetani, T. Tera, and K. Shirakawa, "Novel magnetic structure of integrated differential-mode and common-mode inductors to suppress DC saturation," in *Power Electronics Conference (IPEC-Hiroshima 2014-ECCE-ASIA), 2014 International*, pp. 304-311, 2014.

[94] C. Deng, X. Shi, and Y. Zhong, "An integrated unit of LCL filter for grid-connected inverter," in *Energy Conversion Congress and Exposition (ECCE), 2015 IEEE*, pp. 5287-5292, 2015.

[95] Y. Zhenyang, W. Shishan, S. Zheng, and B.-L. Lee, "The reviews of integrated EMI filters applied in power electronic system," in *Electromagnetic Compatibility (APEMC), 2015 Asia-Pacific Symposium on*, pp. 227-230, 2015.

[96] G. Gohil, L. Bede, R. Teodorescu, T. Kerekes, and F. Blaabjerg, "An Integrated Inductor For Parallel Interleaved Three-Phase Voltage Source Converters," *IEEE Transactions on Power Electronics,* vol. 31, pp. 3400-3414, 2016.

[97] Y. Liu, K. See, R. Simanjorang, L. Yong, C. Gajanayake, C. Tong, *et al.*, "Evaluation on Filter Topologies in High Power Density Converter Design for Power Quality and EMI Control," in *Electromagnetic Compatibility (APEMC), 2015 Asia-Pacific Symposium on*, pp. 20-23, 2015.

[98] M. ANSYS, "3D Software, 2010, version 13.0. 0," *ANSYS Inc.*, USA, 2010.

[99] X. Zhang, D. Boroyevich, and R. Burgos, "Design and integration of interphase inductors for interleaved three phase voltage-source-inverters in DC-fed motor drive systems," in *Power Electronics Conference (IPEC-Hiroshima 2014-ECCE-ASIA), 2014 International*, pp. 2626-2631, 2014.

[100] D. Zhang, F. Wang, R. Burgos, R. Lai, and D. Boroyevich, "Impact of interleaving on AC passive components of paralleled three-phase voltage-source converters," *IEEE Transactions on Industry Applications,* vol. 46, pp. 1042-1054, 2010.

[101] J. Ewanchuk and J. Salmon, "Three-limb coupled inductor operation for paralleled multi-level three-phase voltage sourced inverters," *IEEE Transactions on Industrial Electronics,* vol. 60, pp. 1979-1988, 2013.

[102] A. A. Khan, H. Cha, and H.-G. Kim, "Three-Phase Three-Limb Coupled Inductor for Three-Phase Direct PWM AC–AC Converters Solving Commutation Problem," *IEEE Transactions on Industrial Electronics*, vol. 63, pp. 189-201, 2016.

[103] D. Shin, J.-P. Lee, D.-W. Yoo, and H.-J. Kim, "Stability Improvement of Interleaved Voltage Source Inverters Employing Coupled Inductors for Grid-Connected Applications," *IEEE Transactions on Industrial Electronics,* vol. 62, pp. 6014-6023, 2015.

[104] Y. Liu, K. Y. See, J.-S. Lai, K. Tseng, Y. Liu, C. F. Tong, *et al.*, "FEM modelling of three-phase common mode choke for performance evaluation," in *2016 Asia-Pacific International Symposium on Electromagnetic Compatibility (APEMC)*, pp. 96-99, 2016,.

[105] A. M. Hava and E. Ün, "A high-performance PWM algorithm for common-mode voltage reduction in three-phase voltage source inverters," *IEEE Transactions on Power Electronics,* vol. 26, pp. 1998-2008, 2011.

[106] N. Zhu, J. Kang, D. D. Xu, B. Wu, and Y. Xiao, "An integrated AC choke design for common-mode current suppression in neutral-connected

power converter systems," *IEEE Transactions on Power Electronics,* vol. 27, pp. 1228-1236, 2012.

[107] A. Khodakarami, S. M. Pedramrazi, and H. F. Farahani, "Analysis of auxiliary winding effect on the leakage inductance reduction in the pulse transformer using ANSYS," *Journal of Electromagnetic Analysis and Applications,* vol. 2, p. 513, 2010.

[108] H. Chen, Z. Qian, S. Yang, and C. Wolf, "Finite-element modeling of saturation effect excited by differential-mode current in a common-mode choke," *IEEE Transactions on Power Electronics,* vol. 24, pp. 873-877, 2009.

[109] M. Kovacic, S. Stipetic, Z. Hanic, and D. Zarko, "Small-Signal Calculation of Common-Mode Choke Characteristics Using Finite-Element Method," *IEEE Transactions on Electromagnetic Compatibility,* vol. 57, pp. 93-101, 2015.

[110] J. Petzold, "Advantages of softmagnetic nanocrystalline materials for modern electronic applications," *Journal of Magnetism and Magnetic Materials,* vol. 242, pp. 84-89, 2002.

[111] S. Yin, K. Tseng, Y. Liu, R. Simanjorang, C. Tong, and A. K. Gupta, "Demonstration of a 50 kW and 100 kHz SiC high power density converter for aerospace application," in *Region 10 Conference (TENCON), 2016 IEEE,* pp. 2888-2891, 2016.

[112] J. Biela and J. W. Kolar, "Cooling concepts for high power density magnetic devices," in *Power Conversion Conference-Nagoya, 2007. PCC'07*, pp. 1-8, 2007.

[113] N. Simpson, R. Wrobel, and P. Mellor, "Multi-physics design of high-energy-density wound components," in *2015 IEEE Energy Conversion Congress and Exposition (ECCE)*, pp. 3857-3864, 2015.

[114] C. W. T. McLyman, *Transformer and inductor design handbook*: CRC press, 2016.

[115] H. Gavrila and V. Ionita, "Crystalline and amorphous soft magnetic materials and their applications- status of art and challenges," *Journal of Optoelectronics and Advanced Materials(Romania),* vol. 4, pp. 173-192, 2002.